Title
Contributions of clouds to Greenland's surface melt

Author
Wang, Wenshan

Publication Date
2017

Peer reviewed|Thesis/dissertation

UNIVERSITY OF CALIFORNIA,
IRVINE

Contributions of clouds to Greenland's surface melt

DISSERTATION

submitted in partial satisfaction of the requirements
for the degree of

DOCTOR OF PHILOSOPHY

in Earth System Science

by

Wenshan Wang

Dissertation Committee:
Professor Charles S. Zender, Chair
Professor Eric Rignot
Professor Steven J. Davis

2017

DEDICATION

To every researcher who works hard to collect data in the polar regions.

TABLE OF CONTENTS

LIST OF FIGURES

LIST OF TABLES

ACKNOWLEDGMENTS

Graduate school is a journal. You start as a curious kid and graduate becoming an independent scientist. I couldn't have made this far without the help and support from my advisor, my colleagues and collaborators, and my friends and family.

My superb advisor, Dr. Charles S. Zender, led me to see the ocean of science. He encouraged me to go far and go deep, and always brought me back when I drifted too far. He taught me how to think with imagination, how to write with clarity, how to give suggestions with politeness, and how to face problems with humor. He guided me to acquire diverse tools from data analysis to model simulations and to fieldwork, and supported me to achieve my dream of going to Greenland! This graduate-school journal has been so intriguing and rewarding because of him!

My committee members, Dr. Eric Rignot and Dr. Steven J. Davis, gave me comprehensive suggestions along the way and provided me with collaboration opportunities to broaden my horizon. Their own dedication to science also inspires me to pursue excellence! Dr. Dirk van As always asked the hard questions, which were critical to improve the quality of our projects. He, Dr. Signe Bech Andersen, and Jessica Jenkins shared with me invaluable fieldwork experience in the harsh and variable polar regions. Dr. Scott Stephenson is a powerful drive of the Arctic shipping project. From him, I learned that nothing can baffle persistent scientists! Dr. Andreas Peter Ahlstrøm, Dr. Nathaniel B. Miller, Dr. Hailong Wang, Johannes Mohrmann, and Dr. Robert Wood patiently answered a lot of my questions about measurements and processes of cloud and radiation. Helen He, Carolyn McClaskey, Tyson Patros, and John Hunter went above and beyond to help me solve technical and writing problems. Meetings with my group members, Morgan Gorris, Dr. Sagar Parajuli, Zachary Wolff, Dr. Cheng Dang, Matthew Laffin, Ajay Saini, and Justin Tang inspired countless new ideas. Encouragement from my cohort, Cilan Cai, Enrico Ciraci, Erin Delman, Clay Elder, A. J. Purdy, and Hongju Yu kept me moving forward. The broad topics and delightful environment conducted by all faculty, staff, and students in our ESS department provided strong supports for both research and mindfulness.

The journal would be lonely without accompany of Kevin and all my friends. The laughs we had together made home feel closer. Finally, I would like to thank my parents for their infinite love and support!

This work was funded by NASA Grant NNX12AF48A, NASA ACCESS NNX14AH55A, and DOE ACME DE-SC0012998.

CURRICULUM VITAE

Wenshan Wang

EDUCATION

Ph.D. Candidate in Earth System Science **2012-2017**
University of California, Irvine *Irvine, CA, U.S.A.*

- Dissertation: Contributions of clouds to Greenland's surface melt
- Advisor: Dr. Charles S. Zender

M.S. in Physical Geography **2009-2012**
Beijing Normal University *Beijing, China*

- Thesis: Weekly cycle of PM10 and meteorological signals over Eastern China
- Advisor: Dr. Daoyi Gong

B.S. in Natural Resource Science and Technology **2005-2009**
Beijing Normal University *Beijing, China*

PUBLICATIONS

1. **Wenshanw Wang**, Charles S. Zender, Dirk van As, Paul C. J. P. Smeets, and Michiel R. van den Broeke (2016), A Retrospective, Iterative, Geometry-Based (RIGB) tilt correction method for radiation observed by automatic weather stations on snow-covered surfaces: application to Greenland, *The Cryosphere*, 10, 727-741, doi:10.5194/tc-10-727-2016.

2. Rui Mao, Dao-Yi Gong, Tianbao Zhao, **Wenshanw Wang**, and Jing Yang (2015), Trends in the frequency of high relative humidity over China: 1979 to 2012, *Journal of Climate*, 28:24, 9816-9837, doi:10.1175/JCLI-D-14-00840.1.

3. Daoyi Gong, **Wenshan Wang**, Yun Qian, Wenbing Bai, Yuanxi Guo, and Rui Mao (2014), Observed holiday aerosol reduction and temperature cooling over East Asia, *Journal of Geophysical Research: Atmospheres*, 119, 6306-6324, doi:10.1002/2014JD021464.

4. **Wenshanw Wang**, Daoyi Gong, Zhiyang Zhou, and Yuanxi Guo (2012), Robustness of the aerosol weekly cycle over Southeastern China, *Atmospheric Environment*, 61, 409-418, doi:10.1016/j.atmosenv. 2012.07.029.

5. Jing Yang, Daoyi Gong, **Wenshan Wang**, Miao Hu, and Rui Mao (2012), Extreme drought event of 2009/2010 over southwestern China, *Meteorology and Atmospheric Physics*, 115:173-184, doi: 10.1007/s00703-011-0172-6.

SELECTED PRESENTATIONS

1. **Wenshanw Wang**, Charles S. Zender, Dirk van As, Paul C. J. P. Smeets, and Michiel R. van den Broeke (2016), Cloud-induced stabilization of Greenland surface melt, *AGU Fall Meeting 2016*, San Francisco, U.S.A. (Oral)

2. **Wenshanw Wang**, Charles S. Zender, Dirk van As, Paul C. J. P. Smeets, and Michiel R. van den Broeke (2015), Correcting radiation measured by tilted automatic weather stations: application to Greenland, *AGU Fall Meeting 2015*, San Francisco, U.S.A. (Poster)

3. **Wenshan Wang** and Charles S. Zender (2015), Improving estimates of cloud radiative forcing over Greenland, *Improving our fundamental understanding of the role of aerosol-cloud interactions in the climate system, Sackler Colloquia by National Academy of Sciences*, Irvine, CA, U.S.A. (Poster)

4. **Wenshan Wang** and Daoyi Gong (2011), Weekly cycle of PM10 in Eastern China: the seasonal patterns and possible effect on radiation, *European Geosciences Union General Assembly 2011*, Vienna, Austria (Poster)

FIELDWORK EXPERIENCE

1. Calibrate unattended radiometers on ice sheet, Thule, Greenland, 07/2016 (collaborate with the PROMICE team from GEUS, Denmark)

2. NASA Snow Measurement School 2016, How to explore a snow pit, 01/2016, NASA International Snow Working Group Remote Sensing, Fraser, CO, U.S.A

TEACHING EXPERIENCE

1. Departmental seminar:
    - The beauty of Linux (11/2015)
    - How can NCO help you (10/2015)

2. Teaching assistant:
    - ESS 19: Modeling the Earth (five times, 09/2013-06/2016)
    - ESS 1: Introduction to ESS (09/2016)

3. CLEAN member: outreach in Macarthur Elementary School

4. Mentor of the Women and Minorities in STEM Mentorship Program

ABSTRACT OF THE DISSERTATION

Contributions of clouds to Greenland's surface melt

By

Wenshan Wang

Doctor of Philosophy in Earth System Science

University of California, Irvine, 2017

Professor Charles S. Zender, Chair

Clouds have a strong impact on surface radiation fluxes and may have triggered multiple massive melt events in the Arctic. However, harsh and distinctive physical conditions there make it difficult to obtain the regular and reliable in situ observations of clouds and radiation necessary to study the cloud radiative effects (CRE). In this dissertation, we use radiation observed by 30+ automatic weather stations (AWS) all over Greenland, facilitated by a radiative transfer model, to establish the ground-truth of CRE temporal variability and spatial distribution in melt season (May to August). We then use our novel dataset of CRE estimated from in situ measurements to evaluate the CRE estimated by five well-known large-scale datasets from satellite retrievals, reanalyses, and climate models.

AWS provide valuable observations of radiation and basic meteorology. However, their results may contain considerable biases caused primarily by station tilt. We invent a method that relies only on solar geometry (no additional instrumentation) to retrospectively correct tilt-induced errors in insolation, which affect more than 60% of data and can reach up to $200\,\mathrm{W\ m^{-2}}$. The overall improvement is $11\,\mathrm{W\ m^{-2}}$ on average, equivalent to $0.24\,\mathrm{m}$ of snow melt in liquid during melt season. Albedo estimated using the adjusted insolation presents a consistent semi-smiling diurnal cycle, and agrees better with temperature changes on monthly and inter-annual time scales. Overheating and riming on sensor domes due

to a lack of proper shading and ventilation can also contribute to tens W m^{-2} of biases in longwave measurements. We apply data quality control using physical limits and inter-variable principles to reduce their influences.

We then estimate CRE by subtracting simulated clear-sky radiation from corrected AWS all-sky observations, and examine the relative importance of major factors (such as cloud properties, surface albedo, and solar zenith angle) that determine the temporal and spatial distributions of CRE. Clouds currently warm Greenland during most of the melt season. However, the seasonal trends are contrasting in the ablation (elevation $<$ 1800 m) and accumulation (elevation $\geq$ 1800 m) zones. Net CRE in the ablation zone, controlled mainly by shortwave CRE, decreases from May to July and increases afterwards. Net warming in the accumulation zone, controlled mainly by longwave CRE, increases from May to August. Average through melt season, clouds warm most of Greenland except in the lower southern ablation zone. CRE generally decreases with elevation, forming a "warm center" spatial distribution. In the ablation zone, the large variability of albedo dominates the seasonal trend and spatial distribution of CRE, shown by strong correlations for both (r > 0.90 and p << 0.01). In the accumulation zone where albedo is constantly high, CRE seasonal trend and spatial distribution are more likely associated with cloud properties, such as cloud fraction and liquid water path. On an hourly timescale, CRE exhibits a bimodal distribution with one peak near 0 W m^{-2} (i.e., clear state) and the other near 40 W m^{-2} (i.e., cloudy state), indicating that Greenland is either nearly clear or heavily cloudy with fast transitions between the two. At the cloudy state, CRE strongly correlates with the combination of solar zenith angle and albedo (r=0.85, p<0.01) probably because clouds are already thick enough for CRE to become saturated. The actual links among CRE, cloud properties, and environmental conditions need to be further examined using large-scale observations and determined by model simulations.

Therefore, we evaluate five well-known gridded datasets by assessing their CRE spatial distributions against AWS estimates and examining their cloud-radiation physics as well as simulations of the major determinants of CRE. CRE areal averages from the five datasets are similar (all around $10\,\mathrm{W\ m^{-2}}$). MERRA-2, ERA-Interim, and CERES CRE estimates agree with in-situ estimates and reproduce the "warm center" distribution. However, the NCAR Arctic System Reanalysis (ASR) and the CESM Large ENSemble community project (LENS) show strong warming in the south and northwest, forming a "warm L-shape" CRE distribution. Discrepancies are mainly caused by longwave CRE in the accumulation zone. MERRA-2, ERA-Interim, and CERES successfully reproduce cloud fraction and its dominant positive influence on longwave CRE in this region. On the other hand, longwave CRE from ASR and LENS correlates strongly with ice water path instead of with cloud fraction or liquid water path. In the ablation zone, MERRA-2 best captures the observed inter-station changes, due to its correct radiation physics and good simulations of surface albedo.

This dissertation provides the first CRE estimate over the entirety of Greenland using multi-year high-quality in-situ observations. It identifies the unique features of CRE temporal and spatial distributions, and uses them to evaluate the verisimilitude of large-scale observations and simulations. Our new methods and findings improve understanding of and ability to predict cloud-related contributions to the increasing widespread melting events in Greenland and, by extension, other polar regions.

Chapter 1

Introduction

1.1 Clouds and Arctic warming

Instrumental records and model simulations show a quickly warming Arctic (*Serreze and Barry*, 2011). Surface air temperature has increased 1.36°C per century since 1875, almost double the Northern Hemisphere average rate (*Bekryaev et al.*, 2010; *Serreze and Barry*, 2011). Moreover, this Arctic warming has accelerated by a factor of about 10 (to 1.35°C per decade) since 2000 (*Bekryaev et al.*, 2010; *Serreze and Barry*, 2011). Climate models from the fourth assessment report of the Intergovernmental Panel on Climate Change (IPCC) also show a warmer-than-global-average Arctic as carbon dioxide doubles (*Winton*, 2006; *Serreze and Barry*, 2011). Shrinking of both sea ice and ice sheets has accelerated (e.g., *Comiso* (2002); *Chen et al.* (2006); *Serreze et al.* (2007); *Rignot et al.* (2011); *Velicogna and Wahr* (2013); *Hofer et al.* (2017)), as melt extent expands (*Tedesco et al.*, 2013), melt season elongates (*Mioduszewski et al.*, 2016), and gaps between massive melt events shorten (*Mote*, 2007; *Tedesco et al.*, 2011). The potential climate impacts of continued warming are profound. For example, completely melting Greenland, the largest ice sheet in the Arctic, would cause about 7 m sea-level rise (*Church et al.*, 2001). Fresh water from Arctic melt could weaken the heat transport between high-latitudes and low-latitudes by perturbing the buoyancy in the North Atlantic (*Swingedouw and Braconnot*, 2007). Furthermore, the increasing heat loss from open ocean to atmosphere and surface darkening accelerate Arctic warming (*Serreze and Barry*, 2011) due to positive feedbacks.

Clouds are a major mediator of Arctic warming because they strongly modulate surface radiative energy budgets due to the region's persistent cloudiness and dry atmosphere (*Intrieri et al.*, 2002; *Wang and Key*, 2003; *Shupe and Intrieri*, 2004; *Morrison et al.*, 2011; *Cesana et al.*, 2012; *Zygmuntowska et al.*, 2012; *Shupe et al.*, 2013b). Cloud fraction in the entire Arctic is large throughout all seasons, with an annual mean of ∼70% (*Wang and Key*, 2005). Even at Summit, Greenland, where the altitude exceeds 3000 m a.s.l. and is among the least cloudy parts of Greenland, cloud fraction is above 80% during most time of a year (*Shupe et al.*, 2013b). Moreover, this high cloud fraction largely consists of the radiatively important low-level liquid-containing clouds (*Shupe and Intrieri*, 2004; *Cesana et al.*, 2012; *Shupe et al.*, 2013b). The extremely dry atmosphere with limited water content in the Arctic enhances the clouds' influence by enlarging the contrast of greenhouse effects between cloudy and clear skies (*Curry et al.*, 1996; *Zygmuntowska et al.*, 2012; *Cox et al.*, 2015). Recent massive melt events in the Arctic are all associated with cloud variability (*Kay et al.*, 2008; *Vavrus et al.*, 2010; *Bennartz et al.*, 2013; *Hofer et al.*, 2017). Clouds can cool the surface through the shortwave shading effect, and an absence of clouds accelerates surface melt (*Kay et al.*, 2008; *Vavrus et al.*, 2010; *Hofer et al.*, 2017). In 2007, reduced cloudiness due to anticyclones in the Western Arctic Ocean contributed 32 W m^{-2} (equivalent to 2.4 K warmer in surface ocean) to the then-unprecedented Arctic sea ice loss (*Kay et al.*, 2008). On the other hand, clouds can enhance surface heating caused by warm southerly advection, and trigger massive surface melt through their longwave greenhouse effect (*Bennartz et al.*, 2013). In 2012, almost the entirety of Greenland experienced surface melt, the largest melt extent in the satellite era (*Nghiem et al.*, 2012). Strong and persistent warm anticyclonic wind anomalies (*Hanna* *et al.*, 2014) and the induced snow-albedo feedback both contributed significantly (*Tedesco et al.*, 2013). However, only simulations with the presence of thin liquid-containing clouds have successfully reproduced the great magnitude of this melt (*Bennartz et al.*, 2013).

The competition of clouds' longwave greenhouse effect and shortwave shading effect is determined by a complicated and dynamic function of both cloud properties (e.g., cloud fraction, cloud water path, and cloud droplet shape and size) and environmental conditions (e.g., surface albedo, solar zenith angle, aerosols, and atmospheric profiles) (*Curry et al.*, 1996; *Shupe and Intrieri*, 2004; *Serreze and Barry*, 2011; *Cox et al.*, 2015). Cloud properties directly alter radiation received by the surface. Greater cloud fraction and liquid water content result in both stronger shortwave and longwave cloud radiative effects, however, with different sensitivities (*Shupe and Intrieri*, 2004; *Bennartz et al.*, 2013). For example, clouds thicker than liquid water path of $\sim 40\,\mathrm{g\,m^{-2}}$ do not increase longwave surface warming by much, yet continue to increase shortwave surface cooling (*Bennartz et al.*, 2013). Cloud temperature, mainly controlled by cloud height, determines the longwave effect when clouds are thick enough to be completely opaque in the infrared spectrum (*Shupe and Intrieri*, 2004; *Bennartz et al.*, 2013). Cloud micro-properties and their interactions with aerosols also affect clouds' transmittance and emissivity (*Shupe and Intrieri*, 2004; *Serreze and Barry*, 2011). Solar zenith angle and surface albedo modify solar radiation availability and thus the cloud shortwave effect. For example, with the same clouds, lower surface albedo causes a stronger shortwave shading effect because of the larger albedo contrast between clouds and the surface (*Shupe and Intrieri*, 2004). Atmospheric profiles can also alter cloud influences on radiation. For example, higher below-cloud temperature and humidity reduce the longwave greenhouse effect by increasing clear-sky longwave downwelling radiation (*Cox et al.*, 2015).

The combination of these diverse cloud properties and environmental conditions result in highly heterogeneous cloud radiative effects (CRE) in the Arctic. We define CRE as the difference between all-sky and clear-sky radiative flux at the surface, so that positive CRE warms the surface and negative CRE cools it. Clouds usually warm the Arctic throughout most of the annual cycle, and cool the surface during a brief period in the middle of summer (*Intrieri et al.*, 2002), when the surface albedo decreases due to snow melt and metamorphism (*Flanner and Zender*, 2006). In the accumulation zone, clouds usually warm the surface because prevalent low-level liquid-containing clouds are optically thick enough to absorb longwave terrestrial radiation, yet thin enough to transmit shortwave solar radiation (*Cesana et al.*, 2012; *Bennartz et al.*, 2013). Bright surface albedo in this region further suppresses the shortwave shading effect of clouds, due to less contrast between clouds and surfaces (*Shupe and Intrieri*, 2004). In the ablation zone, clouds are relatively thicker (*Zygmuntowska et al.*, 2012) and surfaces are darker (*Perovich et al.*, 2002), amplifying the shortwave shading effect of clouds. However, so far, no observations nor simulations allow a reliable and comprehensive depiction of CRE magnitudes and variabilities in the Arctic.

To make the relationship between clouds and the Arctic warming more complicated, clouds also response to or interact with other warming causes and consequences, with large uncertainty. The warm southerly advection can also bring moisture into the Arctic when coincides with atmospheric rivers (*Neff et al.*, 2014), enhancing low-level clouds (*Curry et al.*, 1996; *Shupe et al.*, 2013a; *Tjernström et al.*, 2014). On the other hand, warm and dry southerlies might reduce the overall cloudiness (*Hofer et al.*, 2017). Over newly formed open water, low-level clouds increase during early fall, with less static stability and greater air-sea temperature gradients, however, not in summer (*Kay and Gettelman*, 2009; *Vavrus et al.*, 2010). Moreover, increased cloudiness can enhance broadband snow albedo since clouds preferentially absorb radiation in the near infrared spectrum where snow albedo is low *Gardner and Sharp* (2010). These interactions trigger multiple cloud-related feedbacks, the magnitudes and variabilities of which are largely unknown, making CRE predictions even more challenging.

1.2 A paucity of data

Estimating CRE requires measurements of surface radiation on both clear and cloudy days. However, satellites cannot retrieve surface radiation on cloudy days. In situ measurements are plagued with difficulties due to the harsh environments and special surface conditions. Many gridded datasets such as satellite observations, reanalyses, and model simulations include the cloud and radiation fields necessary to study CRE variabilities on large spatial scales. Nevertheless, they all have technical difficulties in the snow-covered Arctic. For satellite products, surface radiation is estimated with remotely sensed cloud properties. It is inherently hard for passive sensors to detect clouds over bright and cold surfaces, especially with frequent temperature inversions and varying topography under dim or no insolation due to the large zenith angle. These conditions cause fluctuations in the near infrared spectrum that make a simple threshold between clouds and snow impossible. The moderate-resolution imaging spectroradiometer (MODIS) underestimates cloud cover by up to 20% during polar night compared to a space lidar (*Ackerman et al.*, 2008). Active sensors can provide overall more accurate instantaneous cloud observations, since radars and lidars do not depend on insolation (*Cesana and Chepfer*, 2012; *Chan and Comiso*, 2013; *Kay and L'Ecuyer*, 2013; *Henderson et al.*, 2013). However, in a two-year comparison throughout the Arctic, MODIS captured near-surface thin clouds that were sometimes missed by the Cloud-Aerosol Lidar with Orthogonal Polarization (CALIOP) (*Chan and Comiso*, 2013). Moreover, climatologies derived using active sensors can contain considerable errors due to their limited spatial-temporal sampling (*Liu*, 2015). Modern reanalyses that assimilate satellite products inherit the deficiencies of their inputs. The prognostic cloud schemes used by reanalyses and climate models further suffer from an incomplete understanding and representation of Arctic cloud physics. To make the situation worse, the accuracy and uncertainties in these gridded cloud products are largely unknown because they have not been systematically evaluated against in-situ observations.

Although in-situ measurements provide valuable cloud and radiation baselines to evaluate gridded datasets, they are generally too sparse in time and space. For example, the Surface Heat Budget of the Arctic Ocean (SHEBA) experiment with complementary cloud and radiation observing instruments on-board a station drifting with ice in the central Arctic first measured the annual cycle of CRE in the Arctic (*Intrieri et al.*, 2002). Unfortunately, comprehensive in-situ campaigns like SHEBA, the First ISCCP (International Satellite Cloud Climatology Project) Regional Experiment (FIRE), and the Arctic Summer Cloud Ocean Study (ASCOS), usually last no more than a year (*Randall et al.*, 1998; *Curry et al.*, 2000; *Tjernström et al.*, 2014). For relatively long-term cloud observations, there are five atmospheric observatories inside the Arctic with two on the North Slope of Alaska, one in the Canadian archipelago, one at Summit, Greenland, and one on the coast of Svalbard (*Shupe et al.*, 2011). This coverage is far from sufficient considering the vast territory and diverse topography of the Arctic. For example, inside Greenland, the largest island in the world with a peak altitude over 3000 m, satellite-based cloud retrievals can only be ground-truthed at one station, Summit (*Shupe et al.*, 2013b; *Lacour et al.*, 2017).

The 30+ automatic weather stations (AWS) spreading through both the ablation and accumulation zones of Greenland provide another estimate for CRE. These AWS observe surface radiative fluxes and regular meteorological variables. Facilitated by a Column Radiation Model (CRM) (*Zender*, 1999), CRE, defined as the difference between all-sky and clear-sky radiative fluxes, can be estimated to assess the impacts of clouds on surface energy budget.

1.3 Challenges of using automatic weather stations

There are two major networks operating AWS in Greenland since 1995, the Greenland Climate Network (GC-Net) (*Steffen et al.*, 1996) and the Programme for Monitoring of the

Greenland Ice Sheet (PROMICE) (*van As and Fausto*, 2011). Measurements from these networks are used in many studies (*Fettweis*, 2007; *Wang and Zender*, 2010a; *van den Broeke et al.*, 2011; *Kuipers Munneke et al.*, 2011; *Box et al.*, 2012; *van As et al.*, 2014). However, since the stations are usually left unattended in the field for at least one year at a time, and their radiometers are not equipped with shading or ventilation confined by battery performance at these extreme temperatures, the measured radiative fluxes contain considerable biases (*Stroeve et al.*, 2001; *van den Broeke et al.*, 2004).

The typical problems include station tilt, low cosine response at large solar zenith angles, icing and riming on sensor domes, sensor overheating, and random micro-scale environmental noise (*van den Broeke et al.*, 2004; *Stroeve et al.*, 2005).

The primary source of the bias in the shortwave measurements is the instrument leveling (i.e., sensor tilt) (*van den Broeke et al.*, 2004; *van As*, 2011; *Stroeve et al.*, 2013). Differential snow-melt and compaction as well as glacier movement (Andreas Peter Ahlstrøm, 2015: personal communication) around the station towers and/or cable anchors can cause stations to drift and tilt over time. Tilted sensors will result in either underestimates or overestimates of radiation measurements, depending on the combination of tilt angles and tilt directions. Shortwave measurements are highly sensitive to sensor tilt. Theoretically, a tilt angle of 1° towards 40°N will induce a $\sim 20\,\mathrm{W\ m^{-2}}$ bias in net shortwave radiation (*van den Broeke et al.*, 2004). Using a radiative transfer model, *Bogren et al.* (2016) estimate the albedo error introduced by a station tilt of 5° to be $\sim 13\%$. Moreover, tilt shifts the diurnal phase of radiation, suggesting that sub-daily variability will be inaccurate without correcting the tilt problem. Both *van den Broeke et al.* (2004) and *Stroeve et al.* (2013) used a 24-hour running average as a workaround. *van den Broeke et al.* (2004) further calculated net shortwave radiation by multiplying the 24-hour running average albedo with the upwelling radiation, which is less susceptible to station tilt. These workarounds provide more stable estimates of radiation and albedo. However, the only way to obtain the accurate radiation and albedo at all time-scales is to correct the tilt problem. The PROMICE stations are equipped with inclinometers that measure the north-south and east-west tilt angles. The station rotation is obtained every 1-2 years during station maintenance visits. Insolation observed by tilted AWS can then be adjusted using this information (*van As*, 2011). However, in spite of the effort to re-position the stations during each visit, the frequent station rotation, occurring together with station tilt, changes the orientation of these inclinometers, making the measured tilt angles questionable. In any case, half of the AWS in Greenland have no inclinometers at all and their tilt biases can only be estimated.

Other shortwave measurement problems, such as icing and riming on sensor domes and low cosine response, also prejudice shortwave measurements. However, the biases are either minor or can be removed by typical data quality control. An ice-coating over the sensor dome can shield part of the incoming solar radiation, causing an underestimate of net SW. On the other hand, riming on the sensor dome can increase the incoming solar radiation, especially at large solar zenith angles, due to enhanced multiple scattering of the solar radiation. This can cause an overestimate of net SW. Although the thermal mass of the pyranometers is small (*Stroeve et al.*, 2001) and the interior of ice sheets are usually high and dry, riming still happens occasionally, especially during cold seasons (*Miller et al.*, 2015). The unlikely high/low values induced by icing, riming and shadowing can be removed by detecting sudden changes of albedo since the down-looking sensors are generally less sensitive to these problems. The cosine response error at large solar zenith angles is intrinsic, and variable with instrument types and manufacturers. Using an intermediate resolution spectrophotometer, *Grenfell et al.* (1994) found the departures of measurements from an ideal cosine law were less than 15% at solar zenith angles less than 72°. Using a Brewer spectroradiometer in UV band, *Bais et al.* (1998) reported a cosine error range from 2% to 7%. One AWS project in Greenland, the Greenland Climate Network, employs LI-COR 200SZ pyranometers. *Stroeve et al.* (2001) observed deviations of this pyranometer from highly accurate instruments in excess of 5% at solar zenith angles larger than 75°. *van den Broeke et al.* (2004) obtained negative net shortwave radiation measurements at high solar zenith angles using Kipp & Zonen CM3 pyranometers, equipped by the other two Greenland AWS projects, K-transect project and the Programme for Monitoring of the Greenland Ice Sheet networks. According to the manufacturer report, the typical percentage deviation of Kipp & Zonen CM3 from ideal cosine behavior is $\sim 2\%$ at solar zenith angle of 80°, with a maximum of $\sim 8\%$, which is on the same magnitude of that of LI-COR 200SZ (*Kipp & Zonen*, 2004). The newer version of LI-COR pyranometer, LI-200R, claims a typical cosine error of less than 5% up to solar zenith angle of 82° (*Biggs*, 2015). None of the cosine errors reported above exceeds the mean tilt-induced biases as we document below.

For longwave radiation, the most important bias source is the window overheating (*van den Broeke et al.*, 2004). Up-looking pyrgeometers without shading or ventilation can be improperly heated by solar radiation by up to $25\,\mathrm{W\ m^{-2}}$ of $1000\,\mathrm{W\ m^{-2}}$ of solar insolation. It is hard to calculate the true bias even if the dome temperature is known, since it is impossible to distinguish heating from the measured longwave radiation and heating from the undesired shortwave radiation. Natural shading (i.e., clouds) and ventilation (i.e., wind) can mitigate though not eliminate this problem.

In order to take advantage of the relatively long-term measurements from multiple AWS, we must ameliorate biases in shortwave radiation caused by station tilt and in longwave radiation caused by window over-heating.

1.4 Organization of research

The remainder of this dissertation is organized as follows: in Chapter 2, we correct the station tilt problem, using a new method—the Retrospective, Iterative, Geometry-Based (RIGB) tilt correction method—that depends only on solar geometry and no additional instrumentation, to produce more consistent shortwave radiation (thereafter, SW) measured by AWS. We evaluate the adjusted insolation against satellite products and reanalysis, and present the improved surface albedo on diurnal, monthly, and annual time scales. In Chapter 3, we use the tilt-corrected AWS observations, apply rigorous data quality control procedures to minimize influences from window over-heating, and estimate melt-season CRE from 2008–2013. We then assess the leading factors that determine CRE on hourly and semi-monthly timescales. In Chapter 4, we use our bias-corrected AWS CRE estimates to evaluate the verisimilitude of CRE spatial distributions from five well known gridded datasets during the melt seasons from 2008-2013. We explain the discrepancies in terms of physical properties relevant to the cloud-surface-radiation interactions that determine CRE. Chapters 2, 3, and 4 are from a published paper and ready-to-submit manuscripts and thus can be read individually.

Chapter 2

Tilt correction for radiation observed by automatic weather stations

2.1 Introduction

Surface melt and mass loss of the Greenland Ice Sheet may play crucial roles in global climate change due to their positive feedbacks and large fresh water storage. With few other regular meteorological observations available in this extreme environment, measurements from Automatic Weather Stations (AWS) are the primary data source for studying surface energy budgets, and for validating satellite observations and model simulations. Station tilt, due to irregular surface melt, compaction and glacier dynamics, causes considerable biases in the AWS shortwave radiation measurements. In this study, we identify tilt-induced biases in the climatology of surface shortwave radiative flux and albedo, and retrospectively correct these by iterative application of solar geometric principles. Section 2.2 and 2.3 describe the datasets we use, and RIGB method to estimate tilt angle-direction and to adjust SW. In Section 2.4, we evaluate our adjusted insolation against satellite observations and reanalysis at all stations, and against data from PROMICE stations, which were adjusted by the inclinometer-measured tilt angles. To what degree station tilt affects the diurnal phase and magnitude of insolation are also revealed in this section. In Section 2.5, we present the observed diurnal variability of albedo over Greenland for the first time, and show the improvement of the monthly and annual climatology using the adjusted SW. In Section 2.6, we explore the dominant factors for station tilt, and discuss the possible limitations and uncertainties of RIGB method, followed by our conclusions.

2.2 Data

AWS used in this study are from three networks: Greenland Climate Network (GC-Net), the Kangerlussuaq transect (K-transect) and the Programme for Monitoring of the Greenland Ice Sheet (PROMICE). The first GC-Net station was set up in 1995. By 2014, there were a total of 17 long-term AWS in GC-Net, spreading in both ablation and accumulation zones (*Steffen et al.*, 1996). Three AWS at the K-transect were initiated in 2003 (*van den Broeke et al.*, 2011), with one more station added in 2010. Since 2007, PROMICE set up 22 AWS in succession, arranged mostly in pairs with one station in the upper ablation zone near the equilibrium line and the other at a lower elevation well into the ablation zone (*van As and Fausto*, 2011).

In this study, we correct the sensor tilt problem in surface SW data observed by AWS from all three aforementioned datasets during melt seasons (i.e., May–Aug) from 2008 to 2013, when data at most of the stations are available. Stations with more than two years of missing data are excluded from consideration, including Crawford Point1, GITS, NASA-U and Petermann Gl. from GC-Net, s6 from K-transect, and MIT, QAS_A and TAS_A from PROMICE. The remaining number of stations is 35, of which 13 stations are from GC-Net, 3 from K-transect and 19 from PROMICE (Fig. 2.1). The radiative flux from these datasets is hourly average. We synchronize all three datasets to account the fact that the time stamp of GC-Net and K-transect is half an hour after the interval mid-point (i.e., data stamped as 8 am represent the average from 7 to 8 am); the one of PROMICE is half an hour before the interval mid-point (i.e., data stamped as 8 am represent the average from 8 to 9 am). PROMICE also provides adjusted SW by measured tilt angles at their stations, which can be used as a reference for our method. However, this PROMICE product has not been corrected for the inclinometer orientation shift yet.

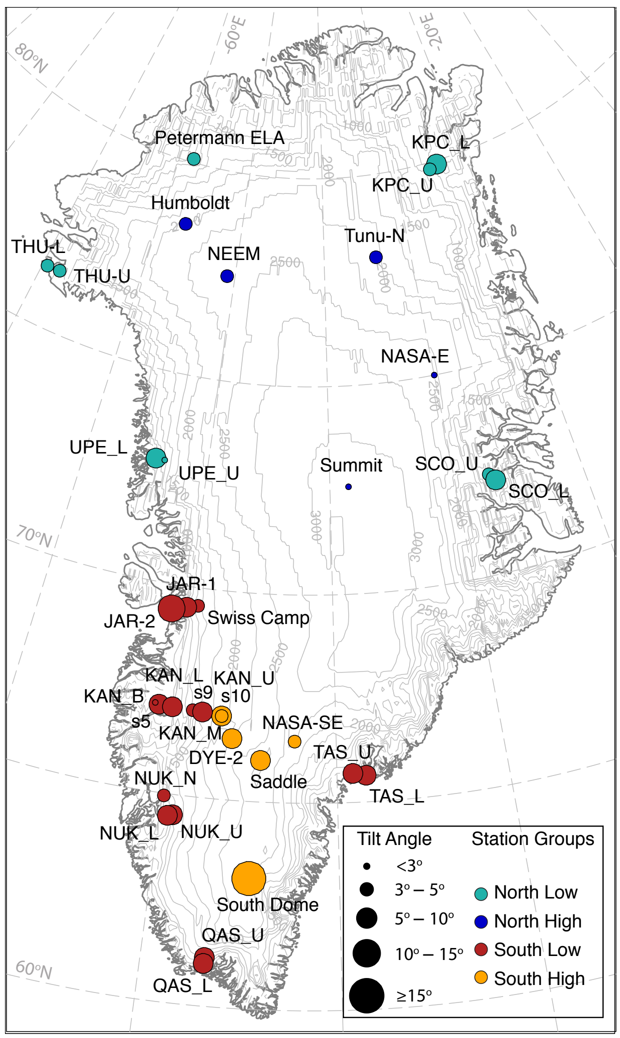

Figure 2.1: The automatic weather stations used in this study and their average tilt angles (β). Stations are separated into four groups based on their latitudes and altitudes.

We also use insolation from the Clouds and the Earth's Radiant Energy System (CERES) (*CERES Science Team*, 2017) and the Modern-Era Retrospective Analysis for Research and

Applications (MERRA) (*Rienecker et al.*, 2011) as references to evaluate RIGB adjustments. CERES instruments are now aboard three satellites, including Terra, Aqua and the Suomi National Polar-orbiting Partnership (S-NPP) observatory. They measure both solar-reflected and Earth-emitted radiation from TOA, and derives solar radiative fluxes at Earth surface. The insolation we use is Synoptic Radiative Fluxes and Clouds (SYN) Edition-3A Level-3 data, the spatial and temporal resolution of which are 1°and 3 hours, respectively. MERRA is the new generation of reanalysis, which uses the Data Assimilation System component of the Goddard Earth Observing System. It provides near-real-time hourly climate analysis with 1/2° in latitude and 2/3° in longitude.

2.3 Method

Based on the geometric relationship between the tilted insolation observations and simulations on a horizontal surface on clear days, we deduce tilt angles and directions, and then use them to correct the tilt-induced biases on the neighboring cloudy days. The detailed processes are summarized in Fig. 2.2. All the variables used in this section are listed in

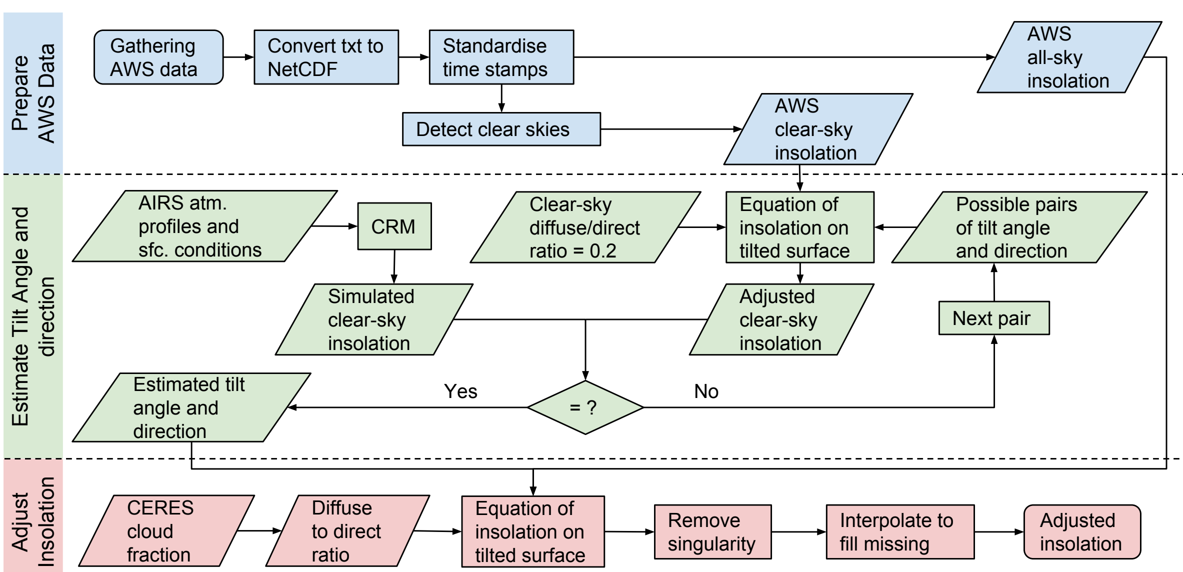

Figure 2.2: RIGB workflow.

Table 2.1.

Table 2.1: Variables used in Section 2.3

Variable	Description
I_h	Shortwave radiation on a horizontal surface, W m^{-2}
I_t	Shortwave radiation on a tilted surface, W m^{-2}
$I_{b,h/t}$	Beam radiation on a horizontal/tilted surface, W m^{-2}
$I_{d,h/t}$	Diffuse radiation on a horizontal/tilted surface, W m^{-2}
$I_{r,t}$	Reflected radiation from a nearby horizontal surface on a tilted surface, W m^{-2}
β	Tilt angle, radians
a_w	Tilt direction, radians
z	Solar zenith angle observed from a horizontal surface, radians
i	Solar zenith angle observed from a tilted surface, radians
a_s	Solar azimuth angle, radians
C	Diffuse ratio
ρ	Surface albedo approximation
CF	Cloud fraction

2.3.1 Surface radiative flux simulation

We use a Column Radiation Model (CRM), the stand-alone version of the radiation model in Community Atmosphere Model 3 (CAM3) updated from *Zender* (1999), to simulate surface radiative flux on clear days based on atmospheric profiles and surface conditions. Here we use atmospheric temperature profiles and humidity profiles, and surface conditions (except surface albedo) from the Atmospheric Infrared Sounder (AIRS) (*AIRS Science Team/Joao Texeira*, 2013). Its Infrared and Micro-Wave (IR/MW) sounding instruments retrieve reliable profiles even near the surface (*Susskind et al.*, 2003). Atmospheric constituents with little variability, such as O_3 and Aerosol Optical Depth are set to values from a sub-Arctic standard atmosphere (Table 2.2).

Table 2.2: CRM Parameters.

Parameter	Unit	Value
Number of vertical levels	layer	100
Ozone column mass path	DU	348.64
Aerosol visible extinction optical depth in North		0.12
Aerosol visible extinction optical depth in South		0.14
Solar constant	W m^{-2}	1367.0

2.3.2 Radiation on a tilted surface

SW on a tilted surface comprises of three parts: direct radiation or beam radiation ($I_{b,t}$), diffuse radiation ($I_{d,t}$) and reflected radiation from a nearby horizontal surface ($I_{r,t}$). These three parts can be calculated separately from tilt angle (β) and tilt direction (a_w), time and place, and SW on the horizontal surface (I_h), assuming isotropic reflection at the surface (*Goswami et al.*, 2000). First, the direct radiation ($I_{b,t}$) is calculated from the direct part of SW on the horizontal surface ($I_{b,h}$) and the solar zenith angle observed on the tilted surface (i), as below:

$$I_{b,t} = I_{b,h} \cdot \cos i \tag{2.1}$$

$I_{b,h}$ is known from the true solar zenith angle (z) and the diffuse ratio (C):

$$I_{b,h} = \frac{I_h}{\cos z + \mathrm{C}} \tag{2.2}$$

$\cos i$ follows the geometric relationship with the true solar zenith angle (z), solar azimuth angle (a_s), tilt angle (β) and tilt direction (a_w):

$$\cos i = \sin z \cdot \cos (a_s - a_w) \cdot \sin \beta + \cos z \cdot \cos \beta \tag{2.3}$$

We calculate solar declination used to estimate solar zenith angle (z) and azimuth angle (a_s) using algorithm from *Reda and Andreas* (2004).

The diffuse radiation on a tilted surface ($I_{d,t}$) can be calculated by multiplying diffuse radiation on a horizontal surface ($C \cdot I_{b,h}$) by the view factor between the sky and the tilted surface, as below (assuming isotropic diffuse radiation):

$$I_{d,t} = \mathrm{C} \cdot I_{b,h} \cdot (1 + \cos\beta)/2 \tag{2.4}$$

Part of the upwelling radiation from a nearby horizontal surface can be intercepted by the tilted surface. This reflected radiation on the tilted surface ($I_{r,t}$) can be obtained by multiplying upwelling radiation from the horizontal surface ($\rho \cdot I_h$) by the view factor between the horizontal surface and the tilted surface (assuming isotropic reflected radiation):

$$I_{r,t} = \rho \cdot I_h \cdot (1 - \cos\beta)/2 \tag{2.5}$$

Where ρ is an approximation of surface albedo. A value of 0.8 is used here for snow covered ground as suggested by *Goswami et al.* (2000).

The relation between SW measured by the tilted sensor (I_t) and SW on the horizontal surface simulated by CRM (I_h) can be summarized as:

$$I_t = \frac{I_h}{\cos z + \mathrm{C}} \cdot [\cos i + \mathrm{C} \cdot (1 + \cos\beta)/2 + \rho \cdot (\cos z + \mathrm{C})(1 - \cos\beta)/2] \tag{2.6}$$

where C is 0.25 for insolation on clear days. The relatively larger value of C used here includes the effects of undetected clouds (*Harrison et al.*, 2008).

2.3.3 Estimate of tilt angle and direction

The SW provided by the three datasets used in this study could include all the AWS measuring problems of icing, riming, shadowing, cosine response error and sensor tilt. AWS from

GC-Net use the LI-COR 200SZ pyranometer, which has a better resistance to rime formation than the standard thermopile pyranometers (*Stroeve et al.*, 2005), due to its small thermal mass. *van den Broeke et al.* (2004) found the Kipp & Zonen CM3 pyranometer, used by AWS from K-transect and PROMICE, less susceptible to riming, since it only has a single dome (rather than double domes), which can be heated up by solar radiation together with the black sensor plate to prevent rime formation. Furthermore, using only clear days with perfect cosine curves to estimate tilt angle-direction helps remove the effects of icing, riming and shadowing. Although the numerical solutions of tilt angle-direction are most sensitive to insolation at solar noon, in order to further limit effect of cosine response error, we only use data at solar zenith angles smaller than 75°, when the cosine response error is typically less than 5% (*Kipp & Zonen*, 2004; *Biggs*, 2015; *Stroeve et al.*, 2001). We assume, therefore, the residual bias is mainly caused by sensor tilt, with an uncertainty in device measurement and random environmental noise. The best tilt angle-direction pair, (β, a_w), is chosen as the pair which produces the surface insolation with the correct shift in phase ($\pm\,0.5$ hours) and the smallest absolute error in magnitude compared with CRM simulations.

2.3.4 Data adjustment

The best tilt angle-direction pair estimated using insolation on all the clear days in one month is used to adjust radiation of that whole month. However, there are cases in which tilt angle changes several degrees in a month. If the standard deviation of RIGB adjustments on different clear days using this one pair of tilt angle-direction is larger than $5\,\mathrm{W\ m^{-2}}$, this month will be divided into shorter time periods and processed separately. To adjust insolation on both clear and cloudy days (i.e., calculate radiation on the horizontal surface I_h from that on the tilted surface I_t), Eq. 2.6 shown previously is used with the diffuse ratio

(C) calculated by the cloud fraction (CF) from CERES (*van As*, 2011).

$$\mathrm{C} = \frac{0.25 + \mathrm{CF}}{1 - \mathrm{CF}} \tag{2.7}$$

Since the improvements in the shortwave upwelling radiation are negligible for the tilt angle range estimated in this study, no tilt correction is performed on it. Although only insolation at solar zenith angles less than 75° is used to estimate station tilt, SW data at all solar zenith angles are adjusted, with physically impossible (i.e., insolation at surface larger than at TOA; or albedo larger than 0.99) and suspicious data (i.e., a sudden change in albedo) excluded. Missing data points with both adjoining sides of data available are filled with linear interpolation.

2.4 Validation

Station tilt affects both the phase and magnitude of the diurnal variability of surface radiative flux. The phase shift can be discerned by comparing the time of observed insolation maximum with solar noon time under clear-sky conditions. The solar noon time at one station is known from its longitude and the date (*Goswami et al.*, 2000; *Reda and Andreas*, 2004). There is a frequent shift of maximum insolation time against solar noon in the unadjusted AWS measurements at most stations (Fig. 2.3). On fewer than 40% of all clear days, insolation peaks within ±0.5 hours of solar noon. Some of the shifts are larger than 3 hours. On the other hand, over 60% of the RIGB-adjusted insolation peaks at solar noon. The maximum shift is ± 0.5 hours.

The improvements in AWS insolation are further evaluated by comparing unadjusted AWS data with RIGB-adjusted data and with the PROMICE adjustment against the CERES (*CERES Science Team*, 2017) and MERRA retrievals (*Rienecker et al.*, 2011). The AWS

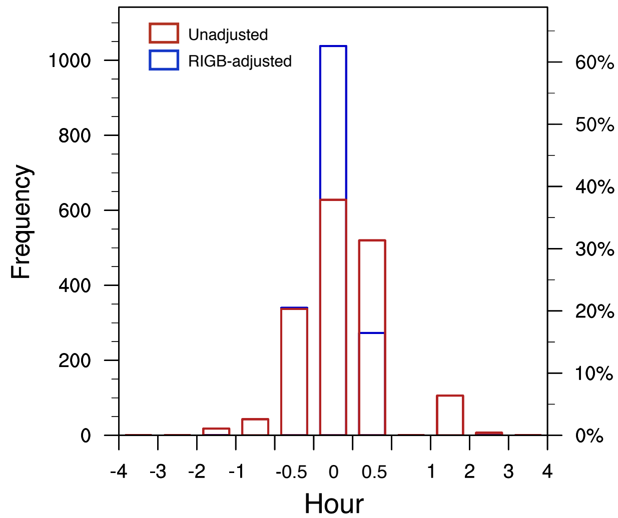

Figure 2.3: Shifts of maximum insolation time to solar noon in unadjusted data and RIGB adjustment. The bins of solar noon time are non-linear with a minimum of 0.5 h.

from PROMICE are equipped with inclinometers that record the station tilt angles. The tilt-corrected data are provided whenever inclinometers worked, with no correction on the inclinometer orientation yet. We compare AWS observations with data in the nearest CERES and MERRA grid. Comparisons are only conducted between 6 A.M. and 6 P.M. at local solar time, since the extrapolation of data in the early mornings and late nights—when most of the data are removed due to icing and low sensitivity problems—is problematic.

RIGB adjustment better agrees with both CERES and MERRA, relative to the unadjusted data and PROMICE adjustment (Fig. 2.4). At PROMICE stations, the RIGB Root-Mean-Square-Errors (RMSE) against CERES and MERRA are $\sim 20\,\mathrm{W\ m^{-2}}$ smaller than the RMSE of the unadjusted data, and are also smaller than the RMSE of the PROMICE adjustment (Fig. 2.4a and b). Correlations of RIGB with CERES and MERRA are the strongest. Their correlation coefficients exceed 0.97 for both references, in contrast with the low values of the unadjusted data, which are 0.93 for CERES and 0.94 for MERRA. The ones of PROMICE adjustment are in-between: 0.96 for both reference datasets. The RIGB-adjusted insolation also better agrees with the references at GC-net and K-transect stations, with $\sim 10\,\mathrm{W\ m^{-2}}$ less RMSE relative to the unadjusted data, and correlation coefficients over 0.95 (Fig. 2.4c and d). Under all-sky conditions, the improvements in RMSE are over 20 W m^{-2} for both CERES and MERRA, although the absolute biases are larger (Table 2.3). We also notice a systematic difference of almost 50 W m^{-2} between CERES and MERRA. These large bias and systematic difference could be caused by the inaccurate estimates of cloud properties by the satellite instrument (i.e., CERES) and reanalysis (i.e., MERRA). Nevertheless, RIGB adjustment shows better consistencies with both references, because our adjustment is on the daily time-scale, which is shorter than that of this systematic difference.

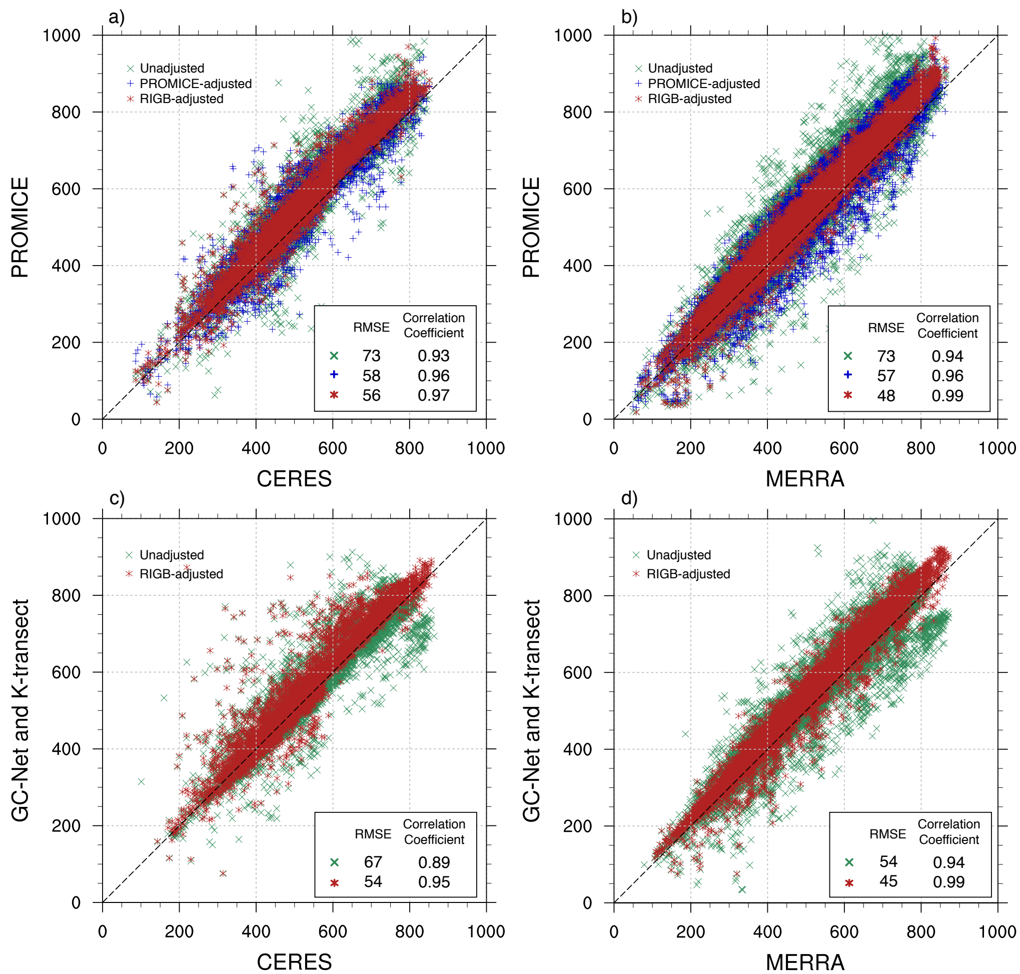

Figure 2.4: Correlation of insolation (W m^{-2}) on clear days between a) PROMICE with CERES; b) PROMICE with MERRA; c) GC-Net and K-transect with CERES; d) GC-Net and K-transect with MERRA.

Table 2.3: RMSE of AWS against the reference datasets under all-sky conditions (W m^{-2}). (Numbers in the parentheses are the percentage of changes relative to the unadjusted data.)

AWS	Reference	Unadjusted	PROMICE Adjustment	RIGB Adjustment
PROMICE	CERES	146	115 (-21%)	101 (-31%)
	MERRA	184	152 (-17%)	150 (-18%)
GC-Net & K-transect	CERES	99		77 (-22%)
	MERRA	154		101 (-34%)

To illustrate the agreement between the PROMICE measured and RIGB estimated tilt angles, we next compare these angles at Station KPC_U, where the station rotation is small according to the field notes taken on revisits. The hourly north-south and east-west tilt angles measured by inclinometers are converted to tilt angle-direction format, assuming no station rotation, and then averaged over a month. The measured and estimated tilt angle-direction agree reasonably well (Fig. 2.5). The year-to-year relative positions are the same. The maximum absolute differences in the tilt angle and direction are 2.24° and 33.35°, with a Root-Mean-Square-Difference (RMSD) of 1.09° and 14.19°, respectively. The resulting RMSD in insolation adjustment is 6 W m^{-2}.

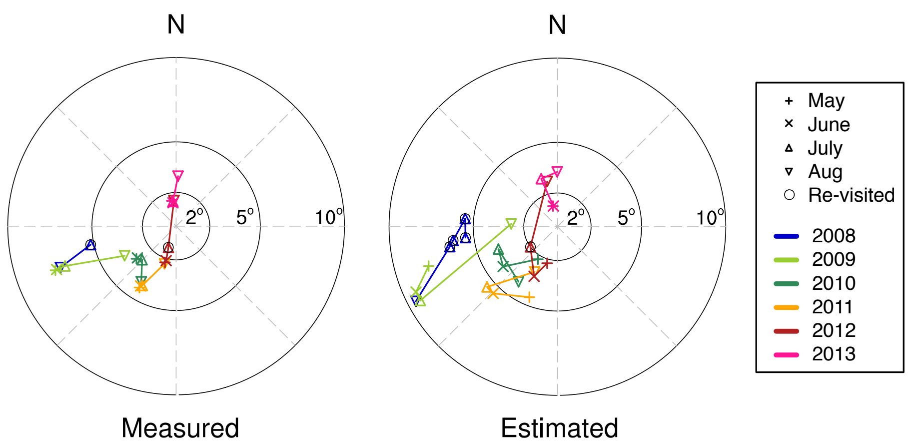

Figure 2.5: Measured and estimated tilt angle-direction at Station KPC_U. The distance from the circle center represents the station tilt angle (β). The direction represents the station tilt direction (a_w) with 0° pointing to the south. The markers are circled in black if the station was re-visited in those months.

Table 2.4: Daily average improvements in insolation. (Numbers in the parentheses are the percentages of the absolute differences relative to the unadjusted insolation. Column 5 is the hourly average of absolute difference between unadjusted data and RIGB adjustment, not the difference between Column 3 and 4.)

Zone	Condition	Unadjusted (W m^{-2})	RIGB adjustment (W m^{-2})	Absolute Difference (W m^{-2})
Accumulation	All-Sky	295	350	13 (4%)
	Clear-Sky	326	395	51 (16%)
Ablation	All-Sky	284	322	10 (4%)
	Clear-Sky	346	428	44 (13%)

The largest improvement of our tilt correction (i.e., RIGB adjustment minus unadjusted data) occurs at South Dome, with a daily average of 32 W m^{-2} under all-sky conditions and 84 W m^{-2} under clear-sky conditions. Although the tilt angles are more variable in the ablation zone (i.e., altitude $<$ 1800 m), the absolute values are larger in the accumulation zone (i.e., altitude *geq* 1800 m), caused by the large systematic tilt at each of the southern stations. Therefore, our method improves the insolation more in the accumulation zone (13 W m^{-2}) than in the ablation zone (10 W m^{-2}; Table 2.4). The average daily improvement of all stations under all-sky conditions is $\sim$ 11 W m^{-2}, which is equivalent to a snow melt in liquid of 0.24 m throughout the melt season, using an albedo of 0.7 for melting snow.

2.5 Impact on snow surface albedo

Snow albedo controls the absorbed solar radiation at the surface. Short-term changes in albedo can lead to snow-melt and trigger the positive snow-albedo feedbacks. Little is known about the sub-daily variabilities of albedo in the Arctic, due to a lack of high-temporal-resolution satellite observations and reliable *in situ* measurements. Although the polar-orbiting satellites instrument such as MODIS pass over parts of Greenland several times a day, only daily average albedo is available mainly due to cloud interference. The cosine response error and the sensor tilt can introduce false diurnal fluctuations into AWS observed albedo. In climate models, the diurnal change of snow albedo is typically simulated as a function of solar zenith angle and snow grain size (*van den Broeke et al.*, 2004; *Flanner and Zender*, 2006). In reality, more factors contribute to this diurnal change, including internal properties (such as particle shape and snow density) and external factors (such as solar azimuth angle and topography) (*Flanner and Zender*, 2006; *Wang and Zender*, 2011). With the tilt-corrected radiation, we find a more consistent diurnal change in surface albedo. For example, the semi-smiling curves of albedo are smoother using the adjusted data (Fig 2.6a and b). At stations with large tilt angles, RIGB adjusts the diurnal variability patterns from frowning to smiling (Fig 2.6c and d). The average diurnal range (maximum minus minimum) of all stations declines from 0.18 to 0.12 with a 3-times smaller standard deviation.

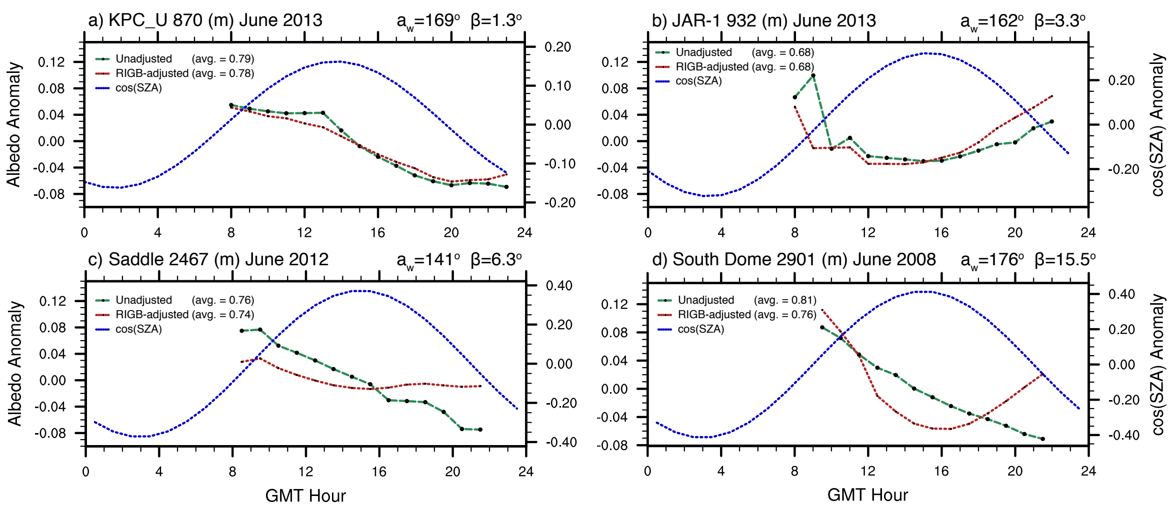

Figure 2.6: Diurnal variability of albedo at solar zenith angle less than 75° at (a) KPC_U; (b) JAR-1; (c) Saddle; (d) South Dome. The anomaly used here is the monthly average of hourly anomalies against daily averages. cos (SZA) represents the cosine of solar zenith angle. The station altitude and tilt angle-direction as well as data time period are labeled on the top of each panel.

Sometimes, the pyranometer tilts enough to jeopardize the daily average albedo, which in turn impacts climatology on long-term time scales. For example, at Station UPE_L in Northwest Greenland, the tilt angle jumped from 2.5° to 9.7° from June to July of 2010. Without tilt correction, data show an improbably higher albedo in July than in June (Fig. 2.7a), which contradicts the results from a nearby station, UPE_U (Fig. 2.7b), as well as the concurrent temperature trend. The high monthly average albedo in the unadjusted data in July 2010 was caused by the abnormally high values in the early mornings and late evenings, due to a shift in downwelling radiation against the upwelling. This misleading effect cannot be fully removed by either the 24-hour running average or limiting the solar zenith angle to less than 75°. After the tilt effect is countered, the normal climatology is restored.

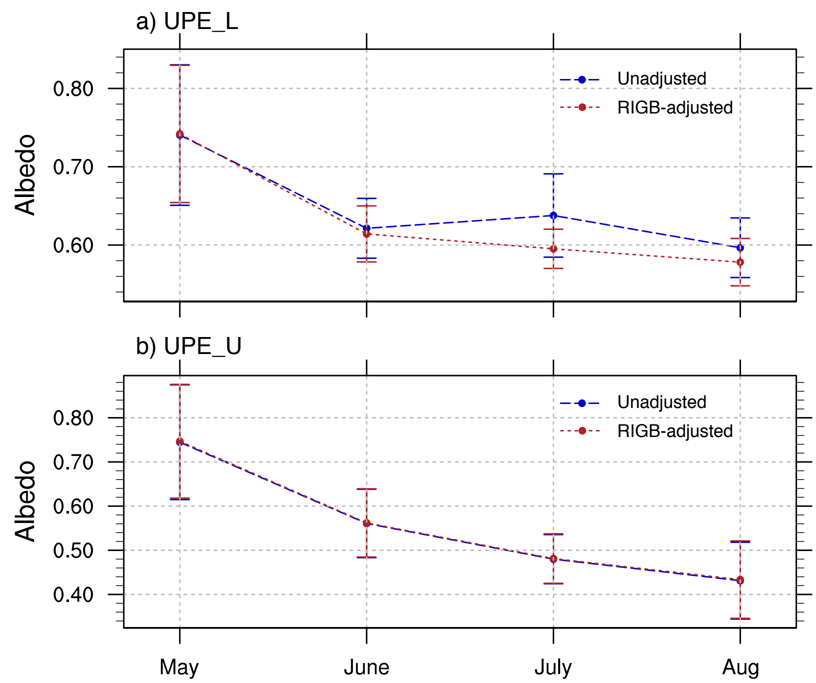

Figure 2.7: Monthly average albedo at a) UPE_L and b) UPE_U in May-Aug 2010 with standard deviation as error bars.

Sensor tilt can also affect the inter-annual variability of albedo. In 2012, Greenland experienced the largest melt extent in the satellite era since 1979 (*Nghiem et al.*, 2012), which is seen as an epic low albedo in both unadjusted and RIGB-adjusted data in the accumulation zone (Fig. 2.8a). In this area, melt only occurs during a limited period of time in the summer, and thus the tilt problem is not as serious as in the ablation zone. In despite of the large systematic tilt at the southern stations, the tilt variation is small. In the ablation zone, the unadjusted data shows the smallest albedo in 2010 instead of in 2012. Moreover, the between-station variability of the unadjusted data is almost 5 times larger than that of the RIGB-adjusted data (shown by the error bars in Fig. 2.8b), indicating varied tilt effects at different stations. After the tilt correction, the long-term trend and the albedo minimum are in agreement with the estimates from the NASA MOD10A data (*Box*, 2015).

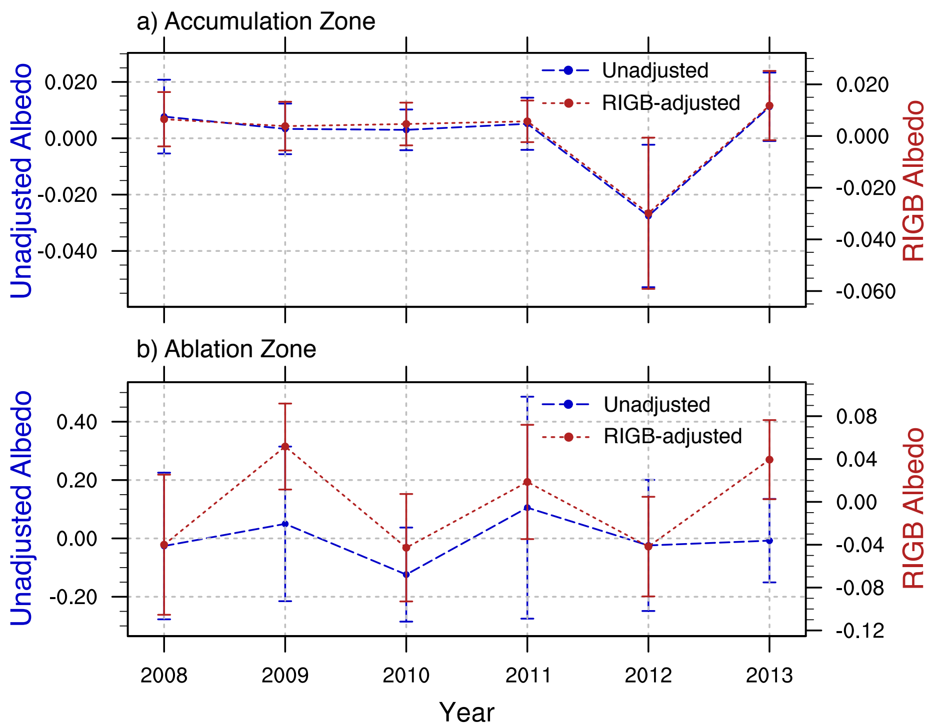

Figure 2.8: Annual average albedo using unadjusted data (on the left Y-axis) and RIGB-adjusted data (on the right Y-axis) in a) accumulation zone; b) ablation zone with standard deviation as error bars. The values are anomalies against the corresponding station averages.

2.6 Discussion

2.6.1 Station tilt

Of all the stations examined here, only KAN_B from PROMICE is anchored into rock; all others are anchored into glacier ice. The estimated tilt angle-directions reveal large temporal and spatial varieties (Fig. 2.9). At the GC-Net stations (Fig. 2.9a), there is a systematic tilt direction at each station in the accumulation zone. For example, the station at South Dome always tilts to the north, and the one at DYE-2 to the northwest. With regards to the tilt angle, both the station maximum and the temporal variability are larger in the ablation zone than in the accumulation zone, except for Station South Dome. At the PROMICE stations (Fig. 2.9b), there is no obvious systematic tilt direction. The tilt angles and their temporal variabilities are generally larger at the southern stations than in the northern stations. It seems that the tilt angles are less variable at GC-Net stations which use long poles as station masts than at PROMICE stations which use tripods instead. However, most GC-Net stations are in the colder accumulation zone, whereas all the PROMICE stations are in the warmer ablation zone. We also compare the temporal variability of tilt angles between the paired stations from PROMICE. The station at a higher altitude always has a smaller tilt angle standard deviation than the station at a lower altitude. In addition, the largest and most variable tilt angles are found in July when the snow melt intensity is strongest of the melt season (i.e., May–Aug). These all suggest a causal correlation between surface melt/compaction and station tilt.

Since snow melt intensity is not available at all AWS, surface albedo instead is used to compare with the tilt angle variability (Fig. 2.10). The significant correlation between surface albedo and station tilt variability is negative. The stations that are more northernly, at higher altitudes and with higher albedo are less affected by station tilt, whereas stations more southernly, at lower altitudes and with lower albedo are more affected. However, whether stations will tilt, and to what degree and direction also depend on environmental factors. For example, if the areas around all the anchors melt at a similar rate, the station tilt may not be as serious as one with melting that occurs only in the area around one anchor. This may explain why the correlation coefficient is relatively low (-0.58). The significant correlation between near-surface atmospheric temperature and the station tilt variability is negative as well (-0.52). The fact that thermometers from different projects are not set to the same height above the surface may contribute to this lower coefficient. Nevertheless, it is highly probable that the station tilt is controlled by surface melt/compaction. As the tilt angle gets larger, more environmental factors take effect.

We also found a weak negative correlation between station tilt and wind speed (i.e., the higher the wind speed, the smaller the tilt variability). However, this could be explained by the co-occurrence of high albedo and high wind speed at high-altitude stations. Moreover, no correlation is found between the systematic tilt directions of GC-Net stations in the accumulation zone and their dominating wind directions. These systematic tilt directions could be a result of the local slopes or glacier dynamics (Konrad Steffen, 2015: personal communication).

2.6.2 Dependence on clear days

The RIGB method requires clear days to perform the tilt estimation. With current precision, at least one clear day is needed per month. Among all the 840 station-months used in this study (i.e., 35 stations, 6 years per station and 4 months per year), there are 33 station-months (3.93%) with no clear days to use. However, most of these (31 out of 33) have at least half of the AWS measurements missing. Only 2 of the 840 station-months was too cloudy to have any clear days. We therefore provide no correction during that month. Another potential limit of RIGB is that it requires more clear days to accurately capture station tilt when the inter-month variability is large.

2.6.3 Uncertainty in the tilt-corrected insolation

The surface insolation simulation using CRM driven by AIRS profiles under clear-sky conditions are validated against Atmospheric Radiation Measurements (ARM) at Barrow, Alaska, U.S.A (*Atmospheric Radiation Measurement (ARM) Climate Research Facility*, 1994). Since we use a constant Aerosol Optical Depth (AOD), only insolation in May is used in order to eliminate the interference of wild fires. From 2008 to 2013, the hourly average difference between the measured and simulated insolation is 5±3 W m^{-2}, which is less than 2±1% of the daily average.

The data quality of the tilt-corrected insolation under all-sky conditions also relies on the quality of cloud fraction data. Higher cloud fraction results in a higher diffuse ratio (C). With more isotropic diffuse radiation, insolation is less susceptible to station tilt. Therefore, if the cloud fraction is under-estimated, the insolation will be over-corrected; vice versa. In the Arctic, the fast-changing convective clouds are rare, so we use the 3-hourly cloud fraction from CERES. With regards to the cloud radiative properties, CERES estimates are reasonably accurate (*Minnis et al.*, 2011). In the Arctic, the average difference between the *in situ* ground-measured and CERES cloud fraction is ~ 0.15 (*Minnis et al.*, 2008). The effect of cloud fraction on the insolation adjustment depends on both the tilt angles and directions (Fig. 2.11). The adjustment at local solar noon is largest when the station tilts to the north ($a_w = 180°$) or south ($a_w = 0°$). The maximum of daily average turns clockwise, e.g., to $a_w = 30°$ and $a_w = -150°$ when the tilt angle (β) is 10°. The adjustment becomes smaller when stations tilt less, or cloud fraction is close to 1. In the worst situation when stations tilt to 30° or 210° and the cloud fraction is close to 0, the uncertainty in insolation adjustment caused by cloud uncertainty is up to 7.5 W m^{-2} at a tilt angle of 10°. In 90% of the station-months we used, tilt angles are less than 10°, 95% less than 15°. The average cloud fraction in the Arctic during summertime is 0.81 (*Vavrus et al.*, 2008). Therefore, the uncertainty in insolation adjustment caused by the uncertainty in cloud fraction should be well below 10 W m^{-2}, the magnitude of the adjustment itself. Nevertheless, a cloud fraction dataset with a higher resolution would further benefit the quality of the hourly radiation measurements from AWS.

The AWS used in these three projects over Greenland Ice Sheet measure only broadband radiation. We, therefore, use a wavelength-integrated relationship between diffuse ratio (C) and cloud fraction (CF), derived from broadband radiation measurements using linear regression. Regression models using higher orders or more predictors, such as relative humidity, do not perform significantly better (*Paulescu and Blaga*, 2016). Also, there is no significant difference in the calculation of radiation on tilted surface by using diffuse radiation estimated from a diffuse fraction correlation or retrieved from observations (*Reindl et al.*, 1990). Although tilt-induced errors are independent of wavelength for direct radiation, they vary with wavelength for diffuse radiation (*Bogren et al.*, 2016). The diffuse/direct ratio (C) also increases with shorter wavelengths (*Hudson et al.*, 2006; *Bogren et al.*, 2016). The equations in Section 3 could be instead written as function of wavelength with diffuse ratio, C(λ), and radiation fluxes, $I(\lambda)$. Therefore, if narrow-band measurements of shortwave radiation and the corresponding diffuse ratios are available, RIGB can be applied to correct spectral tilt-induced errors.

2.7 Conclusions

In this study, we identify and correct the SW tilt bias using tilt angles and directions estimated by comparing CRM simulated insolation with AWS observed insolation under clear-sky conditions. Station tilt causes considerable bias in insolation. On fewer than 40% of clear days, the unadjusted insolation peaks at the correct solar noon time ($\pm$0.5 hours). The largest bias exceeds 3 hours. The unadjusted insolation RMSE against CERES and MERRA at all stations are as large as $\sim 70\,\mathrm{W\ m^{-2}}$ under clear-sky conditions, with a correlation coefficient of ~ 0.90. Using the estimated tilt angle-directions, which are in a good agreement with the measured tilt angles, RIGB adjustment reduces the RMSE by $16\,\mathrm{W\ m^{-2}}$, and enhances the correlation coefficients to above 0.95. The overall improvement relative to the unadjusted data under all-sky conditions is $11\,\mathrm{W\ m^{-2}}$, which is enough to melt 0.24 m snow water equivalent using an albedo of 0.7. With this tilt-corrected SW data, we found a consistent semi-smiling diurnal cycle of albedo in Greenland. The derived seasonal and inter-annual variabilities of albedo agree better with satellite observations and temperature changes. This RIGB tilt correction method relies only on the iterative application of solar geometric principles, that requires no additional instrumentation. Therefore, it can retrospectively solve the tilt problems in SW measurement, and provides multi-year consistent SW for the analysis of surface energy budgets and melt as well as validation of satellite observations and model simulations on Greenland Ice Sheet and in other snow-covering areas.

2.8 Acknowledgements

W. Wang thanks Carolyn McClaskey, Andreas Peter Ahlstrøm, Konrad Steffen, Marie Dumont and the anonymous reviewer for their constructive feedbacks. The authors acknowledge the GC-Net team for providing and helping to interpret AWS measurements. CERES cloud and radiation data were obtained from the NASA Langley Research Center Atmospheric Science Data Center; MERRA radiation data were obtained from the Global Modeling and Assimilation Office and the Goddard Earth Sciences Data and Information Services Center. This work was funded by NASA Grants NNX12AF48A and NNX14AH55A.

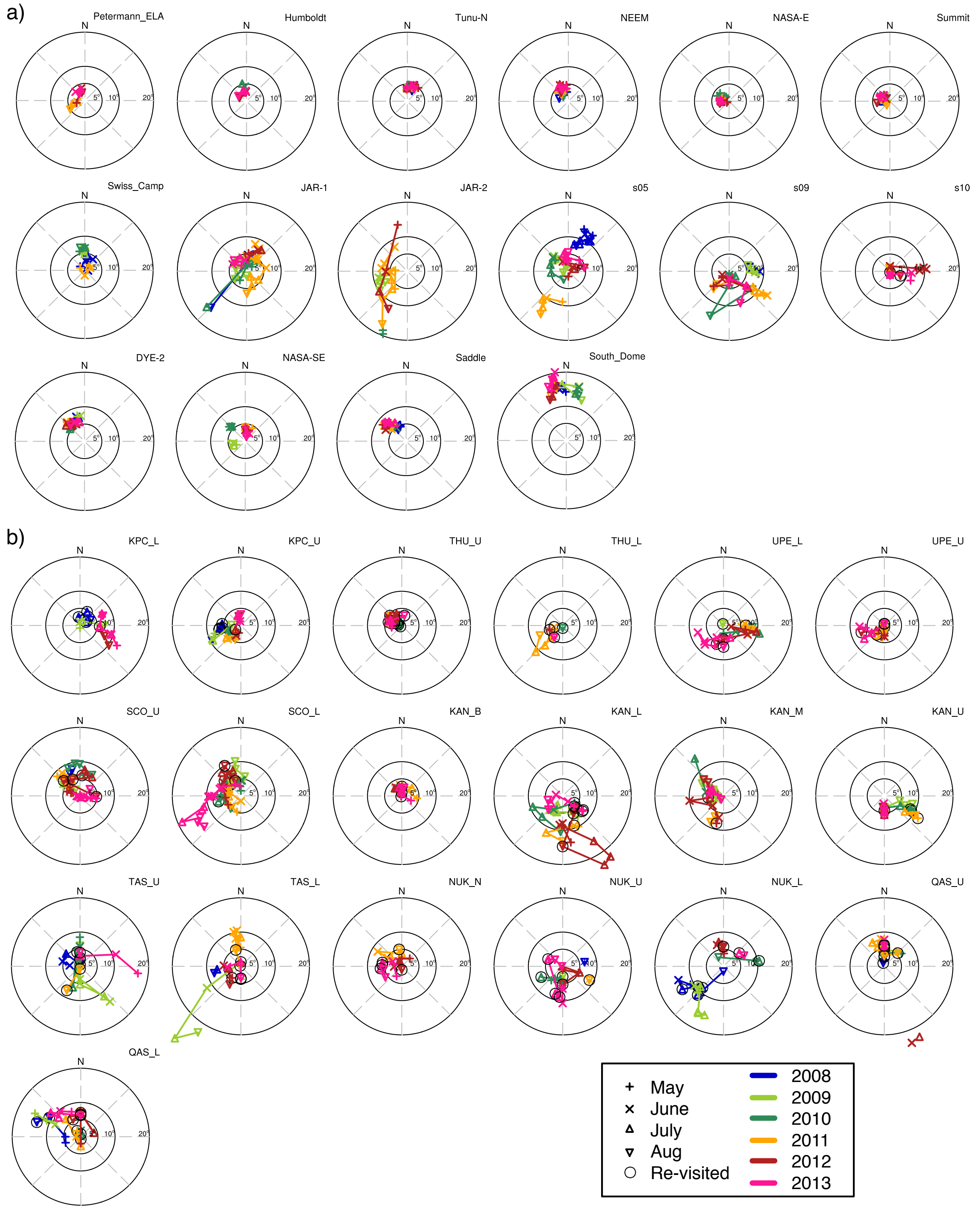

Figure 2.9: Station tilt angles (represented by the distance from the circle center) and tilt directions (0° points to the South) of a) GC-Net and K-transect; b) PROMICE. The markers are circled in black if the stations were re-visited in those months (no re-visiting record for GC-Net is found). There might be multiple tilt angles in one month. The panels of stations on each sub-figure are arranged in the order of latitude, from north to south.

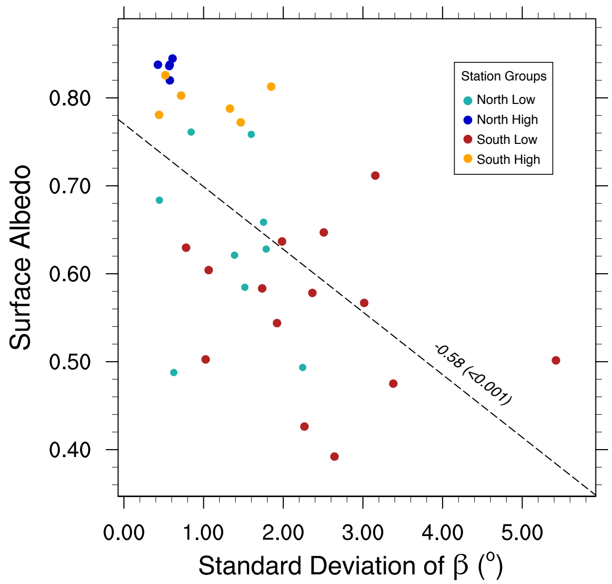

Figure 2.10: Correlation between surface albedo and the standard deviation of tilt angles (β). Numbers on dashed lines are the correlation coefficients. Numbers in the parentheses are the corresponding significant levels based on a two-tailed t test. Station KAN_B that is anchored into rock is not included.

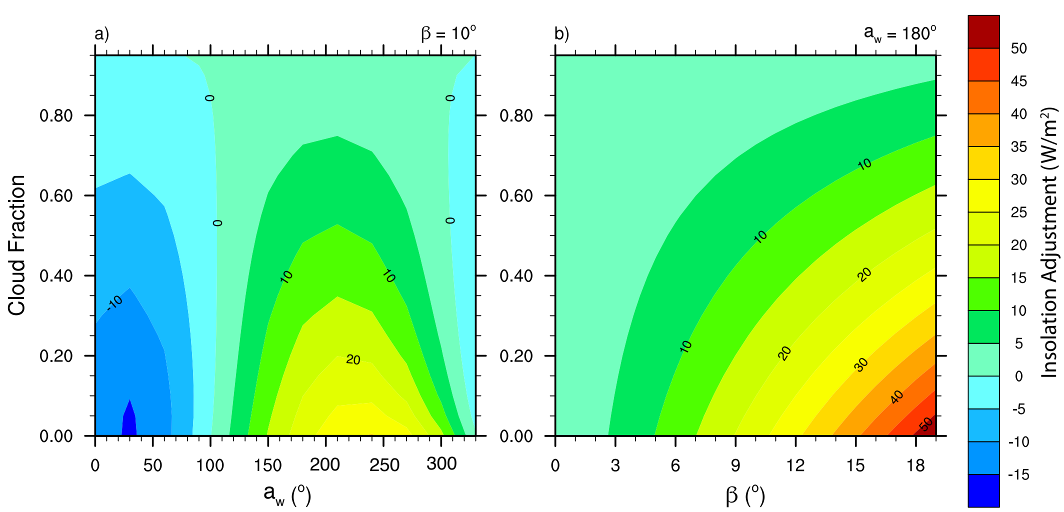

Figure 2.11: The effect of cloud fraction on daily average tilt correction of insolation changing with a) tilt direction (a_w) and b) tilt angle (β).

Chapter 3

Characteristics of cloud radiative effects and their major factors

3.1 Introduction

The impact of clouds on Greenland's surface melt is difficult to quantify due to the lack of *in situ* surface observations. To better quantify cloud radiative effects (CRE), we analyze and interpret multi-year radiation measurements from 30 automatic weather stations, and then assess the relative importance of cloud properties, surface albedo, and solar zenith angle (SZA). Sections 3.2 and 3.3 describe the datasets we use, including how we improve the data quality and estimate CRE. Section 3.4 evaluates the simulated clear-sky radiation at three human-attended stations in the Arctic. Section 3.5 and 3.6 analyze CRE spatial distribution and seasonal variability, and how they are determined by albedo, SZA and cloud properties. Section 3.7 examines the relationships between both albedo and SZA with CRE in two distinct radiative states on the hourly timescale. Lastly, in Section 3.8, we summarize our main findings and discuss the possible tendency of clouds to stabilize Greenland surface melt.

3.2 Data

By 2013, there were 39 long-term AWS operating in two separate networks in Greenland. The Greenland Climate Network (GC-Net) has 17 stations (*Steffen et al.*, 1996), 14 of which are in the accumulation zone (altitude $\geq$ 1800 m). The Programme for Monitoring of the Greenland Ice Sheet (PROMICE) has 22 stations (*van As and Fausto*, 2011), 21 of which are in the ablation zone (altitude < 1800 m). The PROMICE stations are usually arranged in pairs along a glacier with one upper station suffixed with U near the equilibrium line and one lower station suffixed with L deep in the ablation zone. These stations provide hourly measurements of surface radiation and meteorology.

We synchronize the two datasets (*Wang et al.*, 2016) and rigorously assess their data quality. We first remove impossible values using physical limits and the inter-variable dependency analysis in *Long and Shi* (2006). Then we remove data with large discrepancies between the measurements from the dual instruments at one station (GC-Net), and from the two stations within one pair (PROMICE). However, there are still serious problems in the AWS radiation measurements due to the lack of frequent maintenance, shading, and (heated) ventilation, including station tilt, low cosine response at large solar zenith angle (SZA), and riming and overheating of sensor domes (*Stroeve et al.*, 2001; *van den Broeke et al.*, 2004).

Station tilt, caused by uneven snow melt, snow compaction, and glacier dynamics, leads to considerable biases in shortwave (SW) measurements (*Bogren et al.*, 2016; *Wang et al.*, 2016). The maximum hourly absolute bias exceeds 200 W m^{-2} (*Wang et al.*, 2016). We use the Retrospective, Iterative, Geometry-Based (RIGB) tilt-correction method to adjust shortwave downwelling (SW↓) measurements (*Wang et al.*, 2016). RIGB relies on no additional instrumentation. Instead, it iteratively assesses the possible pairs of tilt angles and directions to find the best fit according to the clear-sky optical geometry on a tilted surface, and then uses direct/diffuse ratio estimated from cloud fraction to adjust the all-sky SW↓ measurements. However, RIGB requires sufficient solar insolation to work well, another reason for this study to focus on the melt season.

Insolation measurements significantly biased by the low cosine response issue are largely rejected by the first data quality check. However, the induced missing data at large SZA can lead to an overestimate of daily average insolation. To fill these missing values, we first assign zeros to the hours when the theoretical insolation is below zero. Next, we linearly interpolate the 1-hr gaps, and use spline interpolation to fill the gaps smaller than 12 hours. For the final daily average of insolation, only days with less than 1 missing hour are included. Considering the large seasonal variabilities of radiation, we keep only stations with at least one complete seasonal cycle.

Pyrgeometers used by PROMICE to measure longwave (LW) radiation can be heated by undesirable SW radiation without proper shading and ventilation. This problem cannot be resolved by measuring dome temperature because it is impossible to differentiate dome temperature increases caused by LW and by SW. The manufacturer, Kipp & Zonen, provides the maximum window heat offset under clear-sky and windless conditions, which is 25 W m^{-2} out of 1000 W m^{-2} SW↓ for CG3 pyrgeometers, and 6 W m^{-2} out of 1000 W m^{-2} SW↓ for CG4, an upgraded version. Although wind can serve as a natural ventilation, it is not consistent and sometimes not sufficient to negate the overheating. Therefore, we subtract the maximum offset, and potentially underestimate CRE on windy days. GC-Net stations do not measure LW radiation.

Riming on sensor domes occurs occasionally during summer in Greenland even in the dry environment at Summit (personal communication with Nathaniel B. Miller, University of Colorado). *Box et al.* (2004) only use AWS measurements of radiation and temperature when the wind speeds exceed 4 m/s to reduce the influence of riming. However, as mentioned above, natural ventilation may be insufficient to remove dome riming. Moreover, there are more gaps in wind speed than in radiation measurements. Since wind speed is more variable than radiation, it is harder to interpolate. *Miller et al.* (2015) mark the potential riming incidents when relative humidity (RH) with respect to ice exceeds 100%. On overcast days when humidity is high, temperature is normally high as well. This makes sensors less susceptible to riming (*Sedlar et al.*, 2011). Additionally, the cloud base temperature is usually close to the ambient temperature, resulting in a small bias in LW$\downarrow$ under overcast conditions (*Kipp & Zonen*, 2008). Therefore, removing all incidents with saturated water vapor content might lose a considerable portion of good data.

Instead of identifying riming incidents, we locate AWS radiation data biased by riming. In the Arctic, the LW$\downarrow$ radiation is not expected to exceed LW upwelling (LW$\uparrow$) radiation. When it does, the data is likely infected by riming (*van den Broeke et al.*, 2004). To allow for uncertainty, we remove LW$\downarrow$ that exceeds (LW$\uparrow$+5 W m^{-2}). Although rime could form on the down-looking pyrgeometers as well, gravity and the station shaking with wind make them less susceptible. As for SW measurements, riming can cause drastic albedo changes in a short amount of time because the SW$\uparrow$ is less affected than SW$\downarrow$ (*van den Broeke et al.*, 2004). To circumscribe the hourly change of albedo, we remove data when the second derivative of albedo is greater than 0.1. These methods likely do not eliminate all riming incidents though they significantly reduce rime-biased radiation measurements.

The remaining stations are shown in Fig. 3.1, among which 13 are from GC-Net and 17 are from PROMICE. The stations are divided into 6 groups based on their latitude and altitude: two groups in the accumulation zone (north and south), three groups in the ablation zone (north, middle and south), and one group on bare rocks with scattered snow cover (the bare rock group).

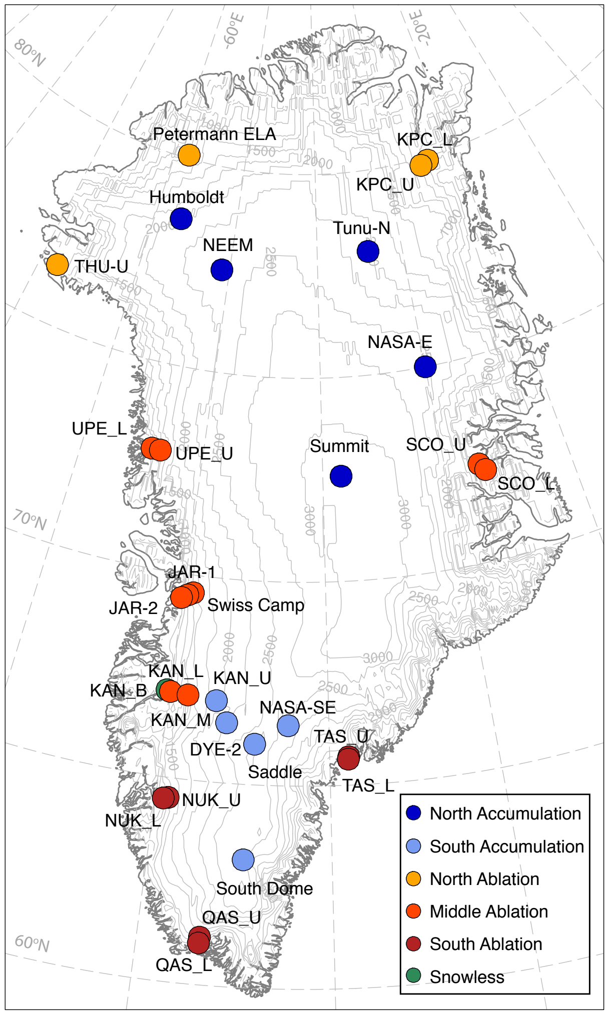

Figure 3.1: The automatic weather stations (AWS) used in this study, divided into 6 groups according to their latitude and altitude: north accumulation (dark blue), south accumulation (light blue), north ablation (yellow), middle ablation (orange), south ablation (red), and snowless (green).

GC-Net stations measure SW↑ and SW↓ components and net radiation, not LW components. The net radiation instrumental uncertainty is 5% to 50% (*Box and Steffen*, 2000). The errors can be large, especially when the instrument is not ventilated (*Box et al.*, 2004). We estimate the LW↑ from surface temperature using a constant snow emissivity of 0.985 (*Box et al.*, 2004; *Miller et al.*, 2015), and LW↓ as the residual of net radiation, SW radiation, and LW↑. After the aforementioned quality control for daily and seasonal averages, only four GC-Net stations remain: Tunu-N, Humboldt, Summit and NASA-SE.

3.3 Method

We define CRE as the instantaneous effect of a cloud on the surface energy budget compared to clear skies (*Intrieri et al.*, 2002). Therefore, it is estimated as the total radiation at surface under all-sky conditions minus that under clear skies, assuming unchanged meteorological conditions. Although cloudy days are often characterized by higher humidity and temperature than clear days, the difference is not significant according to radiosonde data at both Summit, Greenland and Barrow, Alaska, U.S.A. We also acknowledge that snow albedo increases with cloudiness (e.g., *Gardner and Sharp* (2010)) because cloud absorption is high at near-infrared where albedo is low, making the broadband albedo higher (*Miller et al.*, 2015). Nevertheless, these "instantaneous CRE" assumptions are reasonable and practical for studying clouds' contributions to surface energy budget (*Shupe and Intrieri*, 2004). Accordingly, we calculate CRE as:

$$CRE_{SW} = (SW\downarrow_{all-sky} - SW\downarrow_{clr-sky}) \cdot (1 - albedo) \tag{3.1}$$

$$CRE_{LW} = LW\downarrow_{all-sky} - LW\downarrow_{clr-sky} \tag{3.2}$$

$$CRE_{net} = CRE_{SW} + CRE_{LW} \tag{3.3}$$

Clear-sky radiative fluxes are simulated by the Column Radiation Model (CRM), the stand-alone version of the Community Atmosphere Model version 3 (CAM3) radiation model updated from *Zender* (1999), driven by atmospheric profiles and surface conditions. We use atmospheric temperature and humidity profiles from the Atmospheric Infrared Sounder (AIRS) (*AIRS Science Team/Joao Texeira*, 2013), which are 1-deg (~50 km in Greenland) data with one ascending orbit and one descending orbit per day. At the surface, we use AWS-measured hourly temperature and 24-hr running average albedo. Values from a sub-Arctic standard atmosphere are used for parameters with little variability, such as Ozone, CO_2, and aerosol optical depth.

3.4 Evaluation of clear-sky simulations

We evaluate CRM settings and input AIRS atmospheric profiles by comparing simulated radiative fluxes with *in situ* measurements under clear-sky conditions at three human-attended stations: the Baseline Surface Radiation Network (BSRN) station at Alert, Lincoln Sea, the Atmospheric Radiation Measurement (ARM) station at Barrow, Alaska, U.S.A., and the Global Monitoring Division (GMD) NOAA station at Summit, Greenland. Hourly all-sky radiation (for comparison) and basic meteorological measurements (for model input) are provided by all three stations for at least two years. We detect clear skies using the *Long and Ackerman* (2000) identification methods with re-evaluated parameters from local data.

We perform the same data quality check on these stations as on AWS. We find solar noon shifts at Alert and Summit, most likely caused by station tilt. We adjust the SW↓ at Alert using the RIGB tilt correction method (*Wang et al.*, 2016). At Summit, the nearly isotropic SW↑ radiation shifts more than the anisotropic SW↓, which violates RIGB's assumptions. Therefore, we estimate SW↑ radiation using the daily average albedo. Riming effects are largely removed by the "normalized total shortwave magnitude test" and "normalized diffuse ratio variability test" used in the clear-sky detection (*Long and Ackerman*, 2000), except at Summit, where diffuse radiation is not measured. We do not include LW↑ in the evaluation at Alert. Its near-surface air temperature is measured at a greater height than the LW↓ instrument. The simulated LW↑ using this temperature as the surface temperature proxy does not present a good correlation with observations.

Table 3.1: Daily average RMSD and the difference between simulated and measured radiative fluxes under clear-sky conditions (W m^{-2}).

		SW↓	SW↑	LW↓	LW↑	net SW	net LW	Total
RMSD	Alert	9	1	10		9		
	Barrow	6	11	10	1	6	10	8
	Summit	13	10	26	9	6	34	40
Diff.	Alert	-4	0	-2		-5		
	Barrow	4	-5	-10	0	4	-9	-6
	Summit	-10	-5	-26	8	-4	-34	-40

We estimate the daily average (root-mean-square difference) RMSD and differences between the simulated and measured radiation under clear-sky conditions (Table 3.1). During melt season, our simulation underestimates net SW (downwelling minus upwelling) by 5 W m^{-2} and 4 W m^{-2} at Alert and Summit, respectively, and overestimates by 4 W m^{-2} at Barrow. One model uncertainty in SW simulation comes from that CRM is a 2-stream radiative transfer model that does not include the effects of Earth's curvature on insolation at large SZA. The Chapman function shows that neglecting Earth's curvature underestimates SW↓ by about 7 W m^{-2} at SZA = 80°, the latitude of Summit (*Chapman*, 1931; *Wilkes*, 1954). Nevertheless, RMSD of net SW at all three stations do not exceed 10 W m^{-2}.

While most LW RMSD are less than 10 W m^{-2}, the negative bias in LW↓ is 26 W m^{-2} at Summit, causing the total RMSD to be 40 W m^{-2}. Unlike the CRM shortwave simulation whose precision is mainly determined by the model physics, the LW simulation is very sensitive to the input temperature and humidity profiles. To understand this large LW↓ discrepancy, we compared the AIRS atmospheric profiles with radiosonde measurements at Summit (data provided by the Integrated Characterization of Energy, Clouds, Atmospheric State and Precipitation at Summit, ICECAPS) and at the ARM station at Barrow (Table 3.2). Profile biases account for up to 6 W m^{-2} of RMSD in the LW↓ simulation at both stations, which cannot explain the large RMSD at Summit and yet the small RMSD at Barrow. Moreover, simulation using Summit radiosonde profiles instead of AIRS profiles also underestimates LW↓ enormously (RMSD = 22 W m^{-2} and difference = -21 W m^{-2}). LW↓ at

Table 3.2: RMSD and average difference of temperature profile and column water (CWP) path and their impacts on LW↓.

	Temp. RMSD	ΔLW↓	Temp. avg. diff.	ΔLW↓
Summit	0.61 K	1 W m^{-2}	-0.49 K	-1 W m^{-2}
Barrow	0.42 K	1 W m^{-2}	-0.08 K	0 W m^{-2}
	CWP RMSD	ΔLW↓	CWP avg. diff.	ΔLW↓
Summit	0.62 kg m^{-2} (27%)	6 W m^{-2}	-0.03 kg m^{-2} (1%)	0.2 W m^{-2}
Barrow	2.19 kg m^{-2} (17%)	6 W m^{-2}	-0.75 kg m^{-2} (6%)	1.5 W m^{-2}

Summit is measured by a Precision Infrared Radiometer (PIR), which is ventilated though not shaded (personal communication with Dr. David Longenecker, NOAA). We speculate that sensor-dome heating by SW radiation causes this artificial increase in LW↓ measurements. Therefore, biases at Barrow best represent the clear-sky simulation uncertainty in this study. The RMSD of total radiation under clear-sky conditions is 8 W m^{-2}, and the average difference is -6 W m^{-2}.

3.5 CRE spatial distribution

AWS in Greenland cover a large area with various topographies, resulting in considerable differences in cloud properties, solar and surface conditions. In this section, we estimate CRE at these stations on the semi-monthly timescale, and examine how the spatial variabilities of albedo, SZA, and cloud properties affect the competition of clouds' longwave greenhouse effect and shortwave shading effect. A case study along the Kangerlussuaq transect (K-transect) using daily observations provides greater insights into the effects of altitude-related changes of cloud properties and albedo on CRE.

During melt season, the longwave greenhouse effect is larger than the shortwave shading effect in most of Greenland, resulting in a net warming effect; on the other hand, the shortwave effect with a larger variability determines the overall spatial distribution (Fig. 3.2). We use 20-day running average (i.e., semi-monthly timescale) to reduce the synoptic influence

(*Intrieri et al.*, 2002) on spatial distributions. We also further divide the three ablation zone groups (northern, middle, and southern) into upper (U) and lower (L) sub-groups, to better compare CRE under different geographical conditions. The average LW CRE is ~50 W m^{-2} in all groups (red boxes in Fig. 3.2 and Table 3.3). It slightly increases from north to south and from the upper to the lower groups. The range between the largest and the smallest is 12 W m^{-2}. Larger variability in the southern groups mostly represents a larger seasonal cycle. SW CRE is negative in all groups (blue boxes in Fig. 3.2). It also gets more intense from north to south and from high to low altitude, with a more discernible inter-group difference. It ranges from the weakest in the accumulation zone (group average of -6±3 W m^{-2} for the north and -5±3 W m^{-2} for the south) to the strongest at the southern lower stations (-51±22 W m^{-2}). We do not include KAN_B in Fig. 3.2. Although KAN_B is located in the middle ablation zone, its dark albedo of bare rocks make the SW CRE less than the lower-station mean in the south ablation zone. To combine the SW and LW, net CREs are positive in all groups during almost the entire melt season except at the lower stations in the south (green boxes in Fig. 3.2). The largest warming effects are 41±14 W m^{-2} and 41±8 W m^{-2} for northern and southern stations in the accumulation zone, respectively, and the smallest is 5±18 W m^{-2} for the lower southern stations in the ablation zone. However, the spatial distribution of net CRE follows that of SW CRE: the largest net CRE is in the accumulation zone where SW CRE is weakest, instead of in the ablation zone, where LW CRE is strongest. Within both upper and lower groups in the ablation zone, net CRE decreases, instead of increases, from north to south.

The large spatial variability of SW CRE is mainly caused by albedo. SW CRE components include the solar insolation difference under all-sky and clear-sky conditions (shortwave downwelling CRE, SW↓ CRE hereafter), and albedo (Eq. 3.1). The former is dominated by SZA and cloud properties. However, neither of their contributions to CRE has a larger spatial variability than albedo's. Clear-sky insolation, the maximum insolation that can be potentially affected by clouds, is controlled by SZA. Over Greenland, the inter-station SZA

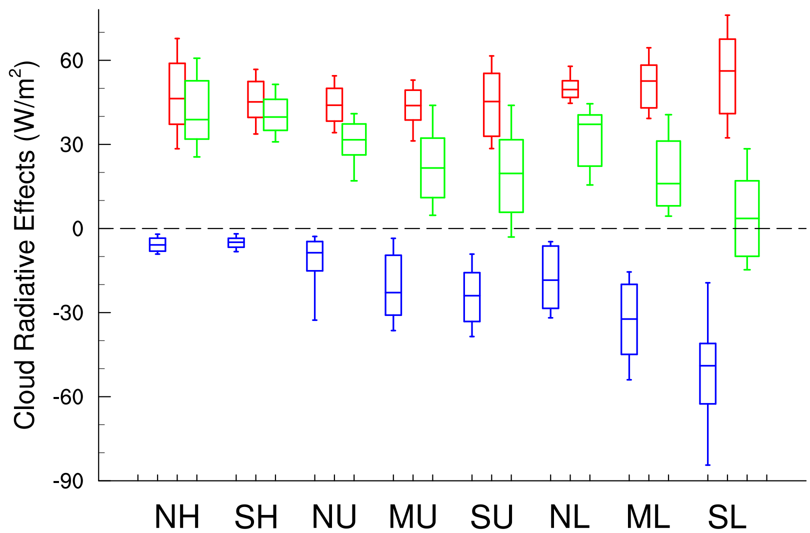

Figure 3.2: Statistics of 20-day running average SW (blue), LW (red), and net (green) cloud radiative effects in different geographical groups: north and south accumulation zones (NH and SH), upper stations in north, middle, and south ablation zones (NU, MU, and SU), and lower stations in north, middle, and south ablation zones (NL, ML, and SL). Whiskers show lower decile and upper decile, box lines show upper quartile, median, and lower quartile.

difference is small due to the fact that the smaller noon SZA in the north is compensated by the longer daylight duration. The insolation increase from north to south is only $\sim$20 W m^{-2} across 20° in latitude (Fig. 3.3). The range of all-sky insolation between the largest and the smallest is 76 W m^{-2}, which mostly arises from cloud properties. The all-sky insolation peaks in the accumulation zone and decreases with altitude and also from north to south in the ablation zone, indicating higher cloud fraction and/or larger cloud optical depth at lower altitudes and in the south, where are warmer and wetter. Albedo decreases from $\sim$0.8 in the accumulation zone to $\sim$0.4 in the lower ablation zone, becoming a powerful multiplicand in determining SW CRE. Albedo on snow-covered surfaces is inversely related to temperature (*Flanner and Zender*, 2006). It decreases as snow grains enlarge and snow melts due to temperature increases from high to low altitudes and from north to south. The correlation coefficient between the station-average albedo and SW CRE is extremely high (r = 0.95 and $p << 0.01$), even if the dependency of albedo on cloudiness is considered. This strong

Table 3.3: Average SW, LW, and net CREs (W m^{-2}) with standard deviation in different geographical groups (divided in the same way as in Fig. 3.2).

	SW	LW	net
NH	-6±3	47±15	41±14
SH	-5±3	46±9	41±8
NU	-13±11	44±7	31±9
MU	-21±12	43±9	22±14
SU	-24±11	45±12	20±17
NL	-18±11	51±5	32±11
ML	-33±15	51±11	20±14
SL	-51±22	55±16	5±18

correlation indicates that albedo is the primary cause for the large spatial variability of SW CRE.

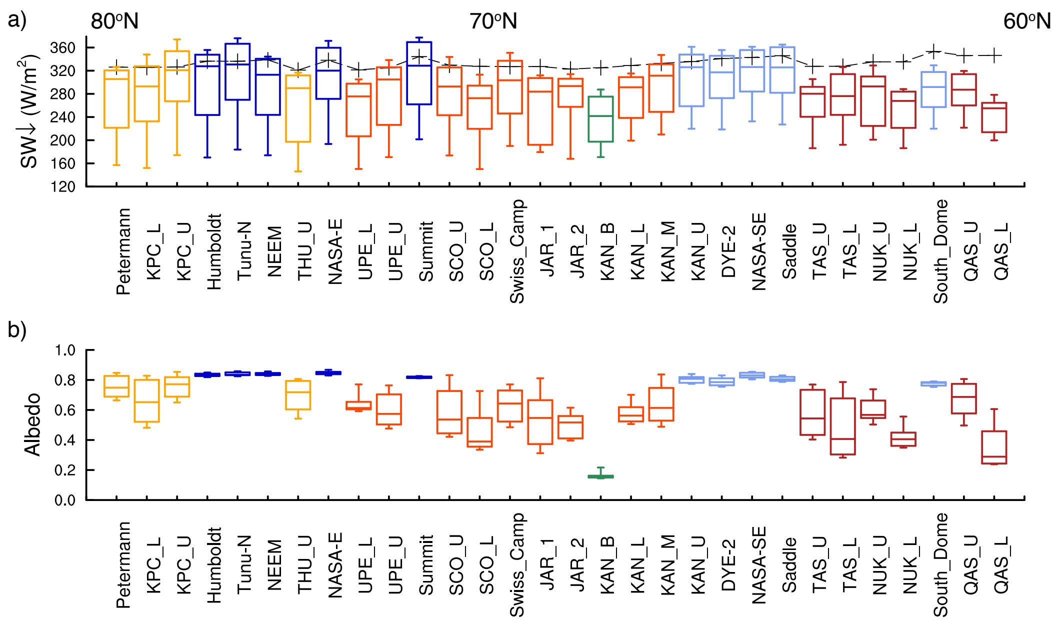

Figure 3.3: Statistics of 20-day running average of a) all-sky SW↓ and b) albedo at each station. The black line in a) represents the clear-sky SW↓. The group colors are the same as in Fig. 3.1. Whiskers show lower decile and upper decile, box lines show upper quartile, median, and lower quartile.

Spatial variability of LW CRE is smaller than SW's, which might be associated with their different sensitivities to cloud properties and the environment. We assume LW↑ does not change under measured all-sky conditions and clear-skies. Therefore, LW CRE equals

LW$\downarrow$ CRE (Eq. 3.2). All-sky LW$\downarrow$ (boxes in Fig. 3.4a) and clear-sky LW$\downarrow$ (the black line in Fig. 3.4a) are intimately related to the near-surface air temperature through the Stefan-Boltzmann law (Fig. 3.4b). Due to the mountainous topography of Greenland, air temperature at each station is controlled largely by altitude rather than latitude (Fig. 3.4c). Therefore, LW$\downarrow$ is high at the low-altitude stations, and low at the high-altitude stations. The long tail of Humboldt (one GC-Net station) probably results from there being only one melt season of data at this station (Fig. 3.4a). At other stations, all-sky LW$\downarrow$ are all higher than clear-sky LW$\downarrow$. The difference between the two (i.e., LW CRE) changes mildly from station to station. This relatively small spatial variability of LW CRE could result from saturation in LW response to cloud thickness increases. According to experiments at Summit, Greenland, the longwave greenhouse effect becomes less sensitive to cloud liquid water content when the clouds are thicker than $40\,\mathrm{g\,m^{-2}}$ (*Bennartz et al.*, 2013). In southern and low-altitude Greenland, clouds might already be thick enough for LW CRE to reach its maximum. Another explanation is that SW CRE and LW CRE respond to cloud property changes with different sensitivities. For example, SW CRE is directly affected by cloud phase, while LW CRE is more sensitive to cloud height (*Shupe and Intrieri*, 2004). Moreover, high temperature and excessive water vapor under clouds reduce LW$\downarrow$ difference with and without cloud presence (*Cox et al.*, 2015), leading to a smaller LW CRE. In Greenland, it is warmer and wetter as well as more cloudy from north to south and from high to low altitudes, making LW CRE more spatially unified.

The four AWSs (KAN_B, KAN_L, KAN_M, and KAN_U) along the Kangerlussuaq transect in southwest Greenland provide a unique opportunity to elucidate the role of altitude-related changes of cloud properties and albedo to CRE. These four stations, spreading from bare rocks into the accumulation zone, occupy nearly the same latitude, and thus the same solar illumination. The average albedo decreases from above 0.8 at the highest station, KAN_U, $\sim$50 km above the equilibrium line in the accumulation zone, to below 0.2 at the lowest station, KAN_B, closest to the ocean and mounted on bare rocks (Fig. 3.5a). Temper-

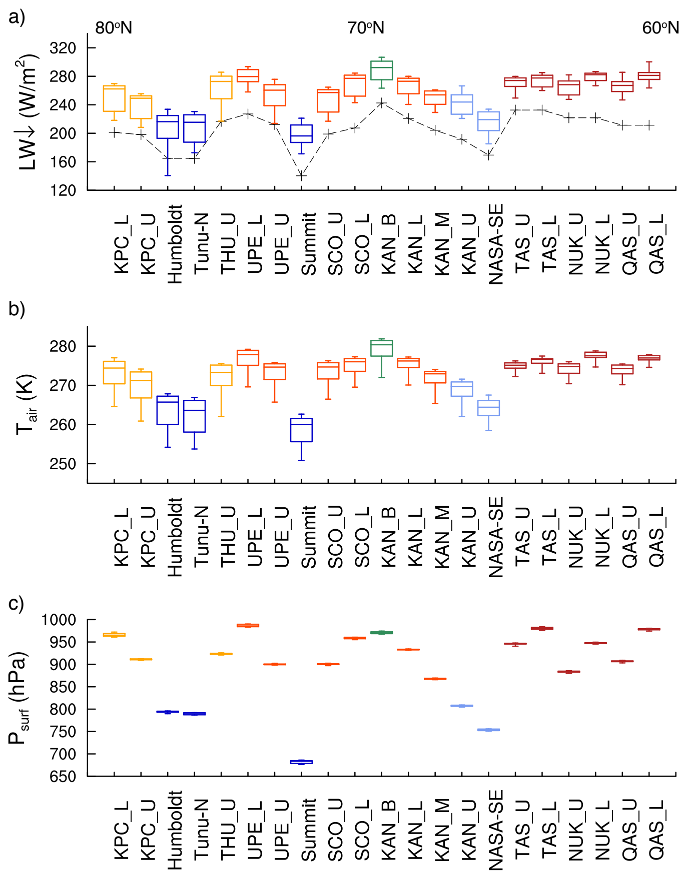

Figure 3.4: Similar to Fig. 3.3 but for a) all-sky LW↓, b) near-surface air temperature, and c) surface pressure. The black line in a) represents clear-sky LW↓.

ature and humidity increase from KAN_U to KAN_B, suggesting a possibly higher cloudiness at lower altitude (Fig. 3.5b and c). Accordingly, SW↓ CRE intensifies while LW CRE stays almost constant as altitude decreases, resulting in a positive net CRE at high altitude and a negative net CRE at low altitude (Fig. 3.5d, e, and f).

On the daily timescale, both SW↓ CRE and LW CRE show discernible temporal variability. The similarity among stations and the inverse correlation between SW↓ CRE and LW CRE suggest that the temporal cloud property changes are caused by large-scale systems. These cloud properties exert considerable influences on both SW and LW, although the daily variability is still larger in SW↓ CRE than in LW CRE. On the other hand, the spatial variabilities among stations are only discernible in SW↓ CRE. The inter-station cloud property differences affect SW CRE substantially but not LW CRE.

In summary, although LW CRE is currently larger than SW CRE in most of Greenland, the overall spatial distribution is controlled by SW CRE, and in turn by albedo. The correlation coefficient between station-average albedo and net CRE is 0.93 ($p << 0.01$). Where the surface is bright with high albedo, clouds warm surface and positively contribute to surface melt; where the surface is darker with lower albedo, clouds warm surface less or even cool the surface.

3.6 CRE seasonal variability

There is a dispute in preview studies on CRE seasonal cycles in the Arctic. CRE first decreases from May to July and then increases afterwards, observed during an in-situ campaign (*Intrieri et al.*, 2002) and by remote sensing (*Kay and L'Ecuyer*, 2013) in the Arctic ocean. On the other hand, CRE increases monotonically throughout the melt season observed at a mobile station at Summit, Greenland (*Miller et al.*, 2015). Due to the differences in in-

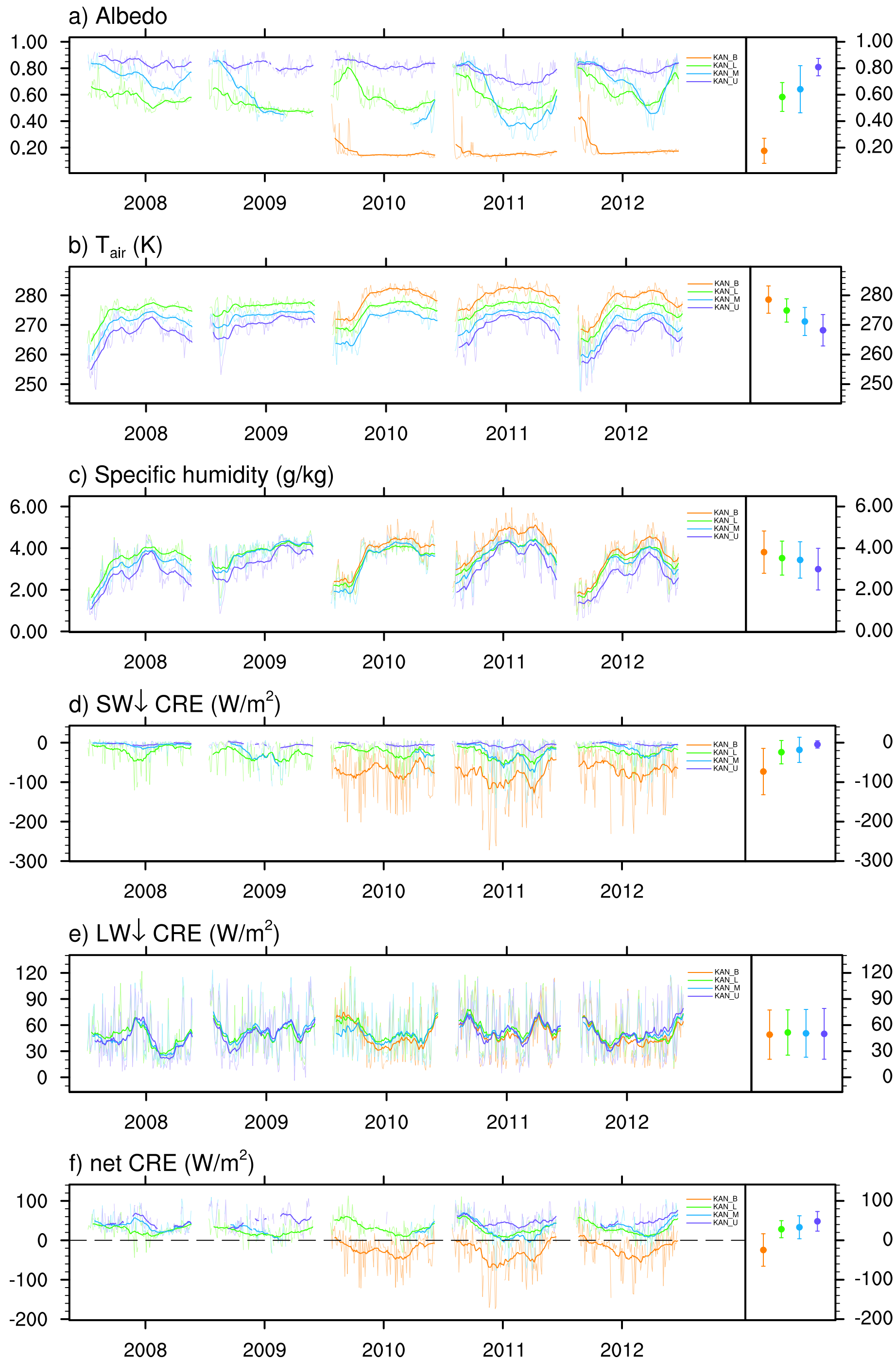

Figure 3.5: Daily average (thin lines), 20-day running average (thick lines), and average with daily standard deviation (dots and error bars in side panels) of a) albedo, b) near-surface air temperature, c) specific humidity, d) SW↓ CRE, e) LW↓ CRE, and f) net CRE at four stations KAN_U (purple), KAN_M (blue), KAN_L (green), KAN_B (orange) along the Kangerlussuaq transect. The black dashed line in f) represents 0 W m^{-2} net CRE.

strumentation, time, and place, reasons behind this dispute are unknown. Cloud properties, albedo, and SZA change greatly during the course of melt season. In this section, we investigate how they shape CRE seasonal cycles differently in different geographical regions, which reconciles the dispute.

Net CRE seasonal cycles are different in the ablation zone and in the accumulation zone. In the ablation zone, clouds warm surface more at the beginning and the end of the melt season and less in the middle; in the accumulation zone, clouds warm surface more from the beginning to the end of melt season (Fig. 3.6). In the ablation zone, Net CRE shares a very similar seasonal pattern from north to south with larger amplitudes towards south (Fig. 3.6a). These cycles are predominantly determined by SW CRE seasonal variability (Fig. 3.6b). In the accumulation zone, net CRE increases almost linearly from May to August in the north. In the south, it slightly decreases in May and rises afterwards (Fig. 3.6a). Due to the minor seasonal variability of SW CRE in this area, net CRE seasonal cycle is dominated by LW CRE (Fig. 3.6c). The seasonal cycle amplitude of northern accumulation zone is similar to that of the ablation zone. In the south, the amplitude is much smaller in the accumulation zone than in the ablation zone. The different seasonal cycles over Greenland, which has mountainous terrain, reconcile controversies in previous studies. At Summit, Greenland, our net CRE seasonal cycle is consistent with *Miller et al.* (2015)'s: net CRE increases from May to July and slightly declines in August. Our seasonal cycles in the ablation zone qualitatively agree with the findings in the Arctic Ocean: over sea ice, clouds warm surface at the beginning and the end of the melt season, and briefly cool (warm less) surface in the middle. (*Intrieri et al.*, 2002; *Shupe and Intrieri*, 2004; *Kay and L'Ecuyer*, 2013).

The seasonal trends of LW CRE also vary in different regions, possibly caused by the spatial variability of under-cloud temperature and humidity. In the southern and middle ablation zones, LW CRE becomes weaker from May to July and stronger afterwards; in the northern ablation zone and the southern accumulation zone, it fluctuates mildly from

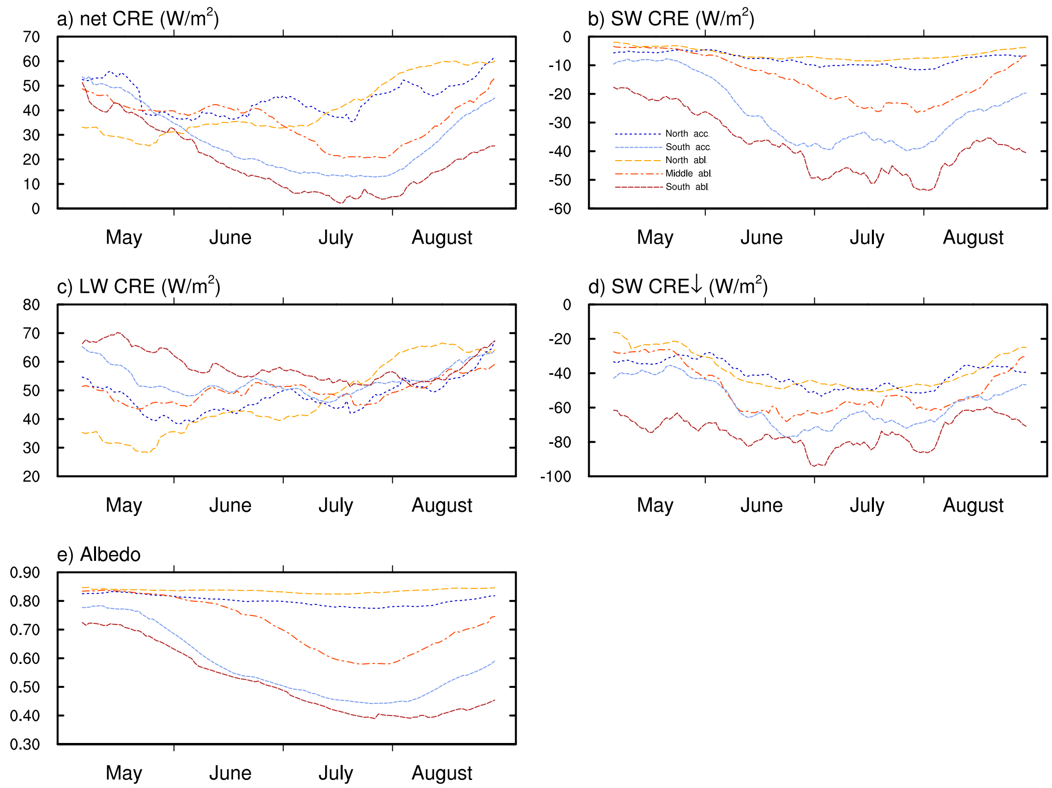

Figure 3.6: Seasonal cycles of a) net CRE, b) SW CRE, c) LW CRE, d) SW↓ CRE, and e) albedo in different groups. Group colors same as Fig. 3.1.

May to July and becomes considerably stronger from late July to August; in the northern accumulation zone, it intensifies directly from May to early-August and starts to decline at the end of August (Fig. 3.6c). The seasonal trend in the northern accumulation zone is in accordance with those of cloud fraction and liquid water content at Summit reported in *Miller et al.* (2015), and therefore is possibly caused by cloud property changes. In the rest of Greenland, LW CRE responds to clouds in an almost opposite manner to SW↓ CRE throughout the season (Fig. 3.6d). These contrasting seasonal trends also exist in the comparison of LW CRE at Summit, Greenland and Barrow, Alaska, U.S.A. (Fig. 3.7). The data at Summit here is from the human-attended station (*Miller et al.*, 2015), which shows a consistent seasonal trend as AWS Summit. The seasonal trend at Barrow, which is adjacent to the ocean and only covered by scattered snow in summer, is closer to that in the southern ablation zone. Further studies into cloud and atmospheric profile observations are needed to explain this divergence.

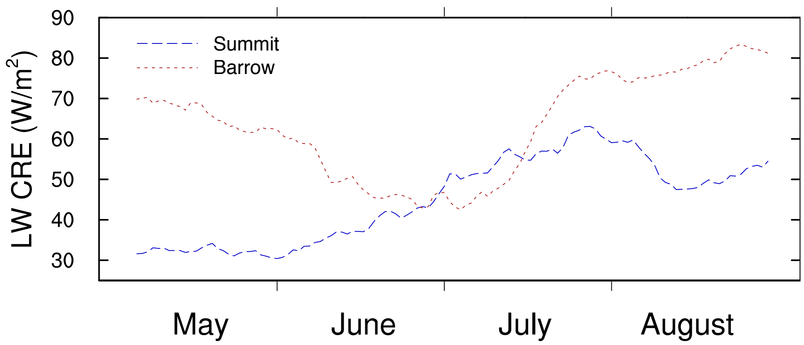

Figure 3.7: Seasonal cycles of LW CRE at Summit, Greenland and Barrow, Alaska, U.S.A.

Though with various amplitudes, the seasonal SW CRE shares the same trend in different regions: SW CRE becomes stronger from May to July and weaker afterwards (Fig. 3.6b), which is mainly controlled by albedo (Fig. 3.6e). The correlation coefficients between albedo and SW CRE are greater than 0.90 in all groups in the ablation zone ($p << 0.01$). In the accumulation zone, the correlations are weaker ($r = 0.74$ for the north and 0.89 for the south) yet also significant ($p << 0.01$). $\cos(SZA)$ is largest in June instead of in July. Therefore, SZA only shows a weak negative correlation with SW CRE in the northern accumulation zone ($r = -0.35$; $p < 0.01$) where albedo seasonal variability is minimum.

During melt season, in the accumulation zone, where albedo seasonal variability is limited, net CRE is determined by LW CRE. Net CRE increases during most of the season and flats out at the end, which is possibly associated with the seasonal cycles of cloud fraction and liquid water content. In the ablation zone, net CRE is determined by SW CRE and in turn by albedo. When albedo is higher (e.g., in May), clouds warm surface more. The triggered snow metamorphism and snow melt reduce albedo. When albedo is lower (e.g., in July), clouds warm surface less and tend to forestall snow melt.

3.7 Two states of hourly CRE

In the central Arctic in winter, the weather is either near clear or overcast most of the time, rarely partially cloudy (*Morrison et al.*, 2011; *Cesana et al.*, 2012). *Morrison et al.* (2011) characterizes this phenomenon as "two quasi-steady radiative states". In Greenland during melt season, we find a similar bimodal radiative distribution. In this section, we compare the two radiative states in Greenland and in the central Arctic, and re-examine the roles of albedo and SZA in these two radiative states.

Similar to the central Arctic, there exist two semi-distinct radiative states in Greenland: the radiatively clear and cloudy states. However, the peak position and the duration of each state are different in these two regions. In the central arctic in the clear state, net LW (downwelling minus upwelling) is near -40 W m^{-2} with clear sky or thin clouds; in the cloudy state, net LW is near 0 W m^{-2}, dominated by opaque, mixed-phase clouds (*Morrison et al.*, 2011). In Greenland, at all PROMICE stations except KAN_B (which is on bare rocks) net LW shows a bimodal distribution (Fig. 3.8a) peaking at ~-70 W m^{-2} (the clear state) and at ~0 W m^{-2} (the cloudy state). The clear state is slightly more common than the cloudy state at most stations. There are no significant changes in the positions or heights of the peaks in different months during melt season. At GC-Net stations, data show no bimodal distribution of net LW (Fig. 3.8b). Possibly, these two radiative states do not exist in the high accumulation zone, even though they do exist at KAN_U, 1840 m a.s.l. and 50 km into the accumulation zone. However, the long tail of the net LW distribution at GC-Net is more likely a symptom of poor data quality. There are no LW measurements at GC-Net (cf. Sec. 3.2), and we compute LW radiation as the residual of net and SW radiation. Therefore, the LW radiation incorporates all the measurement biases and might not be qualified for short-timescale analysis such as the hourly. In the central Arctic in winter the duration of either radiative state is up to 10–14 days and transitions are likely due to the large-scale advection (*Morrison et al.*, 2011). In Greenland in summer, the state duration is only a few

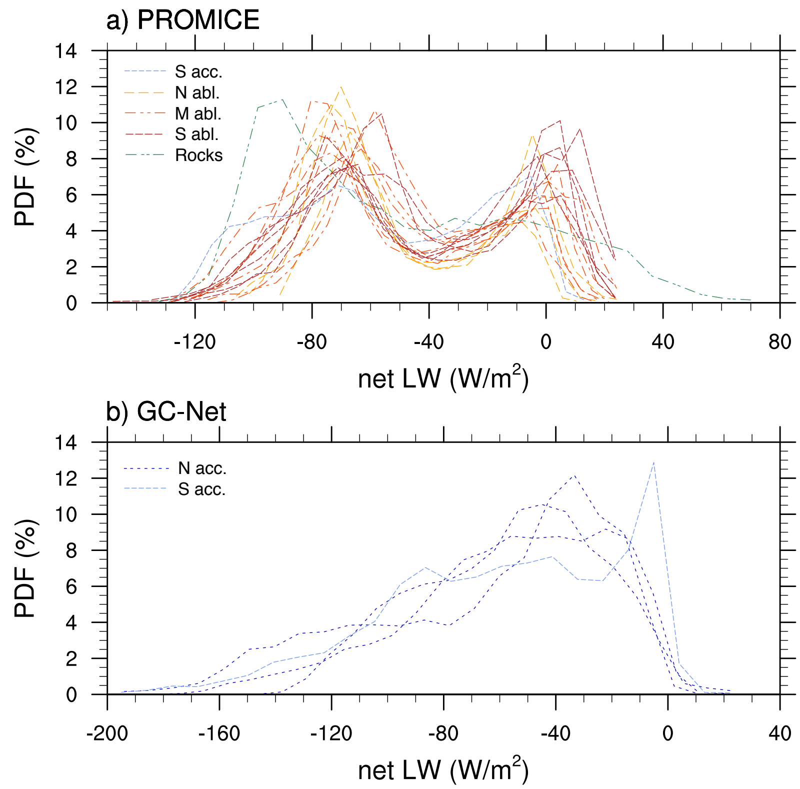

Figure 3.8: Probability density function of hourly net LW at a) PROMICE stations and b) GC-Net stations. The colors of station groups same as in Fig. 3.1.

hours and the cloudy-state peak shrinks as the average period gets longer (Fig. 3.9). In a 24-hour average, the cloudy-state peak completely disappears. This suggests that opaque clouds in Greenland summers persist for less than one day on average.

The combination of SZA and albedo strongly correlates with CRE in the cloudy state; correlation is weak in the clear state. SZA exerts a greater influence on the hourly timescale than on the longer timescales. Moreover, snow albedo and SZA are not independent— albedo usually increases with SZA (*Wang and Zender*, 2010b). Therefore, when we consider their relationship with CRE on the hourly timescale, we use the combination of SZA and albedo (SZA-albedo hereafter), cos(SZA) $\cdot$ (1 $-$ albedo) (*Sedlar et al.*, 2011). This combination accords with the clear-sky surface absorption of solar radiation, and correlates negatively with CRE. When sunlight is abundant, i.e., large $\cos(SZA)$, and the surface is dark, a given cloud scatters more solar radiation that can potentially be absorbed by the surface than with

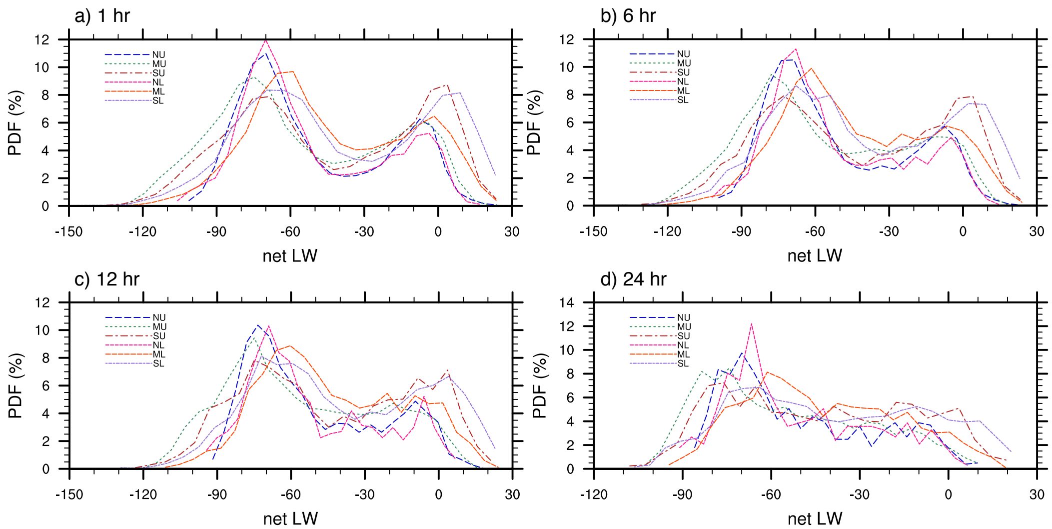

Figure 3.9: Probability density function of net LW averaged over a) 1 hr, b) 6 hr, c) 12 hr, and d) 24 hr at PROMICE stations at upper and lower stations in the north, middle, and south ablation zones.

faint sunlight and bright surface conditions, and therefore causes stronger (more negative) SW CRE. The joint probability density function shows two types of relationships between CRE and SZA-albedo: in one, CRE stays constant at ∼20 W m^{-2} while SZA-albedo changes; in the other CRE decreases almost linearly as SZA-albedo increases (Fig. 3.10). Using -35 W m^{-2} net LW as the threshold to separate clear and cloudy states, these two types of relationships between CRE and SZA-albedo correspond exactly with the two radiative states (Fig. 3.11). In the clear state (which is 58% of the time), CRE almost does not change with SZA-albedo. There is a weak correlation between the two ($r = -0.19$, $p << 0.01$). In the cloudy state (42% of the time), CRE decreases as SZA-albedo increases. The correlation is strong ($r = -0.85$, $p << 0.01$). This high correlation between SZA-albedo and CRE might also result from the saturation in LW CRE response to cloud thickness increases. LW CRE centers at 89 W m^{-2} with little variability (standard deviation = 22 W m^{-2}) in this state. On the other hand, SW CRE is substantially modulated by SZA and albedo (standard deviation = 93 W m^{-2}). In the clear state, CRE is more sensitive to cloud property changes, and the small CRE due to almost clear skies limits the modulating powers of SZA and albedo. To consider the influences of SZA and albedo separately, SZA shows a slightly stronger correlation with CRE ($r = -0.59$ for SZA and $r = 0.50$ for albedo in the cloudy state). Nevertheless, the combination of SZA and albedo has the highest correlation.

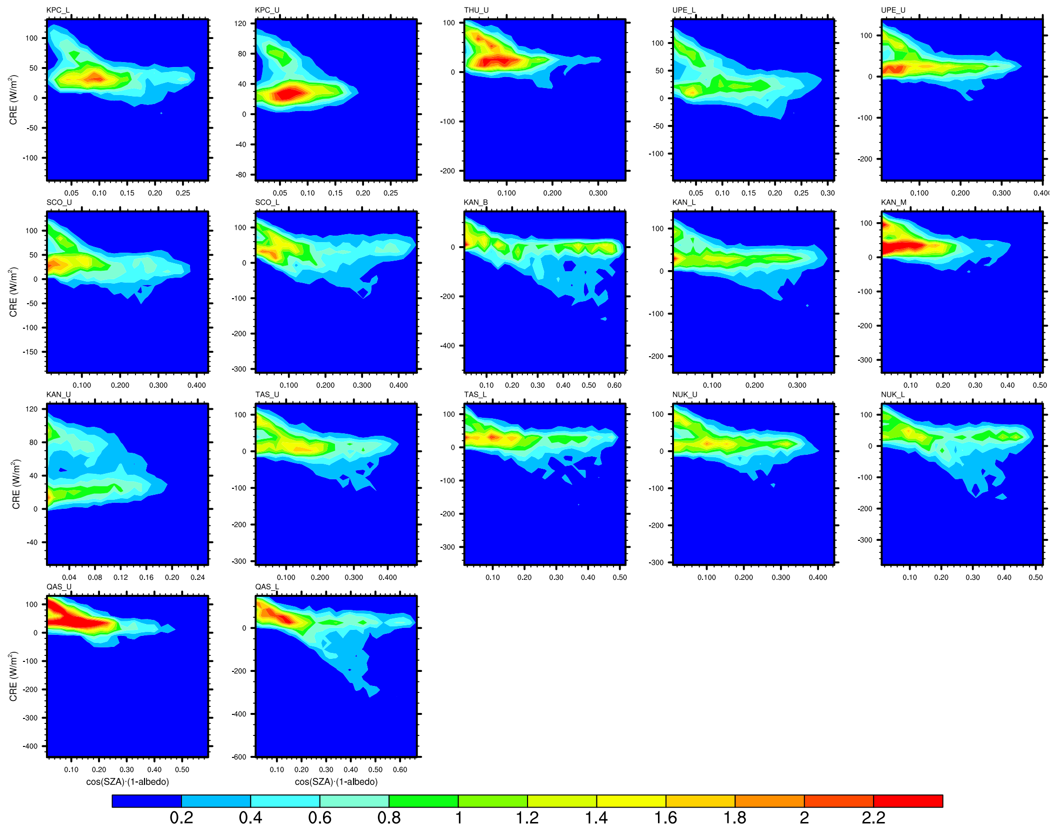

Figure 3.10: Joint probability density function of combined SZA and albedo with CRE at each PROMICE station.

In summary, the two semi-distinct radiative states suggest that the weather in Greenland usually alternates between hours of nearly clear skies and hours of opaque clouds. When it is nearly clear, CRE is small with little variation, 23±27 W m^{-2}, and almost does not change with SZA and albedo. When it is cloudy, CRE changes from over 100 W m^{-2} to less than -150 W m^{-2}, largely determined by SZA and albedo. Therefore, the two non-cloud factors, SZA and albedo, dominate CRE variability on the hourly timescale.

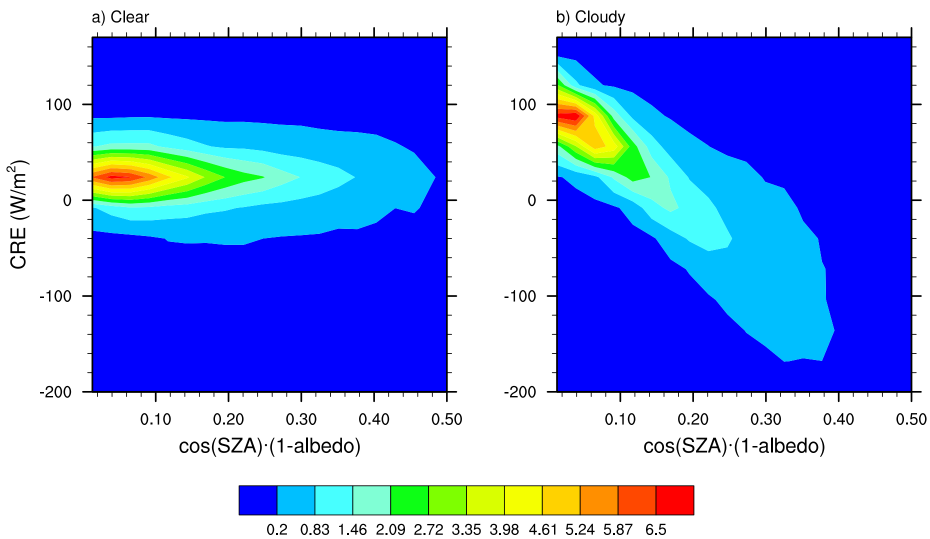

Figure 3.11: Normalized joint probability density function of combined SZA and albedo with CRE in a) clear and b) cloudy radiative states at all PROMICE stations.

3.8 Summary

In this study, we adjust the radiative and meteorological measurements from automatic weather stations (AWSs) to improve data quality, estimate cloud radiative effects (CREs) from the adjusted radiation, and investigate the contributions of the non-cloud factors, albedo and solar zenith angle (SZA), to CRE's spatial distribution, seasonal cycles, and hourly variability during Greenland's melt season.

In order to improve data quality, we assess AWS measurements using physical limits and inter-variable relationships, and adjust data to reduce biases caused by typical AWS problems such as station tilt, pyrgeometer dome overheating, and riming on sensor domes. We use the Retrospective, Iterative, Geometry-Based (RIGB) tilt-correction method to reduce the bias in solar radiation introduced by station tilt. We remove the potential overheating suggested by the manufacturer and the potential riming cases identified by longwave downwelling exceeding longwave upwelling radiation. We also exclude data with drastic hourly variability of albedo as another way of reducing riming effects. The "instantaneous CRE" is estimated by subtracting the clear-sky simulation from the all-sky observation. The clear-sky simulation is evaluated at three human-attended stations in the Arctic. The overall simulation uncertainty is on the magnitude of 10 W m^{-2}.

In our analysis of CRE spatial distribution, we find that currently during melt season, clouds warm most of Greenland's surface, showing greater warming from the longwave greenhouse effect of clouds than cooling from the shortwave shading effect. On the other hand, the larger variability of shortwave CRE determines the overall spatial distribution. The net warming CRE decreases as shortwave CRE becomes stronger from high to low altitudes and from north to south. The largest net CREs are 41±14 W m^{-2} and 41±8 W m^{-2} in the northern and southern accumulation zones, respectively, and the smallest is 5±18 W m^{-2} in the lower southern ablation zone. This large spatial variability is mainly caused by surface albedo. Surface albedo, that declines from ∼0.8 in the accumulation zone to ∼0.4 in the lower ablation zone, and below 0.2 over bare rocks, substantially modulates surface radiation. The correlation coefficient between the station-average albedo and net CRE is up to 0.93 ($p << 0.01$). The spatial variability of SZA is small because the smaller $\cos(SZA)$ at noon in the north is compensated by the longer daylight duration. The similar spatial distribution of shortwave downwelling CRE and albedo suggests that the cloudiness and/or cloud optical depth work in accordance with albedo in determining CRE spatial distribution. However, the dominating spatial correlation between albedo and CRE makes cloud changes a secondary factor.

The seasonal trend of net CRE in the accumulation zone is controlled by longwave CRE related to cloud fraction and liquid water content. It increases from May to July and flats out in August. The net CRE seasonal trend in the ablation zone is determined by shortwave CRE and in turn by surface albedo. It decreases from May to July and recovers in August. The contrasting seasonal trends across geographical zones explain the dispute in previous studies on CRE in the Arctic. The accumulation zone trend agrees with the study at Summit, Greenland (*Miller et al.*, 2015). The ablation zone trend agrees with the studies in the Arctic ocean (*Intrieri et al.*, 2002; *Shupe and Intrieri*, 2004; *Kay and L'Ecuyer*, 2013). The longwave CRE seasonal trend also varies in different regions. The large ascending trend at the beginning of melt season in the northern accumulation zone gradually becomes descending towards south and the ablation zone. At Summit in the northern accumulation zone, the longwave trend is in accordance with the seasonal variability of cloud fraction and liquid water content. However, in the ablation zone, the longwave trend is against the cloud property changes inferred from shortwave downwelling CRE, and therefore might be largely controlled by the under-cloud temperature and humidity. The shortwave seasonal cycle is similar across regions with different amplitudes, strongly correlated with local albedo ($r > 0.90$ in the ablation zone and $r > 0.70$ in the accumulation zone; $p << 0.01$ for both). The influence of SZA, which peaks in June instead of July, only shows a weak correlation.

On the hourly timescale, Greenland is either nearly clear or opaquely cloudy most of the time, forming two semi-distinct radiative states. These two states can be approximately separated by net longwave of -35 W m^{-2}. In the clear state associated with clear skies or thin clouds, CRE is small (23±27 W m^{-2}), and slightly affected by SZA and albedo. In the cloudy state with opaque clouds, CRE is larger and varies greatly (40±78 W m^{-2}), and strongly correlated with the combination of SZA and albedo. The longwave CRE response to cloud liquid water content increases might already reach saturation in this state, making the net CRE dominated by shortwave, and therefore by SZA and albedo. Among the two, SZA shows a slightly higher correlation with CRE than albedo ($r = -0.59$ for SZA and $r = 0.50$ for albedo; $p < 0.01$ for both).

Although cloud properties inherently influence CRE and dominate the seasonal trend in the accumulation zone where albedo is constantly high, the large variability of albedo and SZA during melt season determines CRE's spatial distribution, seasonal trends in the ablation zone, and hourly variability in the cloudy radiative state. CRE mediates the radiative energy budgets between the ablation and accumulation zone. In the accumulation zone that currently occupies most of Greenland, clouds warm the cold and bright surface to enhance snow metamorphism and snow melt, and tend to reduce albedo. In the ablation zone that is expanding as Earth warms, CRE becomes more negative as albedo decreases, and clouds tend to cool the warm and dark surfaces and increase albedo, and thus tend to inhibit surface melt. This stabilizing mechanism might also occur in the Arctic ocean, where surface and cloud conditions over sea ice are similar to those in the Greenland's ablation zone, and helps forestall surface melt in the dimmer Arctic.

3.9 Acknowledgments

The authors acknowledge the GC-Net and PROMICE teams for providing AWS measurements, and thank Dr. Nathaniel B. Miller and Dr. David Longenecker for providing the NOAA GMD radiation measurements at Summit, Greenland and patiently answering all our questions. The AIRS level 3 atmospheric profiles were obtained from the Goddard Earth Sciences Data and Information Services Center provided by the Jet Propulsion Laboratory, California Institute of Technology. The ICECAPS radiosonde data at Summit, Greenland were obtained from the data ftp of the Earth System Research Laboratory (ESRL), the National Oceanic & Atmospheric Administration (NOAA). The radiation, meteorology and atmospheric profile data at Barrow, Alaska, U.S.A. were obtained from the Atmospheric Radiation Measurement (ARM) Program sponsored by the U.S. Department of Energy, Office of Science, Office of Biological and Environmental Research, Climate and Environmental Sciences Division. Supported by NASA ACCESS NNX14AH55A and by DOE ACME DE-SC0012998.

Chapter 4

Evaluating spatial distributions of cloud radiative effects

4.1 Introduction

Arctic clouds can profoundly influence surface radiation and thus surface melt. Over Greenland, these cloud radiative effects (CRE) vary greatly with the diverse topography. To investigate the ability of assorted platforms to reproduce the heterogeneous CRE, we evaluate CRE spatial distributions from a satellite product, reanalyses, and a global climate model against estimates from 21 automatic weather stations (AWS). We then identify the most important factors that contribute to the verisimilitude of each gridded dataset. Section 4.2 describes the data and methods we use to estimate CRE and perform comparisons. Section 4.3 presents CRE spatial distribution estimated from in-situ weather stations. Section 4.4 evaluates CRE spatial distributions from gridded datasets against the interpolated maps and inter-station changes of in-situ measurements. Section 4.5 examines the gridded datasets' cloud-radiation physics and evaluates their retrieval of major CRE factors against observations. In Section 4.6, we discuss the shortcomings of CALIPSO retrievals to reveal climatological CRE. Section 4.7 summarizes the main findings of this study and their implications.

4.2 Data and Method

We examine five well-known gridded datasets as mentioned above. They all provide both all-sky and clear-sky surface radiation fields at high spatial resolution and in the melt seasons (i.e., May to August) from 2008–2013.

CERES cloud retrievals integrate MODIS-observed radiance with an emphasis on radiative issues (*Wielicki et al.*, 1996). CERES retrieves cloud top properties, and estimates cloud base height based on empirical formulas. We use their monthly Synoptic Radiative Fluxes and Clouds (SYN) Edition-3A Level-3 data with a spatial resolution of 1°. MERRA reanalyses take advantage of numerous satellite measurements. MERRA-2, a successor of MERRA, uses an updated Goddard Earth Observing System (GEOS) model and assimilates more types of observations (*Gelaro et al.*, 2017). Its monthly clouds and radiation retrievals are in grids of 1/2° latitude and 2/3° longitude. ERA-Interim is the latest global reanalysis from the European Centre for Medium-Range Weather Forecasts (ECMWF) (*Dee et al.*, 2011), which also assimilates both in-situ and satellite observations and uses forecast models to predict cloud properties. It is often employed to drive regional models in the Arctic (*Wesslén et al.*, 2014; *Noël et al.*, 2015; *Fettweis et al.*, 2017). The spatial resolution is $\sim$0.7°. ASR is a high resolution regional reanalysis focused on the Arctic (*Wesslén et al.*, 2014). It uses the High Resolution Land Data Assimilation (HRLDAS) system and the Polar Weather Forecast Model (PWRF) as the forecast model. The highest spatial resolution of ASR is 15 km. In this study, we use ASR 30 km products and regrid to MERRA-2 rectilinear grids using bilinear interpolation. LENS consists of 40 ensemble members from simulations of the fully coupled Community Earth System Model (CESM), including diagnostic ocean biogeochemistry and the atmospheric carbon dioxide cycle (*Kay et al.*, 2015). The large ensemble means reduce the influence of internal climate variabilities. We utilize the LENS RCP8.5 scenario. This closely mimics historical radiative forcing (*Sanford et al.*, 2014) and has a spatial resolution of $\sim 1°$.

Measurements from the 21 AWS (Fig. 4.1) we analyzed have gone through rigorous data quality control to reduce interference from the typical problems experienced by unattended weather stations, including station tilt, low cosine response at large SZA, riming on sensor domes, and sensor overheating. Among the stations, four are from the Greenland Climate Network (GC-Net; *Steffen et al.* (1996)), all in the accumulation zone; the rest are from the Programme for Monitoring of the Greenland Ice Sheet (PROMICE; *van As and Fausto* (2011)), with one station in the accumulation zone. In the ablation zone, PROMICE stations usually install a pair of stations along one glacier. Stations suffixed with "U" (for "upper") are close to the equilibrium line. Stations suffixed with "L" (for "lower") are deep in the ablation zone.

As in *Intrieri et al.* (2002), we define CRE as the difference between all-sky and clear-sky surface radiation. AWS measure all-sky surface radiation. AWS clear-sky radiation is simulated using the Column Radiation Model (CRM) (*Zender*, 1999) driven by the Level-3 Atmospheric Infrared Sounder (AIRS) (*AIRS Science Team/Joao Texeira*, 2013). The uncertainty of clear-sky simulations is less than $10\,\mathrm{W\ m^{-2}}$. The five gridded datasets provide both all-sky and clear-sky surface radiation to estimate CRE.

CERES, MERRA-2, ERA-Interim, and LENS provide both total cloud fraction and low-level cloud fraction. They all define low-level clouds as clouds below 700 hPa. ASR provides the vertical profiles of cloud fraction. For ASR, we use the maximum-random overlap assumption also used by the other four datasets (*Zib et al.* (2012) and personal communication with Dr. Michael G. Bosilovich from NASA) to calculate the total and low-level cloud frac-

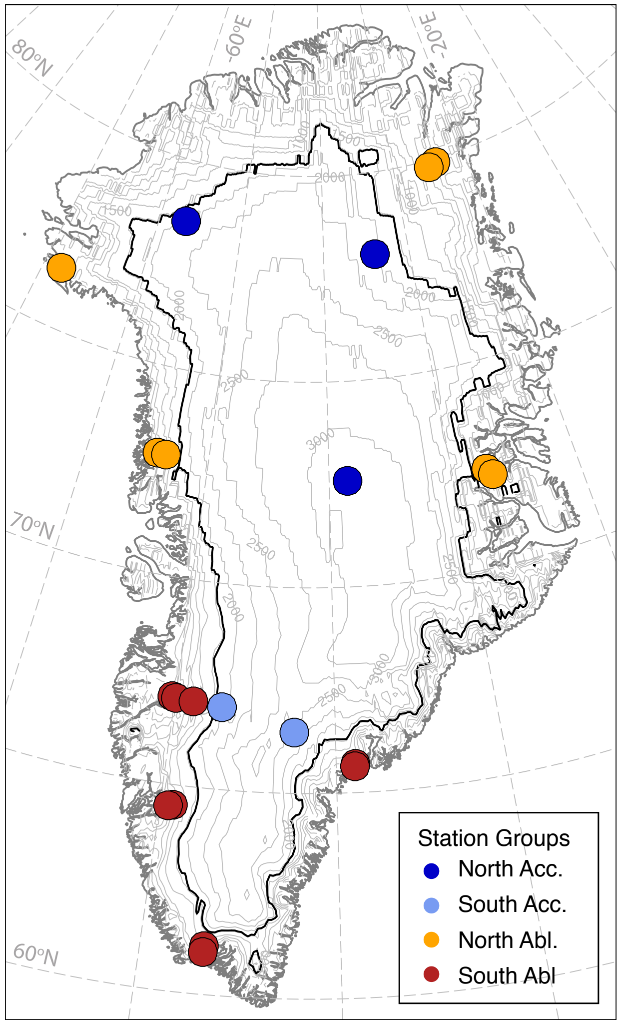

Figure 4.1: Weather stations used in this study with highlighted isoline of 1800 m. Stations in the northern accumulation zone (north of 70°N) are represented in dark blue, southern accumulation zone in light blue, northern ablation zone in yellow, and southern ablation zone in red.

tion. The super cloud layers are defined as in MERRA-2 with altitude thresholds at 700 hPa and 400 hPa. Clouds within one super layer are assumed to be maximally overlapped. Super cloud layers are assumed to be randomly overlapped.

To evaluate cloud fraction and liquid water path from the gridded datasets, We use data from the Integrated Characterization of Energy, Clouds, Atmospheric State, and Precipitation at Summit (ICECAPS), the only multi-year comprehensive in-situ cloud observations in Greenland (*Shupe et al.*, 2013b). ICECAPS retrieves cloud fraction and liquid water path using multiple instruments. *Miller et al.* (2015) estimate cloud fraction using the temporal average of cloud presence detected by Vaisala ceilometer, Millimeter Cloud Radar (MMCR), and MicroPulse Lidar (MPL). Due to the narrow viewing angles of these instruments, this type of cloud fraction might be significantly different from those based on whole sky images (e.g., human and satellite observations), especially when the air is stagnant (*Qian et al.*, 2012). Liquid water path is derived from Humidity and Temperature Profiler (HATPRO) microwave radiometer (MWR) and high-frequency MWR (*Miller et al.*, 2015). The uncertainty is $\sim 3\,\mathrm{g\ m^{-2}}$.

4.3 CRE spatial distribution estimated from in-situ measurements

We interpolate CRE estimates from 21 weather stations to triangular-mesh maps to demonstrate the spatial distribution of CREs. Steep slopes near the coasts render large-scale maps of all of Greenland insufficient to present the large spatial variability in the ablation zone. Therefore, the interpolated maps show only stations in the accumulation zone and in the upper ablation zone. We then use 2-D spaces of latitude-altitude and latitude-albedo to show CRE variability in the ablation zone.

CRE is highest at Summit, lowest near coasts, and generally decreases with elevation (Fig. 4.2a). Shortwave cooling by clouds is weakest near Summit due to the constantly high albedo. Longwave warming effect is strongest there probably due to prevalent low-level liquid-containing clouds (*Shupe et al.*, 2013b; *Miller et al.*, 2015). These clouds most likely form by orographic lifting during warm southerly advection (*Zygmuntowska et al.*, 2012), and are usually decoupled from the surface (*Curry et al.*, 1996; *Shupe et al.*, 2013a; *Tjernström et al.*, 2014) as the surface is drier at higher altitude. As elevation decreases so does albedo, and shortwave CRE strengthens from Summit to the coasts (Fig. 4.2b). The only exception is QAS_U (the southern-most station at 900 m) where albedo is abnormally high (0.67) for its latitude and relative to albedos from nearby stations QAS_L (0.34 at 280 m) and NUK_U (0.64 at 1120 m). As elevation decreases, longwave CRE first decreases until near the equilibrium line and then increases (Fig. 4.2c). This stronger warming effect near coasts might be caused by an increasing cloud fraction, formed mostly by marine stratus clouds (*Walsh et al.*, 2009). However, on the southeastern coast next to relatively warm Atlantic water (TAS), there is no increased warming effect. Due to the persistent anticyclonic conditions and katabatic winds over Greenland, this area is more likely dominated by the cold northerly air advection than by the warm ocean circulation (*Hanna et al.*, 2014). Nevertheless, between the two neighboring PROMICE stations at TAS, the lower station, TAS_L, has a higher longwave CRE than the upper station, TAS_U, demonstrating an increasing warming effect with lower altitude (Fig. 4.3c). Net CRE, the sum of shortwave and longwave CRE, decreases monotonically from Summit to the coasts. At a similar altitude, e.g., THU_U (north) and NUK_U (south), net CRE is higher in the north than in the south, mostly due to shortwave CRE.

This CRE spatial distribution is robust considering the seasonal variability (Fig. 4.3). The statistics of 20-day running average CRE during melt seasons also show decreasing values from the accumulation zone (dark and light blue boxes in Fig. 4.3a) to the ablation zone (yellow and red boxes in Fig. 4.3a), with the highest at Summit. Shortwave CRE strengthens from high to low elevation (Fig. 4.3b). Longwave CRE decreases from Summit to near the equilibrium line, and then increases seawards (Fig. 4.3c).

To better resolve the ablation zone, we scatter-plot latitude and elevation (Fig. 4.4a, b, and c). Net CRE is relatively smaller at lower latitudes and elevations (Fig. 4.4a), mostly due to strong negative shortwave CRE in this quadrant (Fig. 4.4b). The longwave CRE distribution is more scattered with slightly higher values at lower elevation (Fig. 4.4c). In

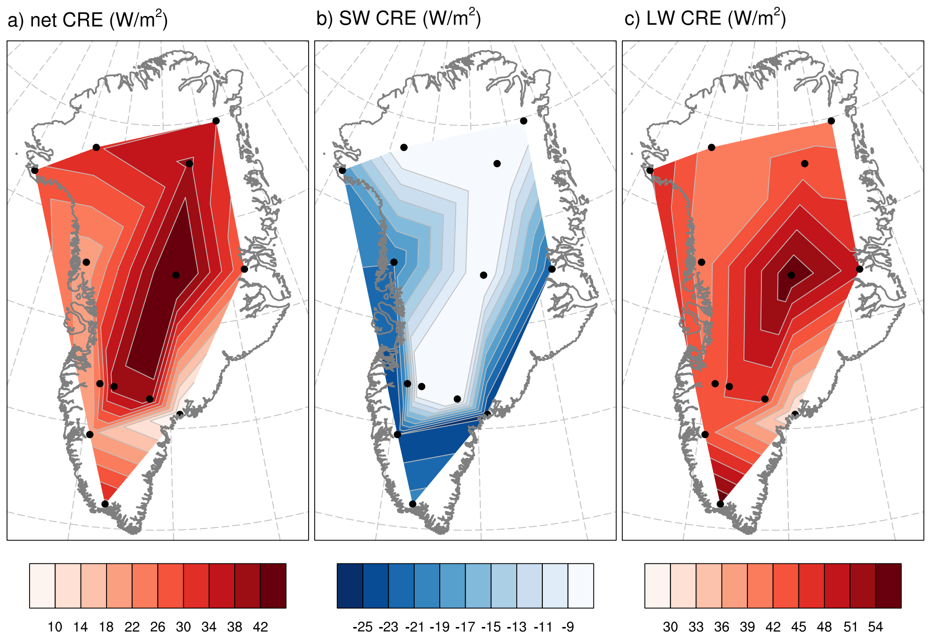

Figure 4.2: Interpolated a) net CRE, b) shortwave CRE, and c) longwave CRE from in-situ weather stations in the accumulation and upper ablation zone (black dots).

the scatter-plot of latitude and albedo, net CRE is better aligned. Net CRE decreases from high albedo to low albedo, similar to shortwave CRE (Fig. 4.4d and e). Therefore, in the ablation zone, albedo mostly determine the spatial distribution of CRE. Although albedo generally decreases with latitude and altitude, the local conditions, e.g., tundra at KAN_B, can also exert a substantial influence.

In summary, net CRE over Greenland presents a "warm center" spatial pattern: peaking at Summit and decreasing toward the coasts. Shortwave CRE decreases with elevation, largely due to albedo. Longwave CRE increases away from the equilibrium line, both inland and coastward, probably due to increased cloudiness in those areas.

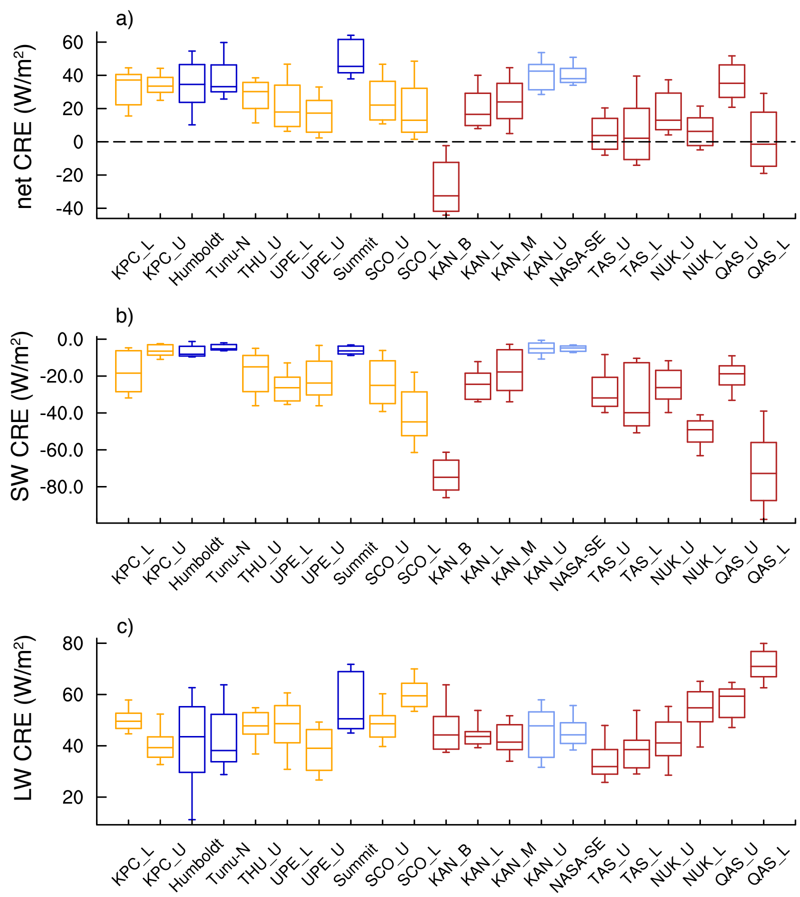

Figure 4.3: Statistics of 20-day running average a) net CRE, b) shortwave CRE, and c) longwave CRE at each weather station. Whiskers show lower decile and upper decile, box lines show upper quartile, median, and lower quartile. Station colors are as in Fig. 4.1.

4.4 Evaluating CRE spatial distributions from gridded datasets against in-situ measurements

4.4.1 CRE maps

CRE areal averages from the five gridded datasets we compare are similar (numbers on top of each panel in Fig. 4.5). However, their spatial distributions present two distinct patterns: "warm center" and "warm L-shape" (south and northwest). MERRA-2, ERA-Interim, and CERES show large positive CRE around Summit area (the "warm center" pattern), while

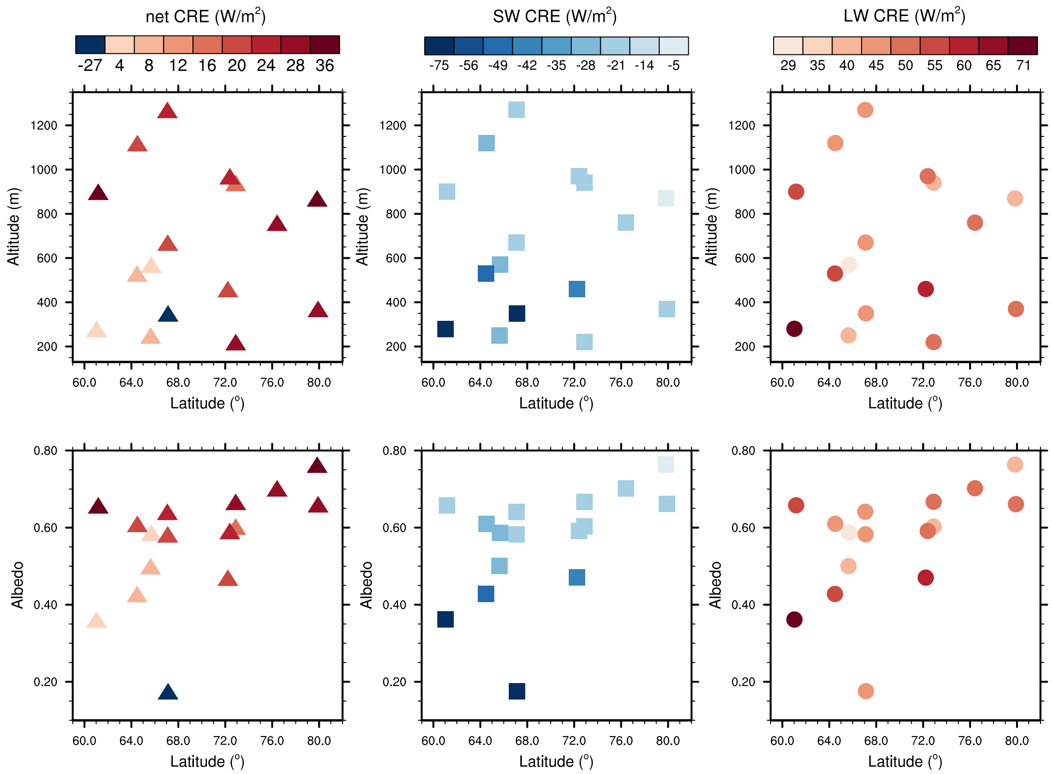

Figure 4.4: Ablation-zone net CRE (left column), shortwave CRE (middle column), and longwave CRE (right column) in scatter plots of latitude-elevation (upper row) and latitude-albedo (lower row).

ASR and LENS show large positive CRE in the south and northwest (the "warm L-shape" pattern). In the "warm center" group, CRE mostly decreases with elevation. The highest values are near Summit with the second highest in the South Dome area. Low values predominate along the coasts with the lowest values in the west. In the "warm L-shape" group, the strongest negative CRE are also in the western ablation zone. However, in the accumulation zone, the positive CRE are smallest in the northeast and increase towards the west and south.

Most inter-dataset discrepancies stem from longwave CRE differences in the accumulation zone. Shortwave CRE spatial distributions from different datasets are similar: weak cooling effects with small variability in the accumulation zone and stronger cooling as elevation decreases (Fig. S1). To compare spatial distributions quantitatively, we interpolate

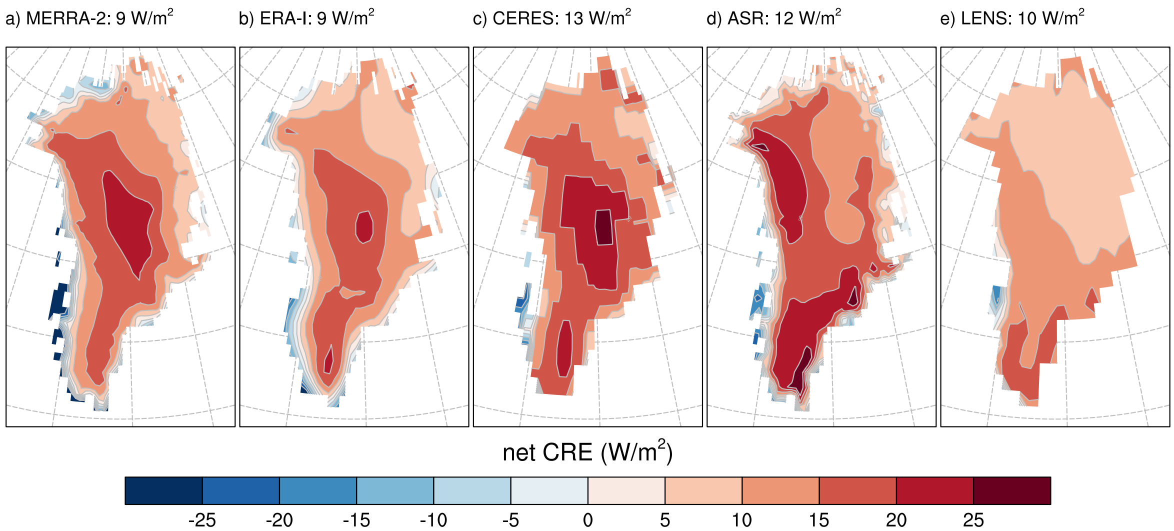

Figure 4.5: Net CRE from a) MERRA-2, b) ERA-Interim, c) CERES, d) ASR, and e) LENS. Numbers on top of panels are areal averages.

the other four onto the LENS grid (one of the lowest spatial resolutions), and calculate their spatial correlations. Shortwave CREs from all datasets are generally well correlated with one another. The correlation coefficients are around 0.8 in the ablation zone and greater than 0.5 in the accumulation zone. Longwave CREs from the "warm center" group (MERRA-2, ERA-Interim, and CERES) are largest at Summit and along the coasts (Fig. 4.6). Longwave CREs from the "warm L-shape" group (ASR and LENS) are larger in the south. ASR also shows strong warming in the northwest. Therefore, only datasets in the same "warm pattern" group are well correlated. Correlation coefficients of datasets from different groups are mostly around 0.3, lower in the accumulation zone than in the ablation zone. Therefore, longwave CRE in the accumulation zone leads to most to the inter-dataset discrepancies in CRE spatial distribution.

4.4.2 CRE inter-station changes

Section 4.4.1 shows that CRE maps from the "warm center" group (MERRA-2, ERA-Interim, and CERES) rather than the "warm L-shape" group (ASR and LENS) better

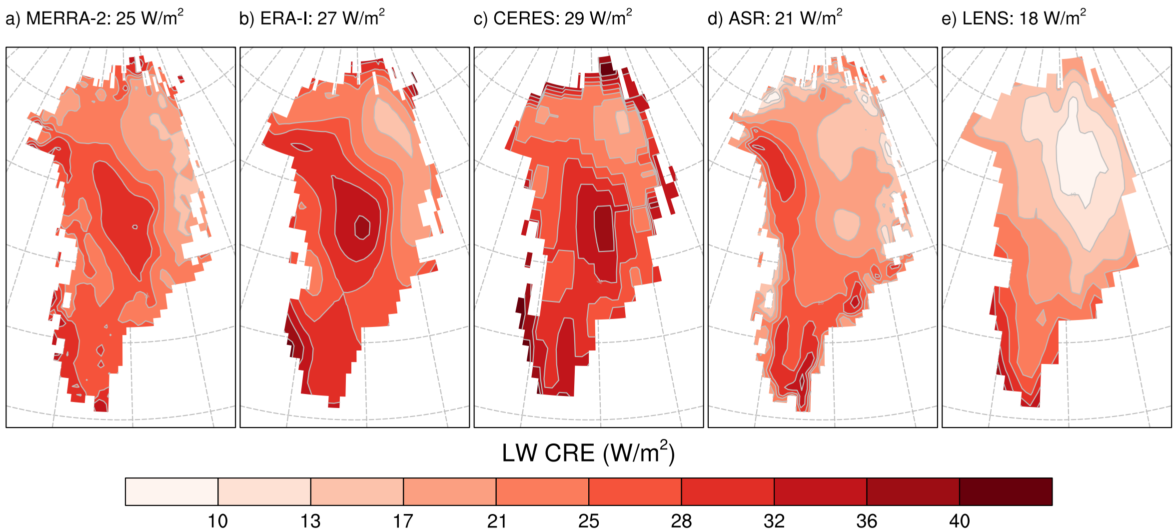

Figure 4.6: Same as Fig. 4.5 but for longwave CRE.

resemble AWS estimates interpolated onto a triangular mesh. In this section, we evaluate CRE in the closest gridcell against in-situ measurements at each weather station. Although temporal averaging can mitigate inter-platform differences, such as footprint size and instrument sensitivity, results from in-situ measurements, remote sensing, and model simulations are never the same (*Li and Trishchenko*, 2001). Therefore, we focus on the relative changes between stations rather than on the absolute differences.

Shortwave CRE from all gridded datasets successfully reproduce the major transitions between the ablation and accumulation zones, but not changes inside the ablation zone with steeper slopes (Fig. 4.7a and b). In the north, all gridded datasets show decreasing shortwave CRE from Tunu-N down to UPE and increasing shortwave CRE back up to Summit, as in the in-situ observation (Fig. 4.7a). However, on the eastern side, from Summit to SCO, most gridded datasets only show a slightly decreasing trend. ERA-Interim even shows an increasing trend. In the ablation zone, no gridded dataset shows a lower value at the lower stations between the station pairs (e.g., KPC_U vs. KPC_L). Moreover, CERES, ERA-Interim, and MERRA-2 overestimate the difference between THU with Tunu-N and UPE to different degrees. In the south, all gridded datasets capture the trends from KAN_L to

TAS_U (Fig. 4.7b). CERES closely matches observations between KAN_B and KAN_L on the western side of Greenland, yet it flattens out through the southern coasts. By contrast, ERA-Interim shows better results at the southern-most coasts but not in the west. In our comparisons, higher spatial resolution (e.g., MERRA-2) and shorter distance between grid cell centers and AWS does not improve the agreement between gridded and AWS CRE changes.

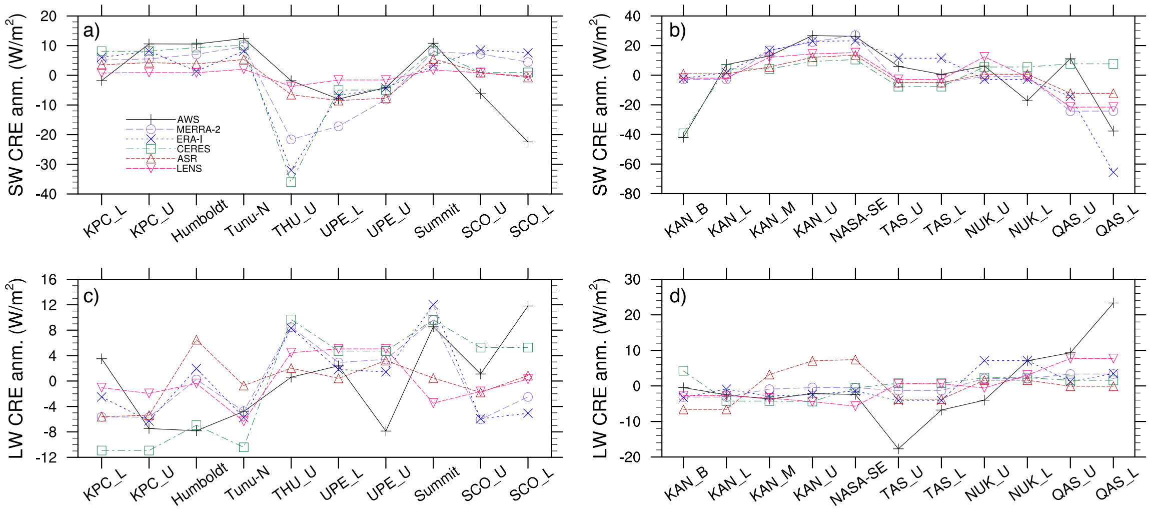

Figure 4.7: Station anomalies of a) shortwave CRE in the north, b) shortwave CRE in the south, c) longwave CRE in the north, and d) longwave CRE in the south from weather stations (black lines with pluses), MERRA-2 (purple lines with circles), ERA-Interim (blue lines with crosses), CERES (green lines with rectangles), ASR (red lines with up-pointing triangles), and LENS (pink lines with down-pointing triangles).

Correlation of longwave CRE from the gridded datasets with in-situ observations is worse than shortwave CRE (Fig. 4.7c and d). In the north, although the "warm center" group of datasets reproduces the relatively strong warming effects at Summit, they overestimate the spatial variability in the northern-most area (between KPC, Humboldt, and THU; Fig. 4.7c). The "warm L-shape" group completely misses the "warm center and warm coasts" spatial features from in-situ measurements. In the south, the gridded datasets underestimate the overall spatial variability. None of them reproduce the large increasing trend from NUK_U to QAS_L (Fig. 4.7d).

The Taylor Diagram summarizes the spatial variabilities of the gridded datasets and the in-situ station measurements, as well as correlations between them (Fig. 4.8). Since absolute values are not in the scope of this study, we do not include root-mean-square difference (RMSD) circles in the figures. With a high correlation and a similar variability, net CRE from MERRA-2 most closely resembles in-situ observations. It produces the best shortwave CRE and mediocre longwave CRE. Net CRE from CERES, ASR, and ERA-Interim also correlate relatively well with observations; however, their spatial variabilities are too small. The global climate model, LENS, with fully prognostic clouds and environmental conditions presents the worst resemblance. Overall, shortwave CRE is better represented in the gridded datasets than longwave CRE, among which ASR shows almost zero correlation with observations.

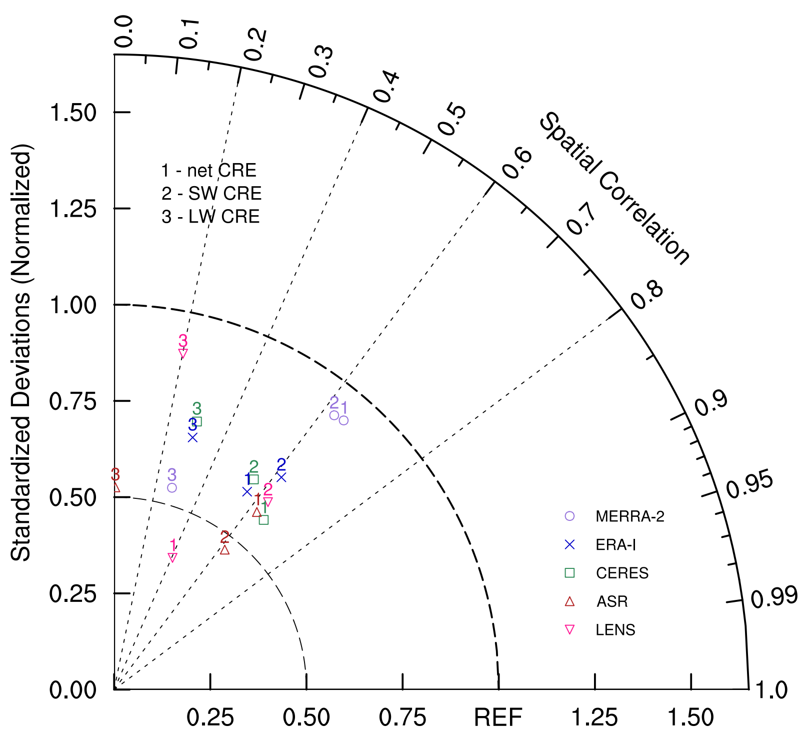

Figure 4.8: Spatial correlations and normalized standard deviations of 1) net CRE, 2) shortwave CRE, and 3) longwave CRE estimated from the five gridded datasets (colors and markers as in Fig. 4.7) comparing with in-situ observations.

4.5 Examining model cloud-radiation physics and estimates of CRE factors

The net effects of clouds on surface energy budget result from a complex synthesis of cloud macro-properties, such as cloud fraction and water path, cloud micro-properties, such as cloud phase and particle size, and environmental conditions, such as surface albedo in melt season (*Arking*, 1991; *Curry et al.*, 1996; *Shupe and Intrieri*, 2004; *Cox et al.*, 2015; *Verlinde et al.*, 2016). The quality of CRE estimates depends not only on obtaining the accurate quantities of these factors but also on reproducing their interactions. All the platforms, satellites, reanalyses, and models, use radiation transfer models to estimate surface radiative fluxes (*Wielicki et al.*, 1996; *Geier et al.*, 2003; *Walsh et al.*, 2009). The difference is how they retrieve cloud properties and environmental conditions. Satellite products use remote-sensed cloud properties and atmospheric and surface conditions to diagnose cloud radiative characteristics. Reanalyses forecast cloud properties based on assimilated atmospheric and surface conditions (*Walsh et al.*, 2009). Fully coupled climate models simulate both clouds and environmental conditions. In this section, we examine the cloud-radiation physics in the five datasets, as well as evaluate the major factors determining CREs against in-situ observations where possible.

In the Arctic, low-level liquid-containing clouds contribute the most to surface radiation balance. (*Shupe and Intrieri*, 2004; *Turner et al.*, 2007; *Bennartz et al.*, 2013; *Miller*, 2017). Radiation that reaches surface is then substantially altered by albedo in melt season. Therefore we count total cloud fraction, low-level cloud fraction, cloud water path (both liquid and ice), and surface albedo as major CRE factors. For each CRE component (shortwave, longwave, and net), we calculate its spatial correlation with these major CRE factors, and present them on a polar coordinate using radii. (Fig. 4.9).

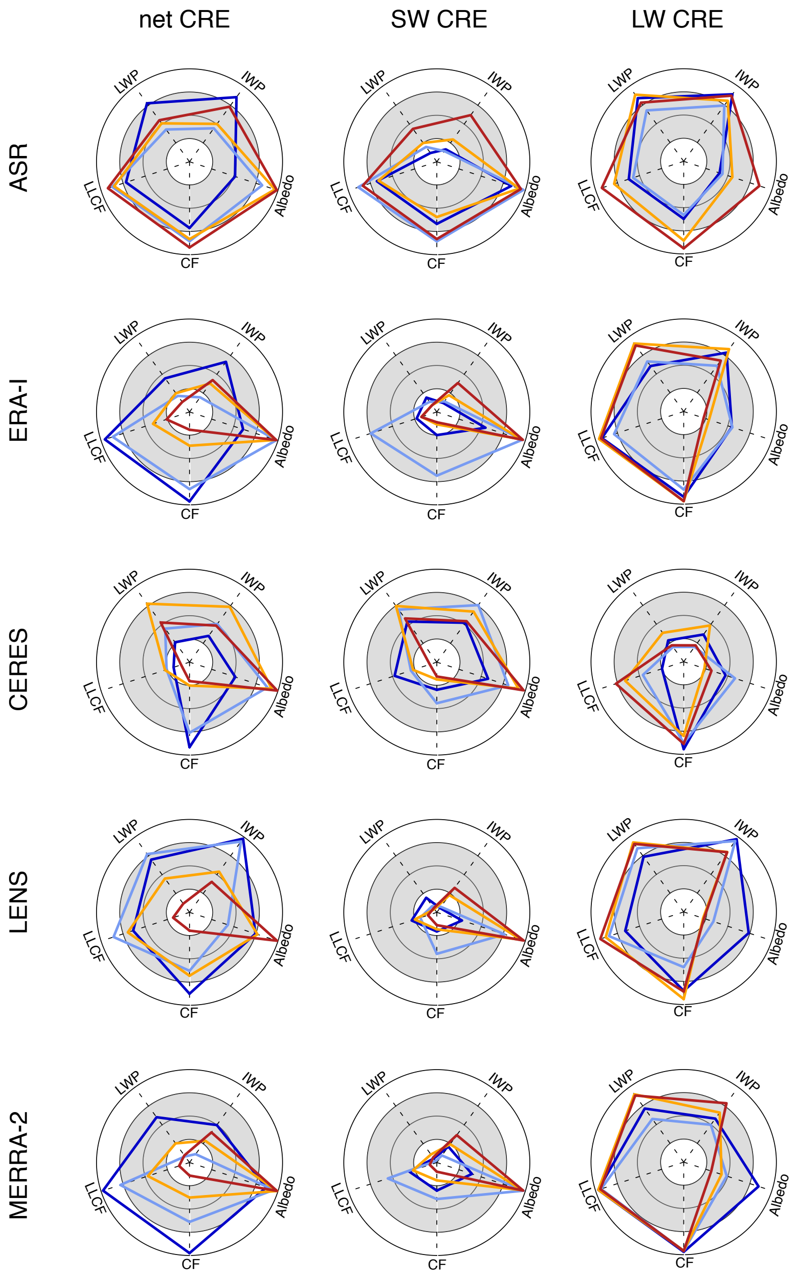

Figure 4.9: Correlations of CRE major factors (cloud fraction, low-level cloud fraction, liquid water path, ice water path, and albedo) with net CRE (left column), shortwave CRE (middle column), and longwave CRE (right column) from the five gridded datasets (each represented in one row). Colors represent different regions defined the same as in 4.1.

Cloud-radiation physics in MERRA-2, ERA-Interim, and LENS is generally consistent with current understandings from in-situ observations (*Curry et al.*, 1996; *Shupe and Intrieri*, 2004; *Walsh et al.*, 2009; *Qian et al.*, 2012; *Bennartz et al.*, 2013; *Shupe et al.*, 2013b; *Miller et al.*, 2015), among which MERRA-2 agrees the best. Observations show that net CRE is largely determined by its shortwave component in the ablation zone, and by longwave CRE in the accumulation zone. Albedo dominates the spatial variability of shortwave CRE in the ablation zone (*Shupe and Intrieri*, 2004). Cloud fraction and liquid water path contribute negatively, and become major influences in the accumulation zone (*Shupe and Intrieri*, 2004). The responses of longwave CRE to major CRE factors are more complicated. Cloud fraction, consisting mostly of low-level cloud fraction, is the primary influence (*Shupe and Intrieri*, 2004; *Walsh et al.*, 2009; *Qian et al.*, 2012; *Bennartz et al.*, 2013). Liquid water path also contributes significantly (*Shupe and Intrieri*, 2004), even at Summit (*Bennartz et al.*, 2013; *Shupe et al.*, 2013b; *Miller et al.*, 2015).

All datasets show strong correlations (exceeding 0.5) between shortwave CRE and albedo in the ablation zone and in the southern accumulation zone. In the accumulation zone, especially in the north, where albedo is less dominant, shortwave CRE is negatively correlated with cloud water path in all gridded datasets except CERES. Nevertheless, the contribution of this negative relationship to net CRE is negligible. Shortwave CRE in ASR incorrectly increases along with cloud fraction in the southern regions.

Longwave CRE from MERRA-2 and ERA-Interim are dominated by low-level cloud fraction in all regions. ASR shows this relationship only in the ablation zones. LENS shows it in the ablation zones and the southern accumulation zone. Total cloud fraction alone determines CERES longwave CRE. All datasets except LENS show weaker correlations of longwave CRE to cloud water paths (liquid and ice). MERRA-2 is the only dataset that shows greater importance in liquid water path than in ice water path throughout all regions. ERA-Interim, ASR, and LENS present a higher correlation between longwave CRE and ice water path in the accumulation zone. The longwave CRE-IWP correlation in LENS exceeds the correlation of CRE with cloud fractions. In CERES, increased cloud water path reduces longwave CRE, opposite to theory and in-situ observations. The strong correlations between albedo and longwave CRE in ASR and MERRA-2 are more likely to be concurrent events rather than causal links. These disparate responses of longwave CRE to major CRE factors inhibit the gridded datasets from reproducing in-situ observed longwave CRE patterns (Fig. 4.8).

We evaluate albedo retrievals from the gridded datasets at each weather station using monthly data averaged over 2008–2013 to increase robustness and avoid asymmetrical seasonal cycles caused by missing values. ASR and MERRA-2 agree best with in-situ measurements 4.10. ERA-Interim, CERES, and LENS overestimate albedo in the ablation zone, and this reduces their spatial variability. Moreover, AWS observations may already overestimate albedo by up to 0.1 due to underrepresentation of albedo spatial heterogeneity (*Ryan et al.*, 2017). Therefore, all gridded datasets may overestimate albedo and underrepresent its spatial variability.

We now evaluate cloud fraction and liquid water path from the gridded datasets with data from ICECAPS. During the three melt seasons from 2011–2013, CERES is the closest to in-situ observations for both cloud properties, in both magnitude and variability 4.11. The cloud fraction qualities of MERRA-2, ERA-Interim, and LENS are similar with either relatively consistent magnitudes or variabilities, but not both. ASR overestimates cloud fraction considerably with almost no seasonal variability. The discrepancies in liquid water path are larger. LENS shows negligible values throughout the whole melt season. MERRA-2 misses the variability. ERA-Interim and ASR underestimates the magnitude. Most of these features also exist in the comparisons between datasets over the entire Greenland (Fig. 4.12). MERRA-2, ERA-Interim, CERES, and LENS present a similar cloud fraction spatial distribution, with high values centered over Summit and near southwestern and northern coasts.

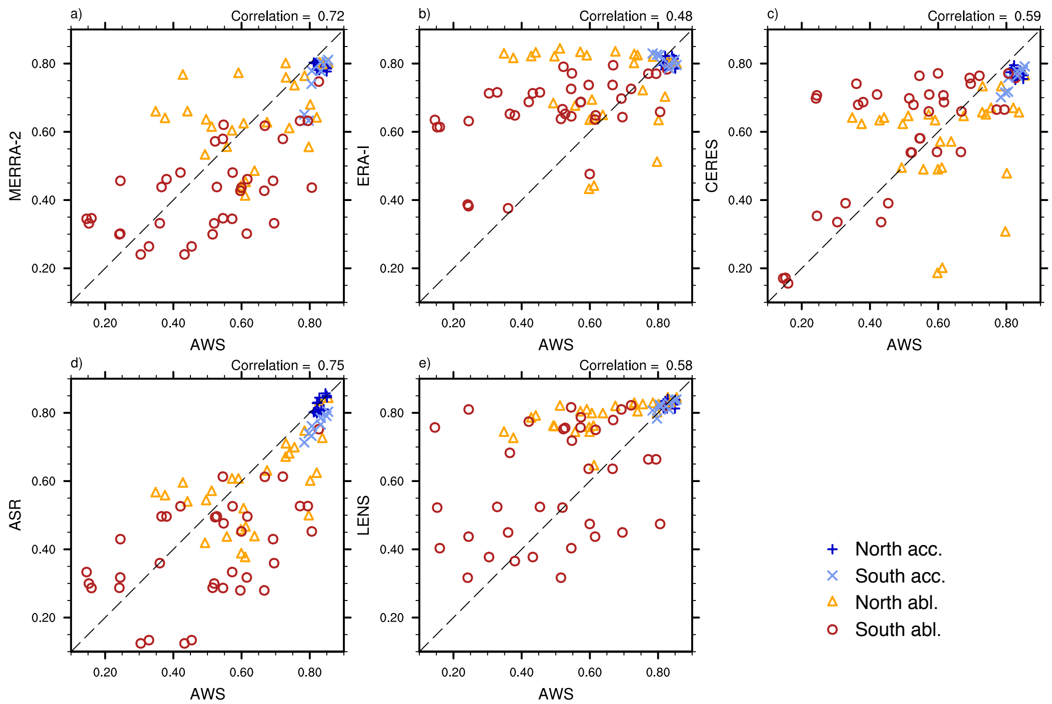

Figure 4.10: Monthly albedo averaged over 2008–2013 from a) MERRA-2, b) ERA-Interim, c) CERES, d) ASR, and e) LENS against weather stations. Colors represent different regions defined as in 4.1.

ASR substantially overestimates cloud fraction, with the lowest values close to the averages of others. The liquid water path spatial distributions are more consistent than cloud fraction. It generally increases with altitude. Nevertheless, the low centers shift from Summit in CERES and LENS towards northwest in ERA-Interim and MERRA-2. The spatial distribution in ASR is quite scattered. CERES still has the largest retrievals. MERRA-2 and ERA-Interim come the next. LENS liquid water path is almost one magnitude smaller than others.

In summary, MERRA-2 captures the major features of cloud-radiation physics and simulates well both albedo and cloud properties, resulting in the best CRE estimates among the five gridded datasets examined here. ERA-Interim reproduces both good physics and cloud properties. Therefore, ERA-Interim presents the same spatial distribution as in-situ weather stations, a "warm center" pattern. The physics of LENS is mostly similar to in-situ esti-

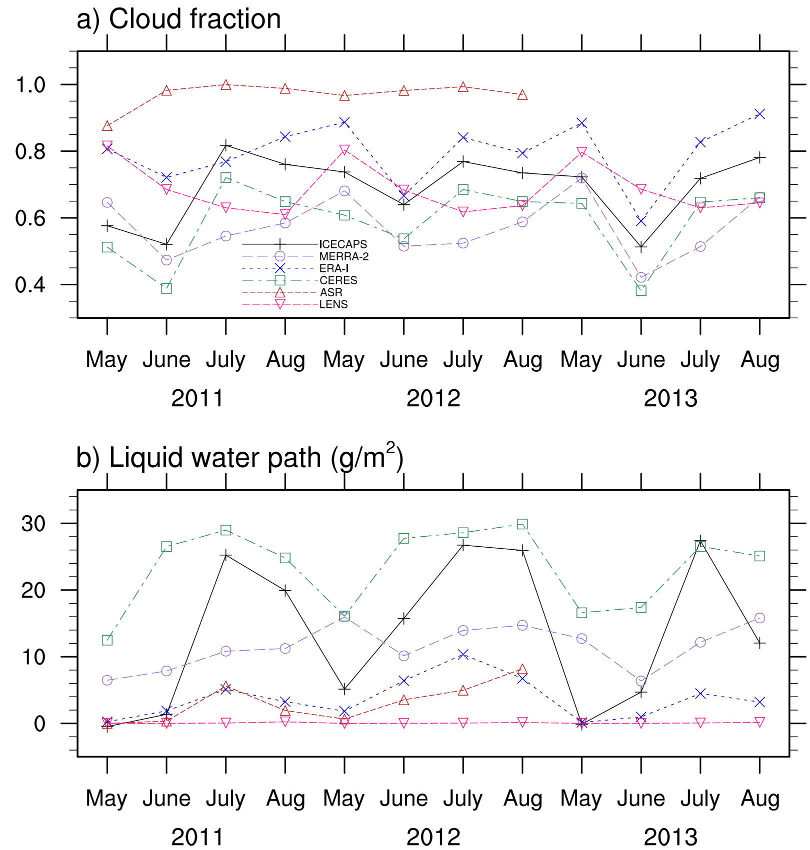

Figure 4.11: Cloud fraction and liquid water path from in-situ observations and the five gridded datasets at Summit in melt seasons from 2011-2013. Symbols are as in Fig. 4.7

mates. However, LENS predicts liquid water path almost one magnitude smaller than in-situ observations. Moreover, due to the favorable response of longwave CRE to ice water path instead of to cloud factions in the accumulation zone, net CRE in LENS presents a "warm L-shape" spatial distribution (similar to that of ice water path; Fig. S2). CERES exhibits an incorrect negative correlation between longwave CRE and cloud water path. Nevertheless, with the dominant influence and good simulation of cloud fraction, CERES also presents a "warm center" CRE distribution. ASR achieves the best albedo. However, it falsely correlates shortwave CRE and cloud fractions in a positive manner, and overestimates cloud fraction substantially, leading to a different CRE spatial pattern as in-situ observations.

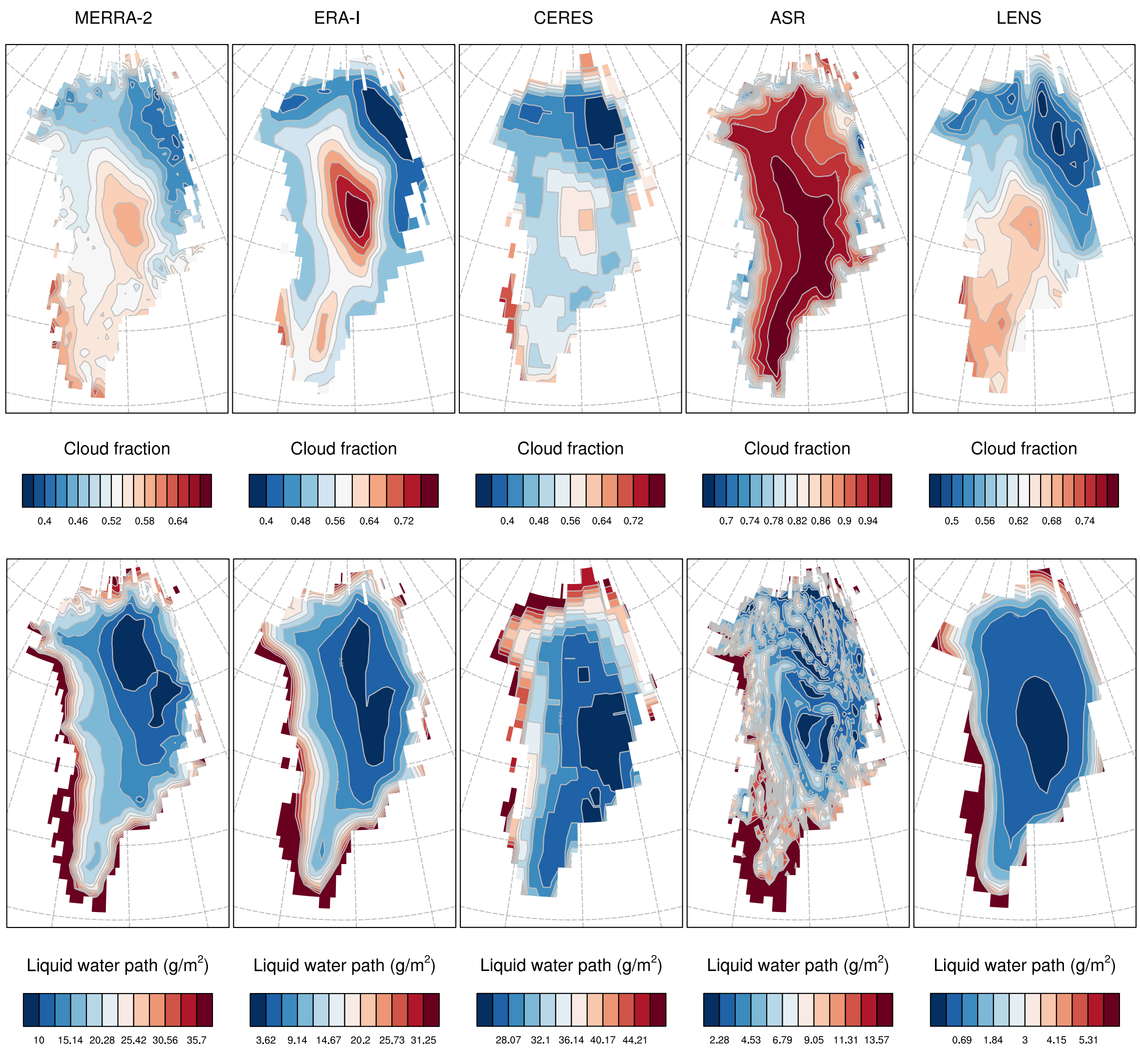

Figure 4.12: Cloud fraction (upper row) and liquid water path (lower row) from the five gridded datasets (each represented by one column) in melt seasons from 2008-2013. The inter-dataset differences are too large to have a common color label.

4.6 Discussion: "warm L-shape" CRE spatial distribution from CALIPSO

Annual mean CRE estimated using CALIPSO products shows a "warm L-shape" spatial distribution during 2007-2010 with a spatial average of 29.5 W m^{-2} (*Van Tricht et al.*, 2016). This annual distribution differs from the in-situ observed "warm center" one in melt season. In order to preclude the influence of seasonality and inter-annual variability, we estimate annual mean CRE during the same time period as *Van Tricht et al.* (2016) using MERRA-2. The annual mean is close (21 W m^{-2}) considering the large range of CREs. However, MERRA-2 still exhibits a "warm center" distribution with the only exception in the northern ablation zone (Fig. 4.13). We expect this distribution because in the accumulation zone, longwave CRE and shortwave CRE both decrease with altitude. Therefore, the spatial distributions in winter, when there is only longwave radiation, and in summer, when there are both longwave and shortwave radiation, are similar. In the sunlit southern ablation zone, net CRE also decreases with altitude, same as in summer. However, in the northern ablation zone, where there is no sunlight during winter, net CRE (dominated by longwave CRE) increases instead of decreases with altitude towards coasts. As mentioned above, although with active sensors, CALIPSO products reportedly provide more accurate instantaneous cloud observations (e.g., *Cesana and Chepfer* (2012); *Chan and Comiso* (2013); *Kay and L'Ecuyer* (2013); *Henderson et al.* (2013)), their sparse spatial-temporal sampling might hinder the ability to reproduce climatologies (*Kay and L'Ecuyer*, 2013; *Liu*, 2015).

4.7 Summary

We establish the melt-season spatial distribution of CRE over Greenland, estimated from 21 in-situ weather stations. We use these results to evaluate CRE spatial distributions from

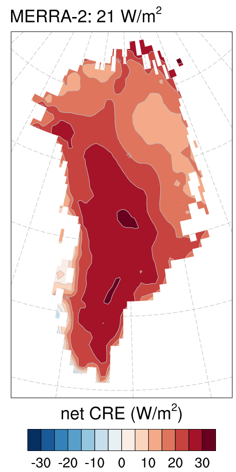

Figure 4.13: Annual mean CRE from MERRA-2 during 2007-2010. Number on top is the areal average.

five datasets including one satellite product, CERES, two global reanalyses, MERRA-2 and ERA-Interim, one regional reanalysis, ASR, and one global climate model, LENS. We also examine the fidelity of the cloud-radiation physics in the gridded dataset results, and their ability to reproduce major factors that determine CREs in order to understand the inter-dataset differences.

Net CRE peaks near Summit, and decreases with elevation to reach a minimum along coasts. This forms a "warm center" spatial distribution over Greenland. In the accumulation zone, both longwave and shortwave CRE values decline with elevation. In the ablation zone, although longwave CRE strengthens coastward, the larger spatial variability of shortwave CRE causes net CRE to decrease towards coasts. MERRA-2, ERA-Interim, and CERES exhibit a similar "warm center" CRE spatial distribution to in-situ observations. ASR, LENS, and CALIPSO present a "warm L-shape" spatial distribution with strong warming in the south and northwest. The largest discrepancy between the two patterns occurs in the accumulation zone where inconsistent cloud-radiation physics alter longwave CRE. MERRA-2, ERA-Interim, and CERES reproduce the strong correlations between longwave CRE and cloud fraction in the accumulation zone. In addition with relatively good simulations of cloud fraction, their net CRE warm the center of Greenland the most. On the other hand, ASR and

LENS show stronger correlations between longwave CRE and ice water path, which increases from north to south. Moreover, ASR overestimates cloud fraction, and LENS underestimates liquid water path, resulting in too-small spatial variabilities.

We also evaluate CRE from the five datasets at each weather station to better examine shortwave CRE and ablation zones. Due to accurate model physics and simulations of both albedo and cloud properties, MERRA-2 CRE agree the best with in-situ measurements, considering both spatial correlation and variability. In all datasets except ASR, albedo dominates shortwave CRE in the ablation zone and in the southern accumulation zone, consistent with in-situ observations. ASR exhibits an incorrect positive correlation between shortwave CRE and cloud fraction, diminishing the influence of albedo, which it reproduces the best. In the northern accumulation zone, shortwave CREs in MERRA-2, ERA-Interim, ASR, and LENS also capture the influence by cloud water path, although the contribution to net CRE is small.

Our results provide ground truth to determine the actual spatial distribution of CRE over Greenland, and highlight the most important factors for successfully reproducing CRE on large scales. Passive sensors, although have their own drawbacks in snow-covered and low-insolation areas, produce a better CRE climatology than active sensors with narrow swaths. The "warm center" CRE spatial distribution established from in-situ measurements, MERRA-2, ERA-Interim, and CERES indicates the role of clouds as a mediator in surface melt over Greenland. Clouds warm the most the bright and cloudy Summit area where surface melt is mild. Clouds cool the dark and cloudy coasts, especially in the west, where heavy mass loss occurs.

4.8 Acknowledgements

W. Wang thanks Dr. Michael G. Bosilovich for explaining the details of MERRA-2 cloud retrieval processes. The GC-Net data were obtained from the Steffen Research Group, the Cooperative Institute for Research in Environmental Sciences (CIRES). The PROMICE data were obtained from the PROMICE website, operated by the Geological Survey of Denmark and Greenland (GEUS) collaborated with the (Technical University of Denmark) DTU Space and Asiaq, Greenland Survey. The CERES data were obtained from the NASA Langley Research Center Atmospheric Science Data Center. The MERRA-2 data were obtained from the NASA EARTHDATA, provided by the Global Modeling and Assimilation Office (GMAO) from NASA Goddard Space Flight Center. The ERA-Interim data were obtained from the European Centre for Medium-Range Weather Forecasts. The ASR data were obtained from the National Center for Atmospheric Research/University Corporation for Atmospheric Research (NCAR/UCAR) and Polar Meteorology Group, Byrd Polar Research Center, the Ohio State University. The LENS data were obtained from the Earth System Grid at NCAR. The ICECAPS data were from *Miller et al.* (2015) provided by Dr. Nathaniel B. Miller. Supported by NASA ACCESS NNX14AH55A and by DOE ACME DE-SC0012998.

Chapter 5

Conclusions

5.1 Summary of results

This dissertation develops and applies new methods to estimate cloud radiative effects (CRE) from 30+ Automated Weather Station (AWS) radiation measurements over Greenland to investigate the contribution of clouds to surface melt. We first invent a method to retrospectively reduce biases in insolation measurements caused by station tilt, a major problem in AWS measurements in polar regions (Chapter 2). We then use the adjusted radiation to present the unique features of CRE over snow-covered surfaces in Greenland on hourly, monthly, and seasonal time scales, and to assess the relative importance of influences from cloud properties, surface albedo, and solar zenith angle (Chapter 3). Lastly, we establish, for the first time, the spatial distribution of CRE over Greenland with measurements rather than models of cloudy sky surface insolation. We use this improved CRE dataset to evaluate the abilities of well-known satellite products, reanalyses, and climate models to reproduce the CRE distribution (Chapter 4).

In Chapter 2, we found that more than 60% of AWS measurements in Greenland suffer from station tilt, which can cause up to 200 W m^{-2} instantaneous bias in measured insolation. We developed and used the Retrospective Iterative Geometry-Based method (RIGB) to correct station tilt by estimating tilt angles and directions using CRM-simulated and AWS-measured insolation under clear-sky conditions. When compared to CERES and MERRA, RIGB-adjusted data show a 16 W m^{-2} smaller RMSE, and a higher correlation (0.95) than unadjusted data. The average improvement under all-sky conditions is 11 W m^{-2}, equivalent to 0.24 m of snow melt in liquid during melt season. The tilt-corrected data exhibit consistent and more realistic semi-smiling patterns of diurnal albedo, and improve agreement with satellite observations and temperature changes in seasonal and inter-annual variability. Since RIGB only relies on solar geometry and no additional instrumentation, it can remediate the station-tilt problem in historical datasets, and provide consistent radiation measurements on all time scales for surface energy studies in Greenland and other polar regions.

In Chapter 3, we estimate CRE by subtracting CRM-simulated clear-sky radiation from AWS-observed all-sky radiation. The uncertainty in clear-sky simulations is $\sim$10 W m^{-2}, evaluated at three human-attended stations in the Arctic. The tilt-adjusted all-sky radiation is further assessed to reduce biases in longwave radiation caused by riming and overheating of domes. During melt season, clouds warm most of Greenland, due to their strong longwave greenhouse effect. However, the spatial distribution of the net effect is largely determined by surface albedo which induces strong variability in shortwave CRE. Net CRE diminishes as shortwave CRE strengthens from high to low elevation and from north to south. The largest CRE is in the accumulation zone (41$\pm$14 W m^{-2} in the north and 41$\pm$8 W m^{-2} in the south) and smallest in the lower southern ablation zone (5$\pm$18 W m^{-2}). This distribution is dominated by surface albedo, which declines from $\sim$0.8 in the accumulation zone to $\sim$0.4 in the lower ablation zone, and below 0.2 over tundra. The spatial correlation between albedo and net CRE is up to 0.93 ($p << 0.01$). The influence of cloud properties is important, though outweighed by surface albedo.

Seasonal CRE shows contrasting trends in the accumulation and the ablation zones. CRE increases from May to July in the accumulation zone, mainly due to longwave CRE enhancement by cloud fraction and liquid water content. CRE decreases from May to July in the ablation zone, mainly due to strengthened shortwave CRE caused by surface albedo reduction. These different trends in different geographical regions explain a dispute in previous CRE studies in the Arctic: A study at Summit, Greenland exhibits a seasonal trend similar to that in the accumulation zone (*Miller et al.*, 2015). Studies over sea ice exhibit ablation-zone-like seasonal trends (*Intrieri et al.*, 2002; *Shupe and Intrieri*, 2004; *Kay and L'Ecuyer*, 2013).

On an hourly time-scale, CRE exhibits a bimodal distribution, indicating that Greenland is either nearly clear or heavily cloudy most of the time. In the clear state, CRE is small with relatively low variability ($23\pm27\,\mathrm{W\ m^{-2}}$), and shows weak correlation with solar zenith angle and albedo. In the cloudy state, CRE is larger with high variability ($40\pm78\,\mathrm{W\ m^{-2}}$), and strongly correlates with the combination of solar zenith angle and albedo ($r=0.85$, $p<0.01$).

The close relation between albedo and CRE in the ablation zone on all time-scales suggests a stabilizing feedback. Net CRE is negative over the dark surfaces caused by snow melt and snow metamorphism, and thus tends to increase albedo. As Greenland becomes dimmer due to future warming-induced snow metamorphism, this stabilizing feedback might initiate in the current accumulation zone and help decelerate surface melt there.

In Chapter 4, we establish the "warm center" spatial distribution of CRE from AWS measurements. In the accumulation zone, both longwave and shortwave CRE decrease with elevation. In the ablation zone, shortwave CRE with its strong spatial variability dominates the decreasing CRE trends towards coasts. Among the five datasets we analyze directly and one from the literature, MERRA-2, ERA-Interim, and CERES agree with in-situ measurements, showing a similar "warm center" CRE spatial distribution. ASR, LENS, and CALIPSO, on the other hand, exhibit strong warming in the south and northwest, forming a “warm L-shape” distribution not seen by our AWS estimates. The largest CRE discrepancies among datasets stem from cloud-physics differences that affect longwave fluxes in the accumulation zone. Longwave CRE from MERRA-2, ERA-Interim, and CERES primarily correlate with cloud fraction, in agreement with in-situ measurements (*Shupe and Intrieri*, 2004). These three datasets also better estimate cloud fraction and liquid water path than ASR and LENS, and so their CRE spatial distributions agree more closely with AWS observations. Instead, ASR and LENS both exhibit stronger correlations of longwave CRE with ice water path, which increases from north to south, causing a warmer south and northwest. Moreover, ASR substantially overestimates cloud fraction. LENS underestimates liquid water path by an order of magnitude. In comparison to AWS-estimated CRE at each weather station, MERRA-2 agrees better than other gridded datasets, due to accurate model physics and good simulations of both surface albedo and cloud properties. Our Greenland CRE spatial distribution is the first estimate to use in-situ measurements, and provides ground truth to evaluate large-scale datasets. The derived “warm center” pattern suggests that the current narrow-swath active sensors such as CALIPSO may not capture climatological cloud statistics.

5.2 Implications for future studies

AWS provide valuable observations for studies of surface energy budget on ice sheets in Greenland and in Antarctic. With the assistance of RIGB, CRE could be inferred from AWS in other polar regions, such as drifting sea ice, without suffering from leveling problems. Our newly funded NASA project, “Justified AWS” (JAWS), will automate and improve RIGB’s efficiency and portability to provide consistent AWS observations in all polar regions and high-mountain Asia in near real-time. A longer time series of high-quality radiation will enable studies of long-term CRE trends in the context of Arctic warming. The cloud contribution to massive melt events can also be investigated with more comprehensive data from more regions.

Chapter 3 reveals the two semi-distinct radiative states in Greenland's melt season. Mostly Greenland is either nearly clear for a few hours or overcast for a few hours. In the central Arctic in winter, there exists a similar distribution (*Morrison et al.*, 2011). However, both states there persist for a few days. (*Morrison et al.*, 2011) attribute this phenomenon to large-scale advection. When the central Arctic is too dry to form clouds locally, its persistent opaque clouds most likely form during warm southerly advection, which, nevertheless, cannot explain the fast cloudiness transition in Greenland. Further study is necessary to find out the causes, and whether this bimodal cloud distribution exists elsewhere. In any case, our results can be used to evaluate cloud simulations in models and reanalyses on short time scales.

In Greenland, the longwave CRE seasonal trend gradually changes from increasing from May to July at Summit to decreasing in the southern coasts. At Barrow, a coastal station on the north slope of Alaska, longwave CRE also decreases from May to July. Longwave CRE is mostly associated with cloud properties (*Shupe and Intrieri*, 2004). The increasing trend in the accumulation zone is likely linked with southerly flow which may advect more clouds in late summer to warm the surface. However, higher cloudiness does not guarantee a larger longwave CRE. Cloud height and cloud phase are also influential factors. Advection that is warm and dry can reduce relative humidity and hinder cloud formation. The decreasing trend in the southern ablation zone of Greenland and the northern coasts of Alaska is difficult to explain. Cloud formation in these areas is influenced by both large-scale systems and local environments. The relative importance varies with time and location. Heat and moisture transports between snow, sea ice, open water, and tundra in the coastal area can further complicate the conditions. For example, in early summer, although water vapor becomes more abundant, the stable atmosphere with frequent inversions inhibits the growth of clouds over open water (*Kay and Gettelman*, 2009). Spatial variability of temperature and humidity profiles may also play a crucial role by contributing to clear- and cloudy-sky longwave radiation contrasts. Therefore, the exact causal links need to be investigated using systematically evaluated regional models and reanalyses. Answers to this question can also help explain the "warm center" spatial distribution of CRE found in Chapter 4. This intriguing finding documents a higher longwave CRE in the drier area near Summit than in the more humid areas at a lower elevation.

Finally, clouds cool surfaces in the lower ablation zone in melt season, and trigger a stabilizing feedback between albedo and CRE. To better predict melt, it would be useful to understand when and where this feedback initiates. Using linear analysis we can examine the magnitude of this feedback and compare it with other cloud feedbacks, in order to better understand the role of clouds in the Arctic system and simulate their future effects on polar climate.

Bibliography

Ackerman, S. A., R. E. Holz, R. Frey, E. W. Eloranta, B. C. Maddux, and M. McGill (2008), Cloud Detection with MODIS. Part II: Validation, *Journal of Atmospheric and Oceanic Technology*, *25*(7), 1073–1086, doi:10.1175/2007JTECHA1053.1.

AIRS Science Team/Joao Texeira (2013), *Aqua AIRS Level 2 Support Retrieval (AIRS+AMSU)*, version 00 ed., NASA Goddard Earth Science Data and Information Services Center (GES DISC), Greenbelt, MD, USA, doi:10.5067/AQUA/AIRS/DATA207.

Arking, A. (1991), The radiative effects of clouds and their impact on climate, *Bulletin of the American Meteorological Society*, *72*(6), 795–813, doi:10.1175/1520-0477(1991)072⟨0795:TREOCA⟩2.0.CO;2.

Atmospheric Radiation Measurement (ARM) Climate Research Facility (1994), *Data Quality Assessment for ARM Radiation Data (QCRAD1LONG). 2008-05-01 to 2013-05-31, 71.323 N 156.609 W: North Slope Alaska (NSA) Central Facility, Barrow AK (C1).*, Oak Ridge, Tennessee, USA, doi:10.5439/1027372.

Bais, A. F., S. Kazadzis, D. Balis, C. S. Zerefos, and M. Blumthaler (1998), Correcting global solar ultraviolet spectra recorded by a brewer spectroradiometer for its angular response error, *Applied optics*, *37*(27), 6339–6344, doi:10.1364/AO.37.006339.

Bekryaev, R. V., I. V. Polyakov, and V. A. Alexeev (2010), Role of Polar Amplification in Long-Term Surface Air Temperature Variations and Modern Arctic Warming, *Journal of Climate*, *23*(14), 3888–3906, doi:10.1175/2010JCLI3297.1.

Bennartz, R., M. D. Shupe, D. D. Turner, V. P. Walden, K. Steffen, C. J. Cox, M. S. Kulie, N. B. Miller, and C. Pettersen (2013), July 2012 Greenland melt extent enhanced by low-level liquid clouds, *Nature*, *496*(7443), 83–86, doi:10.1038/nature12002.

Biggs, W. W. (2015), Principles of Radiation Measurement, in *Advanced Agricultural Instrumentation. Proceedings from the NATO Advanced Study Institute on Advanced Agricultural Instrumentation*, edited by W. Gensler, 2 ed., pp. 1–17, Martinus Nijhof, Dordrecht, The Netherlands, doi:10.1016/B978-0-12-374271-1.00071-X.

Bogren, W. S., J. F. Burkhart, and A. Kylling (2016), Tilt error in cryospheric surface radiation measurements at high latitudes: a model study, *The Cryosphere*, *10*(2), 613–622, doi:10.5194/tc-10-613-2016.

Box, J. E. (2015), Greenland melt season kicks off slowly in 2015; the new abnormal. http://www.meltfactor.org/blog/greenland-melt-season-kicks-off-slowly-in-2015/.

Box, J. E., and K. Steffen (2000), Greenland Climate Network (GC-NET) Data Reference, *Tech. rep.*, Program for Arctic Regional Climate Assessment (PARCA) Cooperative Institute for Research in Environmental Sciences (CIRES), University of Colorado, Boulder, USA, Boulder, Colorado, USA.

Box, J. E., D. H. Bromwich, and L. Bai (2004), Greenland ice sheet surface mass balance 1991–2000: Application of Polar MM5 mesoscale model and in situ data, *Journal of Geophysical Research*, *109*(D16), D16,105, doi:10.1029/2003JD004451.

Box, J. E., X. Fettweis, J. C. Stroeve, M. Tedesco, D. K. Hall, and K. Steffen (2012), Greenland ice sheet albedo feedback: thermodynamics and atmospheric drivers, *The Cryosphere*, *6*(4), 821–839, doi:10.5194/tc-6-821-2012.

CERES Science Team (2017), NASA Atmospheric Science Data Center (ASDC), doi:10.5067/Terra+Aqua/CERES/SYN1deg3HOUR_L3.003A.

Cesana, G., and H. Chepfer (2012), How well do climate models simulate cloud vertical structure? A comparison between CALIPSO-GOCCP satellite observations and CMIP5 models, *Geophysical Research Letters*, *39*(20), L20,803, doi:10.1029/2012GL053153.

Cesana, G., J. E. Kay, H. Chepfer, J. M. English, and G. de Boer (2012), Ubiquitous low-level liquid-containing Arctic clouds: New observations and climate model constraints from CALIPSO-GOCCP, *Geophysical Research Letters*, *39*(20), L20,804, doi:10.1029/2012GL053385.

Chan, M. A., and J. C. Comiso (2013), Arctic Cloud Characteristics as Derived from MODIS, CALIPSO , and CloudSat, *Journal of Climate*, *26*(10), 3285–3306, doi:10.1175/JCLI-D-12-00204.1.

Chapman, S. (1931), The absorption and dissociative or ionizing effect of monochromatic radiation in an atmosphere on a rotating earth part II. Grazing incidence, *Proceedings of the Physical Society*, *43*(5), 483–501, doi:10.1088/0959-5309/43/5/302.

Chen, J. L., C. R. Wilson, and B. D. Tapley (2006), Satellite gravity measurements confirm accelerated melting of Greenland ice sheet, *Science*, *313*(5795), 1958–1960, doi:10.1126/science.1129007.

Church, J., Y. Ding, D. J. Griggs, M. Noguer, P. J. van der Linden, X. Dai, K. Maskell, and C. A. Johnson (2001), Changes in sea level, in *Climate Change 2001: The Scientific Basis. Contribution of Working Group I to the Third Assessment Report of the Intergovernmental Panel on Climate Change*, edited by D. J. G. J. T. Houghton, Y. Ding, K. M. M. Noquer, P. J. van der Linden, X. Dai, and C. A. Johnson, pp. 639–693, Cambridge University Press, Cambridge, United Kingdom and New York, NY, USA.

Comiso, J. C. (2002), A rapidly declining perennial sea ice cover in the Arctic, *Geophysical Research Letters*, *29*(20), 1956, doi:10.1029/2002GL015650.

Cox, C. J., V. P. Walden, P. M. Rowe, and M. D. Shupe (2015), Humidity trends imply increased sensitivity to clouds in a warming Arctic, *Nature Communications*, *6*, 10,117, doi:10.1038/ncomms10117.

Curry, J. A., W. B. Rossow, D. Randall, and J. L. Schramm (1996), Overview of Arctic Cloud and Radiation Characteristics, *Journal of Climate*, *9*(8), 1731–1764, doi:http://dx.doi.org/10.1175/1520-0442(1996)009⟨1731:OOACAR⟩2.0.CO;2.

Curry, J. A., et al. (2000), FIRE Arctic Clouds Experiment, *Bulletin of the American Meteorological Society*, *81*(1), 5–29, doi:10.1175/1520-0477(2000)081⟨0005:FACE⟩2.3.CO;2.

Dee, D. P., et al. (2011), The ERA-Interim reanalysis: configuration and performance of the data assimilation system, *Quarterly Journal of the Royal Meteorological Society*, *137*(656), 553–597, doi:10.1002/qj.828.

Fettweis, X. (2007), Reconstruction of the 1979–2006 Greenland ice sheet surface mass balance using the regional climate model MAR, *The Cryosphere*, *1*(1), 21–40, doi:10.5194/tc-1-21-2007.

Fettweis, X., J. E. Box, C. Agosta, C. Amory, C. Kittel, and H. Gallée (2017), Reconstructions of the 1900–2015 Greenland ice sheet surface mass balance using the regional climate MAR model, *The Cryosphere*, *11*(2), 1015–1033, doi:10.5194/tc-2016-268.

Flanner, M. G., and C. S. Zender (2006), Linking snowpack microphysics and albedo evolution, *Journal of Geophysical Research*, *111*(D12), D12,208, doi:10.1029/2005JD006834.

Gardner, A. S., and M. J. Sharp (2010), A review of snow and ice albedo and the development of a new physically based broadband albedo parameterization, *Journal of Geophysical Research*, *115*(F1), F01,009, doi:10.1029/2009JF001444.

Geier, E. B., R. N. Green, D. P. Kratz, P. Minnis, W. F. Miller, S. K. Nolan, and C. B. Franklin (2003), *Clouds and the Earth's Radiant Energy System (CERES) Data Management System Single Satellite Footprint TOA/Surface Fluxes and Clouds (SSF) Collection Document*, release 2 ed., 1–231 pp., Primary Authors Science Directorate Science Applications Internation, Hampton, VA.

Gelaro, R., et al. (2017), The modern-era retrospective analysis for research and applications, version 2 (MERRA-2), *Journal of Climate*, *30*(14), 5419–5454, doi:10.1175/JCLI-D-16-0758.1.

Goswami, D., F. Kreith, and J. Kreider (2000), Radiation on tilted surface, in *Principles of Solar Engineering, Second Edition*, 2nd ed., Taylor & Francis, Philadelphia, PA, USA.

Grenfell, T. C., S. G. Warren, and P. C. Mullen (1994), Reflection of solar radiation by the Antarctic snow surface at ultraviolet, visible, and near-infrared wavelengths, *Journal of Geophysical Research*, *99*(D9), 18,669, doi:10.1029/94JD01484.

Hanna, E., X. Fettweis, S. H. Mernild, J. Cappelen, M. H. Ribergaard, C. A. Shuman, K. Steffen, L. Wood, and T. L. Mote (2014), Atmospheric and oceanic climate forcing of the exceptional Greenland ice sheet surface melt in summer 2012, *International Journal of Climatology*, *34*(4), 1022–1037, doi:10.1002/joc.3743.

Harrison, R. G., N. Chalmers, and R. J. Hogan (2008), Retrospective cloud determinations from surface solar radiation measurements, *Atmospheric Research*, *90*, 54–62, doi:10.1016/j.atmosres.2008.04.001.

Henderson, D. S., T. L'Ecuyer, G. Stephens, P. Partain, and M. Sekiguchi (2013), A Multi-sensor Perspective on the Radiative Impacts of Clouds and Aerosols, *Journal of Applied Meteorology and Climatology*, *52*(4), 853–871, doi:10.1175/JAMC-D-12-025.1.

Hofer, S., A. J. Tedstone, X. Fettweis, and J. L. Bamber (2017), Decreasing cloud cover drives the recent mass loss on the Greenland Ice Sheet, *Science Advances*, *3*, e1700,584, doi:10.1126/sciadv.1700584.

Hudson, S. R., S. G. Warren, R. E. Brandt, T. C. Grenfell, and D. Six (2006), Spectral bidirectional reflectance of Antarctic snow: Measurements and parameterization, *Journal of Geophysical Research*, *111*(D18), D18,106, doi:10.1029/2006JD007290.

Intrieri, J. M., C. W. Fairall, M. D. Shupe, P. O. G. Persson, E. L. Andreas, P. S. Guest, and R. E. Moritz (2002), An annual cycle of Arctic surface cloud forcing at SHEBA, *Journal of Geophysical Research*, *107*(C10), 8039, doi:10.1029/2000JC000439.

Kay, J. E., and A. Gettelman (2009), Cloud influence on and response to seasonal Arctic sea ice loss, *Journal of Geophysical Research*, *114*(D18), D18,204, doi:10.1029/2009JD011773.

Kay, J. E., and T. L'Ecuyer (2013), Observational constraints on Arctic Ocean clouds and radiative fluxes during the early 21st century, *Journal of Geophysical Research: Atmospheres*, *118*(13), 7219–7236, doi:10.1002/jgrd.50489.

Kay, J. E., T. L'Ecuyer, A. Gettelman, G. Stephens, and C. O'Dell (2008), The contribution of cloud and radiation anomalies to the 2007 Arctic sea ice extent minimum, *Geophysical Research Letters*, *35*(8), L08,503, doi:10.1029/2008GL033451.

Kay, J. E., et al. (2015), The Community Earth System Model (CESM) Large Ensemble Project: A community resource for studying climate change in the presence of internal climate variability, *Bulletin of the American Meteorological Society*, *96*(8), 1333–1349, doi:10.1175/BAMS-D-13-00255.1.

Kipp & Zonen (2004), Instruction manual for Kipp & Zonen CM3, *Tech. rep.*, Kipp & Zonen B.V., Delft, Holland.

Kipp & Zonen (2008), Instruction manual of Kipp & Zonen CNR4 net radiometer, *Tech. rep.*, Kipp & Zonen B.V., Delft, Holland.

Kuipers Munneke, P., C. H. Reijmer, and M. R. van den Broeke (2011), Assessing the retrieval of cloud properties from radiation measurements over snow and ice, *International Journal of Climatology*, *31*(5), 756–769, doi:10.1002/joc.2114.

Lacour, A., H. Chepfer, M. D. Shupe, N. B. Miller, V. Noel, J. Kay, D. D. Turner, and R. Guzman (2017), Greenland clouds observed in CALIPSO-GOCCP: Comparison with ground-based summit observations, *Journal of Climate*, *30*(15), 6065–6083, doi:10.1175/JCLI-D-16-0552.1.

Li, Z., and A. Trishchenko (2001), Quantifying uncertainties in determining SW cloud radiative forcing and cloud absorption due to variability in atmospheric conditions, *Journal of the Atmospheric Sciences*, *58*, 376–389, doi:10.1175/1520-0469(2001)058⟨0376:QUIDSC⟩2.0.CO;2.

Liu, Y. (2015), Estimating errors in cloud amount and cloud optical thickness due to limited spatial sampling using a satellite imager as a proxy for nadir-view sensors, *Journal of Geophysical Research: Atmospheres*, *120*(14), 6980–6991, doi:10.1002/2015JD023507.

Long, C. N., and T. P. Ackerman (2000), Identification of clear skies from broadband pyranometer measurements and calculation of downwelling effects, *Journal of Geophysical Research*, *105*(D12), 15,609–15,626, doi:10.1029/2000JD900077.

Long, C. N., and Y. Shi (2006), The QCRad value added product: Surface radiation measurement quality control testing, including climatology configurable limits, *Tech. Rep. DOE/SC-ARM/TR-074*.

Miller, N. B. (2017), Forcing and Responses of the Surface Energy Budget at Summit, Greenland, Ph.D. thesis, University of Colorado, Boulder, doi:10.5194/tc-2016-206.

Miller, N. B., et al. (2015), Cloud Radiative Forcing at Summit, Greenland, *Journal of Climate*, *28*(15), 6267–6280, doi:https://doi.org/10.1175/JCLI-D-15-0076.1.

Minnis, P., et al. (2008), Cloud detection in nonpolar regions for CERES using TRMM VIRS and Terra and Aqua MODIS data, *IEEE Transactions on Geoscience and Remote Sensing*, *46*(11), 3857–3884, doi:10.1109/TGRS.2008.2001351.

Minnis, P., et al. (2011), CERES edition-2 cloud property retrievals using TRMM VIRS and Terra and Aqua MODIS data-Part II: Examples of average results and comparisons with other data, *IEEE Transactions on Geoscience and Remote Sensing*, *49*(11), 4401–4430, doi:10.1109/TGRS.2011.2144602.

Mioduszewski, J. R., A. K. Rennermalm, A. Hammann, M. Tedesco, E. U. Noble, J. C. Stroeve, and T. L. Mote (2016), Atmospheric drivers of Greenland surface meltrevealed by self-organizing maps, *Journal of Geophysical Research: Atmospheres*, *121*(10), 5095–5114, doi:10.1002/2015JD024550.Received.

Morrison, H., G. de Boer, G. Feingold, J. Harrington, M. D. Shupe, and K. Sulia (2011), Resilience of persistent Arctic mixed-phase clouds, *Nature Geoscience*, *5*(1), 11–17, doi:10.1038/ngeo1332.

Mote, T. L. (2007), Greenland surface melt trends 1973–2007: Evidence of a large increase in 2007, *Geophysical Research Letters*, *34*(22), L22,507, doi:10.1029/2007GL031976.

Neff, W., G. P. Compo, F. Martin Ralph, and M. D. Shupe (2014), Continental heat anomalies and the extreme melting of the Greenland ice surface in 2012 and 1889, *Journal of Geophysical Research: Atmospheres*, *119*(11), 6520–6536, doi:10.1002/2014JD021470.

Nghiem, S. V., D. K. Hall, T. L. Mote, M. Tedesco, M. R. Albert, K. Keegan, C. A. Shuman, N. E. DiGirolamo, and G. Neumann (2012), The extreme melt across the Greenland ice sheet in 2012, *Geophysical Research Letters*, *39*(20), L20,502, doi:10.1029/2012GL053611.

Noël, B., W. J. van de Berg, E. van Meijgaard, P. Kuipers Munneke, R. S. W. van de Wal, and M. R. van den Broeke (2015), Evaluation of the updated regional climate model RACMO2.3: Summer snowfall impact on the Greenland Ice Sheet, *The Cryosphere*, *9*(5), 1831–1844, doi:10.5194/tc-9-1831-2015.

Paulescu, E., and R. Blaga (2016), Regression models for hourly diffuse solar radiation, *Solar Energy*, *125*, 111–124, doi:10.1016/j.solener.2015.11.044.

Perovich, D. K., T. C. Grenfell, B. Light, and P. V. Hobbs (2002), Seasonal evolution of the albedo of multiyear Arctic sea ice, *Journal of Geophysical Research*, *107*(C10), 8044, doi:10.1029/2000JC000438.

Qian, Y., C. N. Long, H. Wang, J. M. Comstock, S. A. McFarlane, and S. Xie (2012), Evaluation of cloud fraction and its radiative effect simulated by IPCC AR4 global models against ARM surface observations, *Atmospheric Chemistry and Physics*, *12*(4), 1785–1810, doi:10.5194/acp-12-1785-2012.

Randall, D., et al. (1998), Status of and outlook for large-scale modeling of atmosphere-ice-ocean interactions in the Arctic, *Bulletin of the American Meteorological Society*, *79*(2), 197–219, doi:10.1175/1520-0477(1998)079⟨0197:SOAOFL⟩2.0.CO;2.

Reda, I., and A. Andreas (2004), Solar position algorithm for solar radiation applications, *Solar Energy*, *76*(5), 577–589, doi:10.1016/j.solener.2003.12.003.

Reindl, D., W. Beckman, and J. Duffie (1990), Evaluation of hourly tilted surface radiation models, *Solar Energy*, *45*(1), 9–17, doi:10.1016/0038-092X(90)90061-G.

Rienecker, M. M., et al. (2011), MERRA: NASA's Modern-Era Retrospective Analysis for Research and Applications, *Journal of Climate*, *24*(14), 3624–3648, doi:10.1175/JCLI-D-11-00015.1.

Rignot, E., I. Velicogna, M. R. van den Broeke, A. Monaghan, and J. T. M. Lenaerts (2011), Acceleration of the contribution of the Greenland and Antarctic ice sheets to sea level rise, *Geophysical Research Letters*, *38*(5), L05,503, doi:10.1029/2011GL046583.

Ryan, J. C., A. Hubbard, T. D. Irvine-Fynn, S. H. Doyle, J. M. Cook, M. Stibal, and J. E. Box (2017), How robust are in situ observations for validating satellite-derived albedo over the dark zone of the Greenland Ice Sheet?, *Geophysical Research Letters*, *44*(12), 6218–6225, doi:10.1002/2017GL073661.

Sanford, T., P. C. Frumhoff, A. Luers, and J. Gulledge (2014), The climate policy narrative for a dangerously warming world, *Nature Climate Change*, *4*(3), 164–166, doi:10.1038/nclimate2148.

Sedlar, J., et al. (2011), A transitioning Arctic surface energy budget: the impacts of solar zenith angle, surface albedo and cloud radiative forcing, *Climate Dynamics*, *37*(7-8), 1643–1660, doi:10.1007/s00382-010-0937-5.

Serreze, M. C., and R. G. Barry (2011), Processes and impacts of Arctic amplification: A research synthesis, *Global and Planetary Change*, *77*(1-2), 85–96, doi:10.1016/j.gloplacha.2011.03.004.

Serreze, M. C., M. M. Holland, and J. Stroeve (2007), Perspectives on the Arctic's shrinking sea-ice cover., *Science*, *315*(5818), 1533–1536, doi:10.1126/science.1139426.

Shupe, M. D., and J. M. Intrieri (2004), Cloud radiative forcing of the Arctic surface : The influence of cloud properties, surface albedo, and solar zenith angle, *Journal of Climate*, *17*(3), 616–628, doi:10.1175/1520-0442(2004)017⟨0616:CRFOTA⟩2.0.CO;2.

Shupe, M. D., V. P. Walden, E. Eloranta, T. Uttal, J. R. Campbell, S. M. Starkweather, and M. Shiobara (2011), Clouds at Arctic atmospheric observatories. Part I: Occurrence and macrophysical properties, *Journal of Applied Meteorology and Climatology*, *50*(3), 626–644, doi:10.1175/2010JAMC2467.1.

Shupe, M. D., P. O. G. Persson, I. M. Brooks, M. Tjernström, J. Sedlar, T. Mauritsen, S. Sjogren, and C. Leck (2013a), Cloud and boundary layer interactions over the Arctic sea ice in late summer, *Atmospheric Chemistry and Physics*, *13*(18), 9379–9399, doi:10.5194/acp-13-9379-2013.

Shupe, M. D., et al. (2013b), High and dry: New observations of tropospheric and cloud properties above the Greenland Ice Sheet, *Bulletin of the American Meteorological Society*, *94*(2), 169–186, doi:10.1175/BAMS-D-11-00249.1.

Steffen, C., J. Box, and W. Abdalati (1996), Greenland Climate Network: GC-Net, *US Army Cold Regions Reattach and Engineering (CRREL), CRREL Special Report*, pp. 98–103.

Stroeve, J., J. E. Box, F. Gao, S. Liang, A. Nolin, and C. Schaaf (2005), Accuracy assessment of the MODIS 16-day albedo product for snow: comparisons with Greenland in situ measurements, *Remote Sensing of Environment*, *94*(1), 46–60, doi:10.1016/j.rse.2004.09.001.

Stroeve, J., J. E. Box, Z. Wang, C. Schaaf, and A. Barrett (2013), Re-evaluation of MODIS MCD43 Greenland albedo accuracy and trends, *Remote Sensing of Environment*, *138*, 199–214, doi:10.1016/j.rse.2013.07.023.

Stroeve, J. C., J. E. Box, C. Fowler, T. Haran, and J. Key (2001), Intercomparison between in situ and AVHRR polar pathfinder-derived surface albedo over Greenland, *Remote Sensing of Environment*, *75*(3), 360–374, doi:10.1016/S0034-4257(00)00179-6.

Susskind, J., C. Barnet, and J. Blaisdell (2003), Retrieval of atmospheric and surface parameters from AIRS/AMSU/HSB data in the presence of clouds, *IEEE Transactions on Geoscience and Remote Sensing*, *41*(2), 390–409, doi:10.1109/TGRS.2002.808236.

Swingedouw, D., and P. Braconnot (2007), Effect of the Greenland Ice-Sheet melting on the response and stability of the Amoc in the next centuries, in *Ocean Circulation: Mechanisms and Impacts—Past and Future Changes of Meridional Overturning*, edited by A. Schmittner, J. C. H. Chiang, and S. R. Hemming, pp. 383–392, American Geophysical Union, Washington, D. C., U.S.A., doi:10.1029/173GM24.

Tedesco, M., X. Fettweis, M. R. van den Broeke, R. S. W. van de Wal, C. J. P. P. Smeets, W. J. van de Berg, M. C. Serreze, and J. E. Box (2011), The role of albedo and accumulation in the 2010 melting record in Greenland, *Environmental Research Letters*, *6*(1), 014,005, doi:10.1088/1748-9326/6/1/014005.

Tedesco, M., X. Fettweis, T. Mote, J. Wahr, P. Alexander, J. E. Box, and B. Wouters (2013), Evidence and analysis of 2012 Greenland records from spaceborne observations, a regional climate model and reanalysis data, *The Cryosphere*, *7*(2), 615–630, doi:10.5194/tc-7-615-2013.

Tjernström, M., et al. (2014), The Arctic Summer Cloud Ocean Study (ASCOS): overview and experimental design, *Atmospheric Chemistry and Physics*, *14*(6), 2823–2869, doi:10.5194/acp-14-2823-2014.

Turner, D. D., et al. (2007), Thin liquid water clouds: Their importance and our challenge, *Bulletin of the American Meteorological Society*, *88*(2), 177–190, doi:10.1175/BAMS-88-2-177.

van As, D. (2011), Warming, glacier melt and surface energy budget from weather station observations in the Melville Bay region of northwest Greenland, *Journal of Glaciology*, *57*(202), 208–220, doi:10.3189/002214311796405898.

van As, D., and R. S. Fausto (2011), Programme for Monitoring of the Greenland Ice Sheet (PROMICE): first temperature and ablation records, *Geological Survey of Denmark and Greenland Bulletin*, *23*, 73–76.

van As, D., et al. (2014), Increasing meltwater discharge from the Nuuk region of the Greenland ice sheet and implications for mass balance (1960–2012), *Journal of Glaciology*, *60*(220), 314–322, doi:10.3189/2014JoG13J065.

van den Broeke, M., D. van As, C. Reijmer, and R. van de Wal (2004), Assessing and improving the quality of unattended radiation observations in Antarctica, *Journal of Atmospheric and Oceanic Technology*, *21*(9), 1417–1431, doi:10.1175/1520-0426(2004)021⟨1417:AAITQO⟩2.0.CO;2.

van den Broeke, M. R., C. J. P. P. Smeets, and R. S. W. van de Wal (2011), The seasonal cycle and interannual variability of surface energy balance and melt in the ablation zone of the west Greenland ice sheet, *The Cryosphere*, *5*(2), 377–390, doi:10.5194/tc-5-377-2011.

Van Tricht, K., S. Lhermitte, J. T. M. Lenaerts, I. V. Gorodetskaya, T. S. L'Ecuyer, B. Noël, M. R. van den Broeke, D. D. Turner, and N. P. M. van Lipzig (2016), Clouds enhance Greenland ice sheet meltwater runoff, *Nature Communications*, *7*, 10,266, doi:10.1038/ncomms10266.

Vavrus, S., D. Waliser, A. Schweiger, and J. Francis (2008), Simulations of 20th and 21st century Arctic cloud amount in the global climate models assessed in the IPCC AR4, *Climate Dynamics*, *33*(7-8), 1099–1115, doi:10.1007/s00382-008-0475-6.

Vavrus, S., M. M. Holland, and D. A. Bailey (2010), Changes in Arctic clouds during intervals of rapid sea ice loss, *Climate Dynamics*, *36*(7-8), 1475–1489, doi:10.1007/s00382-010-0816-0.

Velicogna, I., and J. Wahr (2013), Time-variable gravity observations of ice sheet mass balance: Precision and limitations of the GRACE satellite data, *Geophysical Research Letters*, *40*(12), 3055–3063, doi:10.1002/grl.50527.

Verlinde, J., B. D. Zak, M. D. Shupe, M. D. Ivey, and K. Stamnes (2016), The ARM North Slope of Alaska (NSA) Sites, in *The Atmospheric Radiation Measurement (ARM) program: The first 20 years. Meteorological Monographs.*, vol. 57, edited by D. D. Turner and R. G. Ellingson, chap. 8, pp. 8.1–8.13, doi:10.1175/AMSMONOGRAPHS-D-15-0023.1.

Walsh, J. E., W. L. Chapman, and D. H. Portis (2009), Arctic cloud fraction and radiative fluxes in atmospheric reanalyses, *Journal of Climate*, *22*(9), 2316–2334, doi:10.1175/2008JCLI2213.1.

Wang, W., C. S. Zender, D. van As, P. C. J. P. Smeets, and M. R. van den Broeke (2016), A Retrospective, Iterative, Geometry-Based (RIGB) tilt-correction method for radiation observed by automatic weather stations on snow-covered surfaces: application to Greenland, *The Cryosphere*, *10*(2), 727–741, doi:10.5194/tc-10-727-2016.

Wang, X., and J. R. Key (2003), Recent trends in Arctic surface, cloud, and radiation properties from space., *Science*, *299*(5613), 1725–1728, doi:10.1126/science.1078065.

Wang, X., and J. R. Key (2005), Arctic surface, cloud, and radiation properties based on the AVHRR Polar Pathfinder dataset. Part I: Spatial and temporal characteristics, *Journal of Climate*, *18*(14), 2558–2574, doi:10.1175/JCLI3438.1.

Wang, X., and C. S. Zender (2010a), Constraining MODIS snow albedo at large solar zenith angles: Implications for the surface energy budget in Greenland, *Journal of Geophysical Research*, *115*(F4), F04,015, doi:10.1029/2009JF001436.

Wang, X., and C. S. Zender (2010b), MODIS snow albedo bias at high solar zenith angles relative to theory and to in situ observations in Greenland, *Remote Sensing of Environment*, *114*(3), 563–575, doi:10.1016/j.rse.2009.10.014.

Wang, X., and C. S. Zender (2011), Arctic and Antarctic diurnal and seasonal variations of snow albedo from multiyear Baseline Surface Radiation Network measurements, *Journal of Geophysical Research*, *116*(F3), F03,008, doi:10.1029/2010JF001864.

Wesslén, C., M. Tjernström, D. H. Bromwich, G. de Boer, A. M. L. Ekman, L.-S. Bai, and S.-H. Wang (2014), The Arctic summer atmosphere: an evaluation of reanalyses using ASCOS data, *Atmospheric Chemistry and Physics*, *14*(5), 2605–2624, doi:10.5194/acp-14-2605-2014.

Wielicki, B. A., B. R. Barkstrom, E. F. Harrison, R. B. Lee, G. L. Smith, and J. E. Cooper (1996), Clouds and the Earth's Radiant Energy System (CERES): An Earth Observing System experiment, doi:10.1175/1520-0477(1996)077⟨0853:CATERE⟩2.0.CO;2.

Wilkes, M. V. (1954), A table of Chapman's grazing incidence integral Ch(x, χ), *Proceedings of the Physical Society. Section B*, *67*(4), 304, doi:10.1088/0370-1301/67/4/304.

Winton, M. (2006), Amplified Arctic climate change: What does surface albedo feedback have to do with it?, *Geophysical Research Letters*, *33*(3), L03,701, doi:10.1029/2005GL025244.

Zender, C. S. (1999), Global climatology of abundance and solar absorption of oxygen collision complexes, *Journal of Geophysical Research*, *104*(D20), 24,471, doi:10.1029/1999JD900797.

Zib, B. J., X. Dong, B. Xi, and A. Kennedy (2012), Evaluation and intercomparison of cloud fraction and radiative fluxes in recent reanalyses over the Arctic using BSRN surface observations, *Journal of Climate*, *25*(7), 2291–2305, doi:10.1175/JCLI-D-11-00147.1.

Zygmuntowska, M., T. Mauritsen, J. Quaas, and L. Kaleschke (2012), Arctic clouds and surface radiation—a critical comparison of satellite retrievals and the ERA-Interim reanalysis, *Atmospheric Chemistry and Physics*, *12*(14), 6667–6677, doi:10.5194/acp-12-6667-2012.